

**Acoustic angiography: a new imaging platform for high resolution  
mapping of microvasculature and tumor assessment**

Ryan C. Gessner

A dissertation submitted to the faculty of the University of North Carolina at Chapel Hill in partial fulfillment of the requirements for the degree of Doctor of Philosophy in the Department of Biomedical Engineering.

Chapel Hill  
2013

Approved by:

Paul A. Dayton, Ph.D.

Stephen R. Aylward, Ph.D.

Caterina M. Gallippi, Ph.D.

David Lalush, Ph.D.

Yueh Lee, M.D., Ph.D.

© 2013  
Ryan C. Gessner  
ALL RIGHTS RESERVED

## ABSTRACT

**RYAN C. GESSNER: Acoustic angiography: a new imaging platform for high resolution mapping of microvasculature and tumor assessment.**  
(Under the direction of Paul A. Dayton, Ph.D.)

Statistically, one in four Americans will die from cancer. Many new tumor detection and therapeutic approaches have improved patient outcomes, but cancer continues to run rampant in our country; it claimed the lives of 1.6 million Americans in 2012. To put this number of *annual deaths* in perspective, it is over 500 times the number of people who died in the horrific attacks on September 11, 2001. This dissertation does not offer either an antidote to the disease, nor a detection mechanism appropriate for all tumor types. It does, however, present the description and characterization of a novel dual-frequency ultrasound imaging transducer, capable of operating in a new imaging mode we call ‘acoustic angiography.’ These images offer high resolution and high contrast 3D depictions of the microvasculature; herein we demonstrate its cancer assessment utility by way of multiple imaging studies.

Throughout this dissertation, image data from both healthy and diseased tissues are presented. Additionally, acoustic assessments of vasculature within an *ex vivo* biomatrix scaffold model (a platform for creating of artificial organs) are presented. A vessel mapping algorithm, originally developed for human magnetic resonance angiography images, has been implemented in both *in vivo* and *ex vivo* tissue volumes. A novel microvessel phantom generation technique is presented, which allows ground-truth coordinates for vascular networks to be defined and imaged. Finally, the ultrasound pulsing technique, radiation force, was used as a method to improve the diagnostic sensitivity of ultrasound to malignant tumors. Together, the results of these studies suggest that

the imaging approach, acoustic angiography, enabled by our new dual-frequency ultrasound transducer, could eventually be used to detect and monitor tumors in a clinical imaging context.

This dissertation supports the following three hypotheses:

- 1. A prototype dual-frequency ultrasound transducer can be used to depict *in vivo* microvasculature,**
- 2. These microvascular images can be quantitatively assessed as a means to characterize the presence of a tumor, and evaluate tumor response to therapy, and**
- 3. Radiation force can be used as a method to improve ultrasonic diagnostic sensitivity to the presence of a tumor.**



To my teachers and mentors, who for my entire life have entertained a daily barrage of *but-what-if-THIS-happened?!* questions. By doing so they have each nurtured my curiosity about the underlying mechanics of that mysterious beast: nature. Without them, the questions driving the research within this dissertation might never have been asked.

## ACKNOWLEDGMENTS

I would like to acknowledge my family for their unyielding support throughout the last 27 years of my life. I also could not have asked for a better graduate school advisor than Paul Dayton. Liz Bullitt's work in the quantitative analysis of vessel morphologies, combined with her willingness to mentor me (essentially only *moments* before her retirement) provided a huge amount of initial momentum to my project. Regarding funding: the National Science Foundation's Graduate Research Program fellowship allowed me the flexibility and latitude to pursue many of the topics contained within this dissertation, and for that I am grateful. Finally, I would like to thank my labmates - particularly Dr. James Tsuruta, who manufactured nearly all microbubble contrast agents used in these studies - for creating a uniquely wonderful lab environment in which to work, and for providing experimental assistance and insight for my time at UNC.

## TABLE OF CONTENTS

Table of Contents . . . . .	vii
List of Figures . . . . .	xi
List of Tables . . . . .	xiv
<b>1 Introduction . . . . .</b>	<b>1</b>
1.1 Cancer imaging with ultrasound . . . . .	1
1.2 Contrast ultrasound . . . . .	3
1.3 Dissertation scope and objectives . . . . .	6
<b>2 Detecting cancer’s vascular footprint . . . . .</b>	<b>8</b>
2.1 Detecting cancer’s footprint . . . . .	8
2.1.1 Pathologic tissue’s aberrant vessel morphologies . . . . .	9
2.1.2 How are vessels extracted from images? . . . . .	12
2.1.3 How are vessel structures quantified? . . . . .	15
2.2 Detecting molecular signatures of disease . . . . .	17
2.2.1 Ultrasonic molecular imaging . . . . .	19
2.2.2 Challenges in molecular imaging with ultrasound . . . . .	22
<b>3 Acoustic angiography - a new contrast imaging approach . . . . .</b>	<b>25</b>
3.1 Evaluating a prototype dual-frequency transducer . . . . .	26

3.1.1	Materials and methods . . . . .	27
3.1.2	Results . . . . .	35
3.1.3	Discussion . . . . .	44
3.1.4	Conclusion . . . . .	49
3.2	High resolution assessment of vessel architecture - <i>ex vivo</i> tissue samples	49
3.2.1	Materials and methods: . . . . .	53
3.2.2	Results . . . . .	59
3.2.3	Discussion and concluding remarks . . . . .	66
3.3	Acoustic angiography for assessing microvasculature structure: pilot <i>in vivo</i> studies . . . . .	72
3.3.1	Animal imaging . . . . .	72
3.3.2	Results . . . . .	74
3.3.3	Discussion and summary . . . . .	81
<b>4</b>	<b>Toward the detection of aberrant vessel morphologies with acoustic angiography . . . . .</b>	<b>83</b>
4.1	3D microvessel-mimicking ultrasound phantoms produced with a scanning motion system . . . . .	83
4.1.1	Materials and methods . . . . .	85
4.1.2	Results . . . . .	88
4.1.3	Discussion and conclusions . . . . .	91
4.2	Quantifying vessel structure in controlled <i>in vitro</i> context . . . . .	94
4.2.1	Methods . . . . .	94
4.2.2	Results . . . . .	98
4.2.3	Conclusions and proposed future work . . . . .	100
<b>5</b>	<b>Detecting and assessing cancer with acoustic angiography . . . . .</b>	<b>102</b>

5.1	Detecting aberrant vessel morphologies with acoustic angiography . . .	102
5.1.1	Materials and methods . . . . .	103
5.1.2	Results . . . . .	108
5.1.3	Discussion . . . . .	117
5.2	Assessing tumor therapeutic response with acoustic angiography . . . .	119
5.2.1	Methods . . . . .	121
5.2.2	Tumor model . . . . .	121
5.2.3	Results and discussion . . . . .	127
5.2.4	Concluding remarks . . . . .	138
<b>6</b>	<b>Radiation force enhanced molecular imaging . . . . .</b>	<b>141</b>
6.1	Molecular imaging with the dual-frequency prototype . . . . .	143
6.1.1	Methods . . . . .	143
6.1.2	Results . . . . .	145
6.1.3	Discussion . . . . .	148
6.1.4	Concluding remarks . . . . .	149
6.2	Volumetric molecular imaging with a clinical system . . . . .	150
6.2.1	Materials and methods . . . . .	150
6.2.2	Results . . . . .	158
6.2.3	Discussion . . . . .	164
6.2.4	Conclusion . . . . .	169
<b>7</b>	<b>Closing remarks . . . . .</b>	<b>170</b>
7.1	The future acoustic angiography . . . . .	171
7.2	The future molecular imaging with ultrasound . . . . .	172
<b>A</b>	<b>Microbubble contrast agent formulation . . . . .</b>	<b>174</b>
A.1	Perfusion agents . . . . .	174

A.2 <i>In vitro</i> targeted agents . . . . .	174
A.3 <i>In vivo</i> targeted agents . . . . .	174
<b>B IEEE December 2010 Cover Image . . . . .</b>	<b>176</b>
<b>C <i>Ex vivo</i> liver scaffold preparation . . . . .</b>	<b>178</b>
<b>Bibliography . . . . .</b>	<b>182</b>

## LIST OF FIGURES

1.1	Dayton lab ultrasound equipment . . . . .	2
1.2	Overview of microbubbles . . . . .	3
1.3	Overview of contrast imaging approaches . . . . .	5
2.1	Intravital microscopy image of vasculature . . . . .	11
2.2	Quantifying vessel morphologies . . . . .	16
2.3	Qualitative illustration of the effect of resolution on vessel imaging . . . . .	18
2.4	Cartoon illustration of molecular imaging with ultrasound . . . . .	20
2.5	Schematic of targeted contrast accumulation over time . . . . .	21
2.6	Cartoon illustration of radiation force enhanced targeting . . . . .	23
3.1	Dual-frequency probe schematic . . . . .	28
3.2	Dual-frequency probe beam maps . . . . .	36
3.3	Dual-frequency probe axial pressure maps . . . . .	37
3.4	Time domain responses from contrast and tissue . . . . .	37
3.5	Frequency domain responses from contrast and tissue . . . . .	38
3.6	Contrast to tissue ratios computed with dual-frequency probe . . . . .	39
3.7	Example acoustic angiography images of contrast in rat kidney . . . . .	40
3.8	Comparison of all imaging modes tested . . . . .	42
3.9	Comparison of imaging proficiency with respiratory gating . . . . .	43
3.10	Evidence of radiation force on microbubbles . . . . .	44

3.11	Overview of bioeffect-inducing acoustic parameters . . . . .	45
3.12	Liver scaffold imaging chamber . . . . .	54
3.13	Schematic of image pipeline . . . . .	62
3.14	Biomatrix perfusion stability data . . . . .	63
3.15	All image data acquired of biomatrix samples . . . . .	64
3.16	Quantitative comparison between samples of biomatrix vascularity . . . . .	65
3.17	3D renderings of the three liver scaffolds . . . . .	67
3.18	Overlay of contrast and b-mode . . . . .	75
3.19	Comparison of tumor-bearing and healthy tissue . . . . .	77
3.20	Comparison of Acoustic Angiography with photoacoustics . . . . .	79
3.21	Overlay of contrast and b-mode . . . . .	80
4.1	3D vessel phantom schematic . . . . .	86
4.2	3D vessel phantom generation cartoon . . . . .	87
4.3	Generating phantoms with increasing tortuosity . . . . .	89
4.4	Creating a bifurcating vessel network . . . . .	90
4.5	Measuring contrast sensitivity vs. depth . . . . .	91
4.6	Vessel phantoms used for segmentation . . . . .	95
4.7	Example segmentations . . . . .	96
4.8	Quantifying error in vessel phantom segmentations . . . . .	99
5.1	Microvasculature comparison between Control and Tumor-bearing tissue volumes . . . . .	110
5.2	Example vessel centerlines . . . . .	111
5.3	Quantitative comparisons between tumor and control vessels . . . . .	115
5.4	Retrospective subsampling $p$ values . . . . .	116
5.5	ROC analysis of tortuosity as diagnostic indicator . . . . .	116



5.6	Treatment room for irradiations . . . . .	123
5.7	Treatment timeline . . . . .	124
5.8	Elliptical ROI Computation . . . . .	126
5.9	Pretreatment tumor volumes . . . . .	127
5.10	Post-treatment survival curves . . . . .	128
5.11	Post-treatment animal weights . . . . .	129
5.12	Radiation beam simulation . . . . .	131
5.13	Tumor growth: All groups . . . . .	132
5.14	Tumor growth: 20 Gy group . . . . .	133
5.15	Perfusion of tumors post therapy . . . . .	134
5.16	Perfusion volume ratios post therapy . . . . .	135
5.17	Power analysis . . . . .	137
6.1	Cartoon schematic of RF application . . . . .	144
6.2	Acoustic and optical detection of successful RF . . . . .	146
6.3	3D targeting results . . . . .	147
6.4	Visualizing targeting signal . . . . .	148
6.5	Radiation force <i>in vitro</i> schematic . . . . .	153
6.6	Radiation force <i>in vitro</i> push optimization results . . . . .	159
6.7	Results from the cumulative error function analysis . . . . .	160
6.8	Effects of radiation force on microbubble targeting <i>in vivo</i> . . . . .	161
6.9	3D rendering of microbubble targeting <i>in vivo</i> . . . . .	163
C.1	Decellularization process . . . . .	179
C.2	Liver in bioreactor . . . . .	181

## LIST OF TABLES

3.1	Imaging pressures tested . . . . .	32
3.2	Blood flow rates tested . . . . .	34
4.1	Summary of segmentation consistency results . . . . .	98
5.1	Summary of tortuosity metrics . . . . .	112
5.2	Summary of statistical tests - tortuosity . . . . .	113
5.3	Summary of recent preclinical ultrasound imaging studies . . . . .	121
6.1	Comparison of microbubble targeting efficiency . . . . .	162

# CHAPTER 1

## INTRODUCTION

### 1.1 Cancer imaging with ultrasound

This dissertation is devoted to presenting and discussing work surrounding the development of ultrasound imaging tools to improve cancer research and diagnostics. It is well established that a tumor's growth is highly dependent on its blood supply, which is under constant and chaotic remodeling as a neoplasm evolves. [1] Thus, there exists a widespread demand within the clinical and preclinical cancer research communities for methods to noninvasively and quantitatively assess tumor vascularization and blood supply. These research communities constantly seek to improve their imaging methods to thereby increase their understanding of tumor progression, and the quality of their diagnostic and therapeutic decision making. Ultrasound offers several advantages over other imaging modalities for the preclinical and clinical assessment of tumors and tumor blood flow.

#### **Widespread accessibility**

Ultrasound systems are easily portable, which enables bedside-imaging within a clinical environment (examples of two common systems, one clinical and the other preclinical, can be seen in Figure 1.1). In fact, some ultrasound systems are now so miniaturized that they are capable of being carried in physicians' pockets. In addition to being significantly smaller than other imaging systems, ultrasound devices are also relatively

inexpensive, costing only a fraction of what other modalities' systems cost (magnetic resonance (MR) and x-ray computed tomography(CT)). This makes ultrasound much more accessible to rural or less affluent communities, and much more financially viable for longitudinal studies with many timepoints, or drug efficacy studies with many subjects. Using other imaging approaches, these large-cohort or multiple-timepoint studies could be prohibitively expensive.

### Noninvasive and real time

Ultrasound images do not require ionizing radiation to create images, as is the case with x-ray CT. Whereas longitudinal studies with CT imaging necessitate careful dose considerations, longitudinal ultrasound acquisitions are not problematic, enabling physicians or preclinical researchers to assess changes in tumor size and blood perfusion at many timepoints before, and throughout treatment. Images are also real-time, enabling rapid feedback for imaging transducer position to optimize image quality.

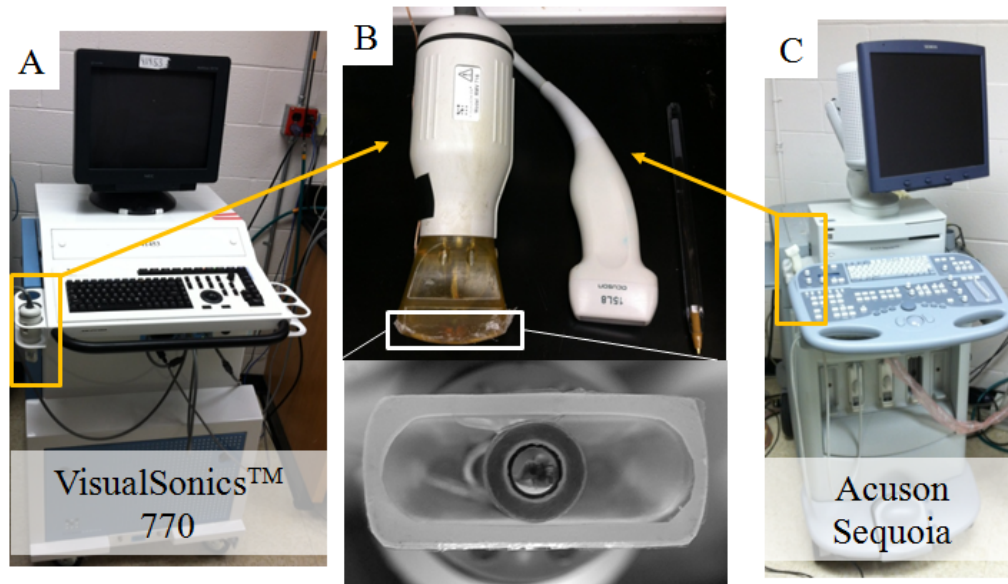


Figure 1.1: The ultrasound systems used to collect image data for this dissertation. A: The system used for acoustic angiography, B: Transducers for each system, C: The system used for CPS molecular imaging.

## 1.2 Contrast ultrasound

Because the cost of drug development is so high - many estimates put drug development, from initial compound screening through clinical trials at over 1 billion USD [2] - preclinical drug researchers continually seek to drive down costs of their studies. Some of these preclinical drug researchers have started using high resolution ultrasound to evaluate their candidate therapeutics.[3; 4; 5; 6]. Lipid-encapsulated microbubbles are often implemented as contrast agents during these ultrasound studies to improve detection of blood flow [7]. Microbubbles typically consist of a high molecular weight gas core stabilized with a lipid. High molecular weight gasses are preferred due to their low solubility in blood and poor diffusivity through their encapsulating shell. This extends microbubble circulation time *in vivo*. The acoustic impedance mismatch between the gas cores of microbubbles and the surrounding blood and tissue is approximately four orders of magnitude [8], causing them to scatter significantly more ultrasound energy than blood components, and thus enabling improved sensitivity of ultrasound to blood flow (Figure 1.2). Their use requires an intravascular injection of a solution of microbubbles immediately before an imaging exam. After their injection, the microbubble contrast agents traverse the circulatory system with similar rheology to erythrocytes [9].

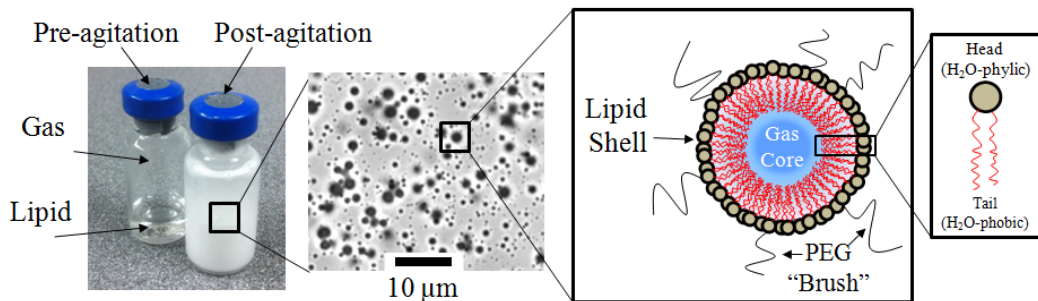


Figure 1.2: Far left: Vials of lipid and gas before and after mixing. The white froth is the suspension of microbubbles. If we zoom in a single contrast agent (cartoon) it is possible to see the orientations of the lipid monolayer, gas core, and PEG spacers.

The most basic method of contrast enhanced ultrasound relies on receiving the acoustic signal scattered from microbubbles at the fundamental imaging frequency. One limitation to this detection method is that echoes from both tissue and microbubbles are in the same frequency band. This necessitates a large quantity of injected microbubbles to compete with the inherent and unwanted tissue backscatter. However, owing to the broadband and nonlinear acoustic responses of these gas-filled spheres it is possible to overcome this limitation with other detection strategies. The most powerful microbubble imaging methods are derived from the nonlinear responses of microbubbles to ultrasound, providing distinct differences in microbubble echo signatures when compared with the linear responses of tissue and blood. Imaging modes such as harmonic imaging [10], subharmonic imaging [11; 12], phase inversion [13; 14], contrast pulse sequence (CPS) imaging [15; 16], and harmonic contrast imaging [17] exploit microbubbles' nonlinear response; all of these methods provide improved contrast-to-tissue ratios compared with the previously described fundamental mode imaging. Figure 1.3 provides a cartoon overview behind the pulsing schemes used to create images from the nonlinear oscillations of contrast agents in response to ultrasound pulses. Although these nonlinear imaging methods are now widely utilized in commercial ultrasound systems operating in the 1 to 15 MHz range, they are more challenging to implement in high-frequency ultrasound systems. One reason for this is that optimal microbubble response requires excitation near the resonant frequency [18], which is approximately 14 to 1.5 MHz for lipid-encapsulated bubbles that are 0.8 to 4  $\mu\text{m}$  in diameter, respectively. Most commonly available commercially produced microbubbles fall within this diameter range.

There is thus a well established tradeoff between imaging sensitivity to microbubbles, and imaging resolution, as lower frequencies correspond to lower spatial resolutions. This presents a problem for preclinical imaging studies, as imaging a preclinical

	Transmit	Resulting echoes	Signal processing	Without MCAs	With MCAs
<b>Fundamental Mode</b>		Tissue Bubble	n/a		
<b>CPS (multi-pulse)</b>		Tissue Bubble Tissue Bubble	 Tissue Bubble		
<b>Acoustic Angiography</b>		Tissue Bubble	HPF → Tissue HPF → Bubble		

Figure 1.3: A cartoon illustration of how CPS and acoustic angiography are distinct from fundamental mode imaging. The ‘Resulting echoes’ column illustrates the non-linear responses of microbubbles to different polarities and frequencies of pulses. HPF: ‘high pass filter.’

model (mouse or rat) requires higher resolution than most clinical systems will allow. This mismatch between microbubble resonance frequency and preclinical system imaging frequency provided the motivation behind the creation of a novel ultrasound imaging transducer capable of circumventing this tradeoff. This transducer is addressed in Chapter 3.1.

There are several contrast ultrasound techniques to evaluate a tumor’s blood supply or interior vascularization. Some of these strategies seek to quantify the *amount* of vascularization within the tissue by using Doppler techniques [19; 20; 21; 22], or contrast image-subtraction approaches [23; 24]. Other strategies attempt to extract information about the perfusion *rates* at which blood flows through the tissue using contrast-based destruction reperfusion (or “flash replenishment”) techniques [25; 26; 27; 28; 29; 30; 31]. Additionally, others have attempted to extract quantifiable metrics for vessel and

vessel network *structure* as a means to understand disease progression [32; 33; 29; 34]. Of particular interest is vessel tortuosity, or *bendiness* which is a morphological abnormality exhibited by cancerous vasculature in both humans and rodents [35; 36], and has been used as a marker for disease state and therapeutic response in clinical studies based on image-derived data [37; 38]. This effect will be described in more detail in Chapter 2.

Because the US Food and Drug Administration (FDA) has practiced excessive caution with respect to microbubble contrast agents, there is currently only one approved clinical application which implements a contrast ultrasound imaging protocol. Their use in other applications such as liver, kidney, thyroid, prostate, and breast tumor assessment, is becoming increasingly widespread, however, in several European and Asian countries. Additionally, as described above, there are a host of exciting new applications being developed in the preclinical realm with potential for clinical translation. Over the next decade, it is likely that the US clinical community will begin catching up with their European and Asian colleagues with respect to the frequency with which they implement these powerful contrast ultrasound imaging approaches. This thesis is primarily devoted to the research and results surrounding one of these new contrast imaging approaches, *acoustic angiography*. This imaging technique, while maybe years away from actual clinical use, is an exciting advance in the field.

### **1.3 Dissertation scope and objectives**

The overarching theme of this dissertation is the development and assessment of a new ultrasound imaging approach, acoustic angiography, enabled by a novel dual-frequency transducer prototype. The diagnostic context for using this imaging approach is presented in Chapter 2, followed by a physical description of the transducer and preliminary pilot studies in several different contexts (*in vitro*, *ex vivo*, and *in vivo*) presented in



Chapter 3. Following these pilot studies we present a description of the limitations in our ability to assess vascular morphological features, evaluated in a controlled *in vitro* context (Chapter 4) by way of a novel microvessel phantom generation approach. The final two chapters focus on the *in vivo* application of this imaging approach to cancer assessment and response to therapy, with Chapter 5 focusing on vessel network architectural features (vessel tortuosity and tumor vascularization) while Chapter 6 focuses on the application of molecular imaging approaches with both our dual-frequency transducer and a clinical ultrasound system.

## CHAPTER 2

### DETECTING CANCER'S VASCULAR FOOTPRINT

The first section of this chapter introduces the effect of cancer-associated vasculature having abnormal morphologies, and how these distinct features are detectable by a quantitative algorithm (Chapter 2.1). The second section describes another method of detecting cancer with ultrasound contrast agents, called ‘molecular imaging.’ (Chapter 2.2)

#### 2.1 Detecting cancer's footprint

Tumor growth beyond 2 mm<sup>3</sup> has been shown to depend on angiogenesis, which is defined as the formation and recruitment of new microvessels from existing vessels. [39; 40; 41]. There are many differences between vessels associated with angiogenic tumors and healthy vessels which can be used as diagnostic indicators of tumor presence and malignancy. For this dissertation, the scope of tumor assessment by way of angiogenesis detection is confined to two facets of vascular composition: (1) vascular

---

*Note:* This chapter has two sections, both of which draw from previous published material. Previously published material was reprinted with permission from the publishers.

**Chapter 2.1:** Ryan C. Gessner, Stephen Aylward, Paul A. Dayton, *Imaging tortuosity: the potential utility of acoustic angiography in cancer detection and tumor assessment*. Imaging in Medicine, 4(6):581-583, 2012. *editorial*

**Chapter 2.2:** Ryan Gessner, Paul A. Dayton. *Advances in molecular imaging with ultrasound*. Mol Imaging, 9(3):117-27, 2010. *review*.

architecture (both at the individual vessel level, and at the network level) and (2) angiogenic molecular markers expressed on the vascular endothelium. The following two sections describe these vascular features in greater detail, and provide some background information on detection strategies.

### **2.1.1 Pathologic tissue's aberrant vessel morphologies**

The morphology and structure of the vasculature associated with malignant tumors has long been observed to be chaotic and unusual compared with that of healthy tissues. In tumors, vessel diameters and branching patterns appear random, and the actual trajectories charted through the 3D tumor volume are often tortuous [36; 42]. These morphological abnormalities are hypothesized to be a result of a number of complicated physiological effects occurring in parallel, such as tumor cells' high metabolic demand and their unusual microenvironment (hypoxic, acidic and so on). These factors contribute to a heightened level of angiogenic activity in and around the tumor, which becomes a self-amplifying cycle when the newly formed vessels fail to supply the tumor cells' insatiable appetite for nutrients [43]. The heightened angiogenic activity also causes the basement membrane and support structure of the vessels to break down. Additionally, the poor organization of the vessel network results in an increase in pressure within the vessels, which is further exacerbated by the absence of lymphatic drainage from the tumor stroma.

As described above, the morphology and makeup of tumor vasculature diverge from healthy vasculature in several ways and these differences can be elucidated by either direct or indirect observations. For direct observations (i.e., quantification of 3D vessel morphologies) there are three critical components. First, the imaging modality must have a high enough spatial resolution to enable individual vessels to be resolved, and it must have sufficient signal-to-noise to enable differentiation of vessels from surrounding

tissue. Second, a segmentation approach must be able to extract vessels from the image volumes in a repeatable and reliable way. This stage usually requires some user input and feedback, although automated approaches allow for higher throughput and thus would be more amenable to clinical implementation. Finally, a classification algorithm based on the segmented vessel data that indicates the presence or degree of pathology is needed. Morphological features can be examined at either the vessel level (e.g., the tortuosity of a single vessel) or at the network level (e.g., the fractal dimension of the vessel tree). Indirect observations of cancer-associated vascular abnormalities are far more prevalent in the clinic today. Examples include measures of overall tissue perfusion and vessel permeability. These types of measurements are powerful indications of tumor presence and malignancy, but they are limited to more global estimations of vessel morphology within a tissue volume, and thus are insensitive to subtle changes occurring therein. These two types of observations (direct and indirect) have been shown to provide independently useful diagnostic information [44]. It is, therefore, unlikely that direct assessments of vascular structure will ever replace existing cancer imaging approaches; however, rather they will compliment them with additional diagnostically powerful information. This could result in a hybrid cancer-assessment approach that is more sensitive than either component alone.

### **Diagnostic information gleaned from vascular architecture**

Of interest from a cancer screening perspective, tumor-associated vascular irregularities can extend beyond the margins of a lesion, as angiogenic growth factors promoted by tumor cells can influence the morphologies of even major vessels in the vicinity of tumors [38]. Additionally, cancer-associated tortuous vessel morphologies have been observed in animal models much sooner than the arrival of a palpable mass. For example, within one day of the introduction of only a few tens of cancer cells, initially

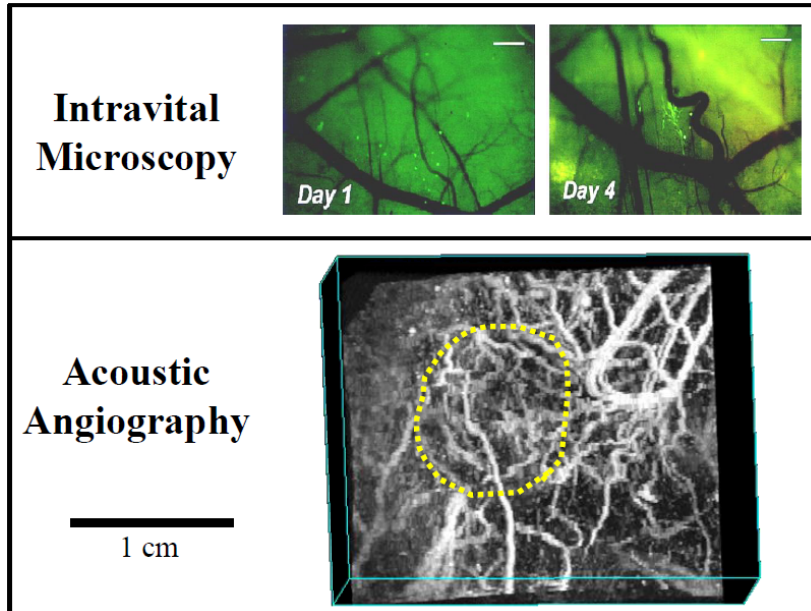


Figure 2.1: Comparison of cancerous vasculature viewed at different scales by different imaging modalities. Top: Intravital microscopy images from the Dewhirst lab at Duke University of tumor cells growing within a window chamber model in a rat (scale bar =  $200 \mu\text{m}$ ). The images illustrate vascular morphological abnormalities occurring within days of implantation of cancer cells. (Figure portions, from [35], reprinted with permission). Bottom: a maximum intensity projection through an acoustic angiography dataset illustrating the same type of morphological abnormalities both within and surrounding the tumor margins (dashed yellow line).

healthy vasculature in the tumor vicinity develop tortuosity abnormalities, [35] an effect observed across many cancer types.[45] Tortuosity abnormalities can spread to even major vessels over time, and have been observed with MRI in humans 1 cm away from any visible lesions.[38] Segmenting and quantifying the morphology of these abnormally shaped vessels has been shown to predict tumor therapeutic response between 2-6 months sooner in humans than traditional methods of estimating tumor volume.[38; 36] Additionally, successful tumor treatment has been shown to lead to rapid regression in tortuosity abnormalities, with changes occurring between hours to days after treatment. [38; 36; 46; 47] Finally, this vessel-morphology analysis has been performed in conjunction with a traditional blood perfusion analysis in an MRI therapeutic response

study of patients with intracranial neoplasms,[44] and the two methods were shown to provide independently useful diagnostic information. The renormalization of tumor vasculature is also of great interest to researchers and clinicians alike, as anticancer therapies, when effectively quelling a tumor’s progression, have been shown to have a rapid effect on the local vascular morphology. This normalization of vessels has served as an indication of eventual tumor volume reduction and the lack of normalization has correspondingly been associated with poor therapeutic response [48].

Thus the motivation for applying a quantitative vessel-morphological analysis to preclinical models of cancer is apparent, as most anti-cancer drug studies are performed in small rodents. To date, most recent progress in ultrasound assessment of therapeutic response has been in molecular and perfusion imaging, and there are some groups who have used 3D high frequency Doppler techniques to image vascular networks. Analyses of vessel network and vessel morphologies based on segmentations from ultrasound data, however, are scarce, though they have been achieved at lower imaging frequencies (and thus lower spatial resolution) in human thyroid and breast tumors imaging studies. [32; 33; 29; 34; 49] Analyzing the morphology of a vascular network within a diseased tissue volume provides a very sensitive method to assess the effects of therapy, which is particularly necessary when clinicians are seeking to tune their personalized therapeutic approaches [50].

### **2.1.2 How are vessels extracted from images?**

The following is an overview of how the segmentation algorithm used throughout this project functions. The mechanics of the algorithm are discussed at length in [51].

*Finding the vessel’s centerline:*

The extraction process is initialized after a user provides seed point near an intensity ridge (assuming vessels are bright on a dark background), and a scale of the blood

vessel selected. The gradient of the image is followed at the location the user specified until a local intensity maximum is reached (assumed to be the true center of the vessel).

*Following the vessel's centerline:*

Once an intensity ridge has been found, the extractor looks for what direction the vessel is traveling. This information is gleaned from the Hessian matrix, which allows the extractor to find the direction of least curvature, important in this case as this direction will be the one along an intensity ridge (i.e. normal to the plane bisecting the vessel, and in the direction of the vessel's trajectory). The next point along the vessel's centerline is then determined by stepping the normal plane at the intensity ridge a very small distance in the previously described direction of least curvature. The assumption here is that if the centerline is representing an anatomically relevant tube (vessel), its smooth trajectory will necessitate it passing through that shifted plane. The next intensity ridge is then found at the location of the shifted normal plane, and a new vessel trajectory and normal plane determined at this new intensity ridge. This process is repeated iteratively in both positive and negative directions from its initial starting point.

*Determining vessel radius*

The radius of the vessel is determined every ten steps along the ridge traversal. This is achieved by convolving a customized kernel with the image data in the previously described normal plane defined by the trajectory of the vessel at the location of interest. This "medialness" kernel is a circularly symmetric arrangement of spheres, and is maximized when the radius of the kernel equals that of the vessel. A physical analog to this operation is considering a ring of magnets of variable radius  $r$  oriented so that all North sides of the magnets are facing away from the center of the ring. If this ring of magnets is placed over another ring of fixed radius  $R$  oriented in the opposite

direction, the  $r$  that will result in the most stable configuration is when  $r = R$ . The extractor tests scales for vessel radius which are within 10% of the previous measurement of vessel radius, which assumes that the radius of anatomically relevant tubes will not rapidly fluctuate (an often accurate assumption, especially since the step size between centerline points is less than one voxel, so if the radius is increasing by more than 10% within that small distance, it's probable that the tube being extracted is not actually a vessel).

*When does the extractor know to stop?*

There are several criteria which result in the termination of a vessel extraction. These are tested at each point along the extraction. If a ridge does not exist in the shifted normal plane, the extraction will terminate (this could occur if the intensity drops below the noise level, as would be the case when large vessels feed sub-resolution capillary beds). Additionally, if a T-junction is encountered, the extraction will terminate. A T-junction would result in the vessel trajectory at the next test point along the centerline not falling within a specified "cone of acceptability."

Finally, there are several conditions that must be satisfied for a test location to be deemed a 'ridge point,' or valid location for a vessel centerline coordinate. These are listed as follows:

1. It must be on a convex intensity ridge. Mathematically this can be verified by ensuring the eigenvalues of the Hessian matrix at this location are negative.
2. It must be a local intensity maximum. Mathematically this can be demonstrated if the projections of the gradient at this location are equal to zero.
3. It must be located near a tube of a roughly circular cross section. This is determined by calculating the ratio of eigenvalues of the Hessian matrix in the direction normal to the ridge in question. This ratio changes as tubes become



more elliptical in cross-section.

### **2.1.3 How are vessel structures quantified?**

After an ensemble of microvessel centerlines had been extracted, their morphologies were quantified via previously established metrics for tortuosity [52]. These metrics, which provide a means to assess two distinct types of centerline tortuosity, were the distance metric (DM) and sum of angles metric (SOAM). The DM is a measure of how far a curve meanders between its end points and is computed as the ratio of the length of the extracted vessel path and the length of the secant line between the vessel's start and end. The SOAM is an index of vessel tortuosity that is computed by integrating the angular changes occurring between successive pairs of points along the vessel's centerline, normalized by the total vessel path length. (Figure 2.2)

### **Relationship between imaging system resolution and tortuosity metrics**

Assuming the same vessel is imaged by two distinct imaging systems, its digitized representation also will be different and thus the reported tortuosity values for that vessel's two image-derived segmentations could be reported as different. What follows is a short overview on the relationship between the imaging system's acquisition characteristics, and the reported tortuosity for a vessel imaged by that system.

A blood vessel can be considered a continuous curve through 3D space. Its representation by an ultrasound imaging system can be modeled in the most simple case as the original continuous curve first becoming blurred by the point spread function of the transducer, and then discretized by the pixels of the imaging system. By way of these processes, information can be lost and the true morphology of the vessel misrepresented. The following analysis will be restricted to 2D for convenience of illustration, though the concepts could be extended to 3D for volumetric data. Assume the continuous vessel curve, parameterized by  $C(x,y)$ , has a sinusoidal shape with a spatial period,  $T$ ,

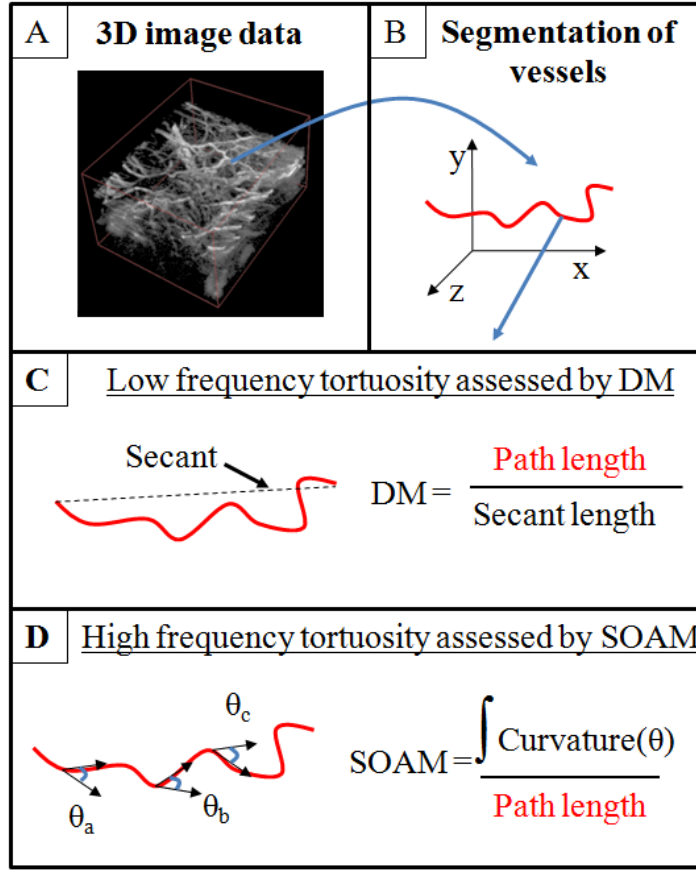


Figure 2.2: A cartoon illustration of how the DM and SOAM are computed from the vessel centerlines.

and is imaged by a system with isotropic resolution in the  $x$  and  $y$  axes of distance  $R$ . The data is discretized by pixels of width  $p$  for display. There are multiple scenarios in which the imaging system parameters ( $R$  and  $p$ ) could bias tortuosity measurements computed from the segmentation  $S(x,y)$  for continuous curve  $C(x,y)$ .

If  $p$  is larger than  $R$ , then vessels smaller than a pixel's width will be displayed by the imaging system as rectangular in cross-section (a form of quantization error). This will artificially inflate the intervoxel angles of  $S(x,y)$ . This is sometimes referred to the 'ping ponging' effect - imagine a ball bouncing erratically through a smooth pipe. This can also occur as a result of the extractor not being appropriately tuned to the point spread function of the imaging system. The ping-ponging effect will correspondingly

inflate the tortuosity values reported for a vessel. In the presence of this type of  $p > R$  quantization error, the SOAM values will be significantly more affected, since part of its computation involves the integral of these angular deviations between successive points. (Figure 2.2) The DM will also be impacted by this type of error, since the ping-ponging centerline of  $S(x,y)$  has a longer path length than the smooth centerline  $C(x,y)$ , with the same secant cord between the end points, though to less of a degree, since the path length errors away from the true centerline do not contribute appreciably to the overall path length, especially for anatomically relevant curves.

Another way the imaging system can bias the results of the tortuosity computation is if the resolution,  $R$ , is too close in size to the spatial period of the vessel being imaged (assume  $p < R$  and quantization errors are no longer significant). One should think of this in terms of the Nyquist-Shannon sampling theorem. The Nyquist-Shannon criterion states that for a continuous periodic curve to be accurately defined by a discretized representation, a sampling frequency of at least twice the frequency of the periodic signal must be implemented. Equivalently, in spatial units this means that the resolution of the imaging system must be at most half of the period of the curve  $C(x,y)$ . If the condition ( $R \leq \frac{T}{2}$ ) does not hold, then the curve will be aliased (Figure 2.3). Practically speaking, this means for an imaging system with  $R = 150 \mu\text{m}$ , the smallest periodic deviation which could be reliably imaged has a period of  $300 \mu\text{m}$ . This relationship is more quantitatively established in Chapter 4.

## **2.2 Detecting molecular signatures of disease**

One of the hallmarks of tumor cells is their upregulation of angiogenic growth factors, which when released into their surroundings promote endothelial cells in their vicinity to release proteases that degrade the basement membrane. This is beginning of sprouting angiogenesis (the formation of new blood vessels from existing blood vessels). The

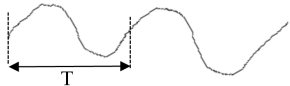
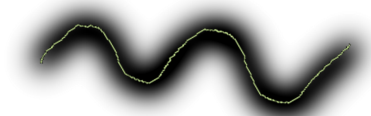
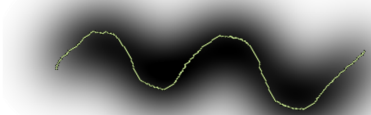
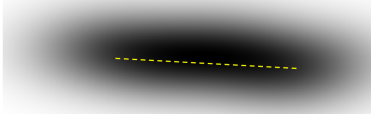
Continuous curve $C(x,y)$	
Resolution	Resulting image + segmentation
T/4	
T/2	
T	

Figure 2.3: A simulation of a continuous vessel curve,  $C(x,y)$ , being sampled by an imaging system at three different resolutions:  $T/4$ ,  $T/2$ , and  $T$ , where  $T$  is the spatial period of the main spatial frequency in  $C(x,y)$ . Simulated segmentations,  $S(x,y)$  are overlaid in yellow.

adhesion molecules used by endothelial cells to migrate along these new ‘sprouts’ are called *integrins*, enabling them to populate the voids in the matrix created by the proteases. These integrins are one potential site to which molecularly targeted contrast agents can be designed to bind. [53] There are several imaging modalities capable of molecular imaging of tumors - such as with SPECT, PET, and optical imaging modalities - and ultrasonic molecular imaging is still in its infancy. However, in preclinical studies, ultrasonic molecular imaging has shown promise in assessing angiogenesis and the functional status of tumors. This section describes the background behind ultrasonic molecular imaging, as well as an acoustic pulsing technique, known as “radiation force,” which can substantially improve the capabilities and utility of ultrasonic molecular imaging *in vitro* by circumventing one of the largest challenges to the approach (low numbers of retained contrast agents). In Chapter 6, this is tested for the first time

*in vivo* in which the radiation force pushing and the imaging are achieved on the same clinical ultrasound system.

### **2.2.1 Ultrasonic molecular imaging**

Traditional non-contrast enhanced ultrasound imaging utilizes a transducer to produce pulses of sound that propagate into tissue. These sound pulses are scattered from interfaces between tissue components of different density and compressibility. Scattered ultrasound reflections are detected and processed to form an image based on the intensity of scattered echoes and the time delay, which corresponds to the depth from which echoes have returned. As such, standard ultrasound imaging is well suited for assessment of anatomical features and measurement of blood flow in large vessels, however, there is no mechanism by which non-contrast enhanced ultrasound can detect changes in physiology on a molecular level.

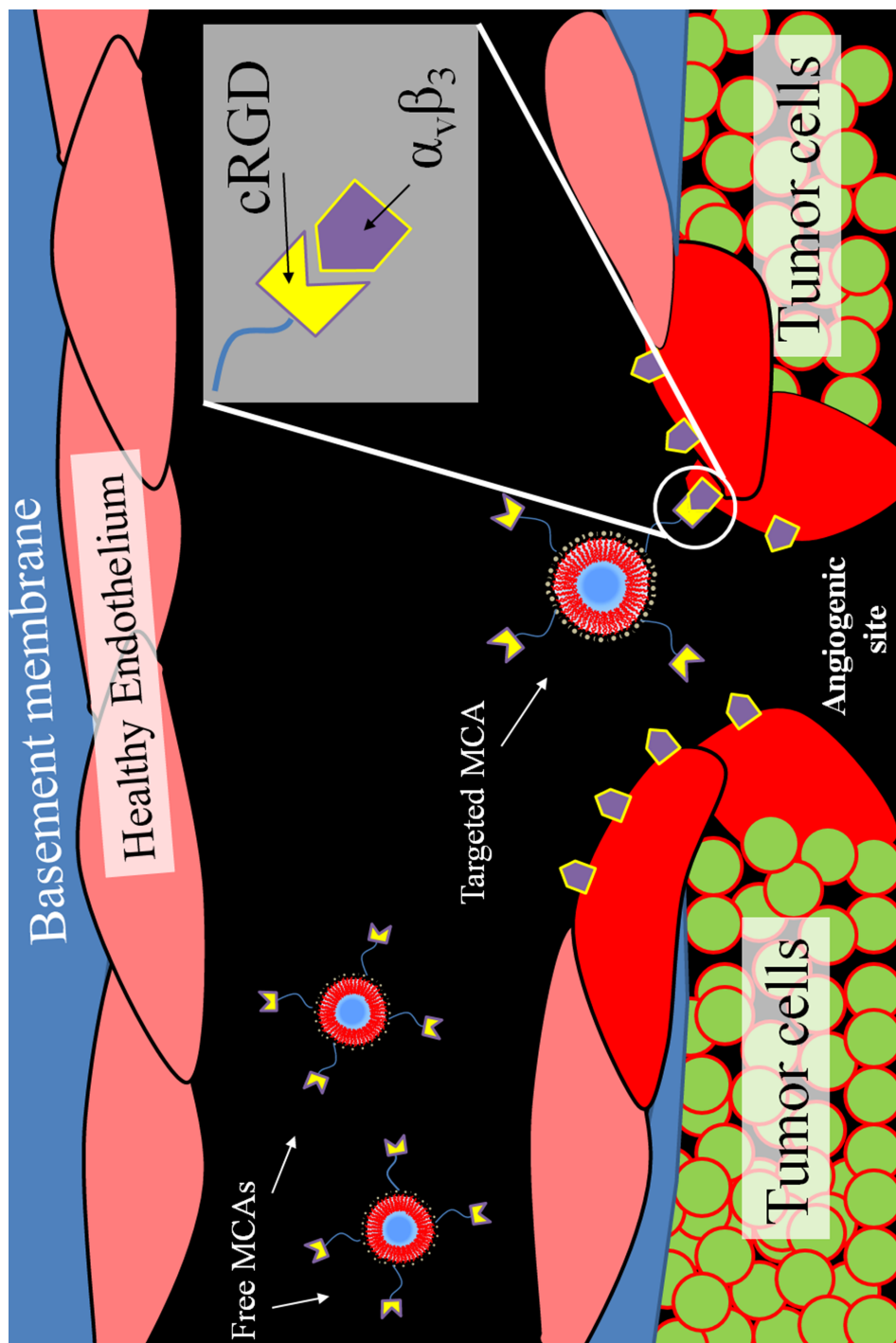


Figure 2.4: A cartoon illustration of the principles behind ultrasonic molecular imaging. In this example, a cRGD targeting ligand is used to bind to  $\alpha_v\beta_3$  integrins overexpressed at sites of angiogenic vasculature.

Molecular imaging with ultrasound is typically performed as follows: an ultrasound transducer is fixed in position over the region of interest with a mechanical arm to avoid motion artifacts from operator movement. A targeted contrast agent is administered into the peripheral vasculature, often through a tail vein during serial imaging studies in rodents. Prior to imaging, a waiting period of approximately 4-30 minutes is required, depending on contrast agent circulation characteristics.[54] During this period, there is a first phase when the targeted contrast agents accumulate in the microvasculature, followed by a second phase when freely circulating agents are cleared from the animal's system (Figure 2.5). After free agent clearance, imaging is performed to detect molecularly targeted contrast agents retained in regions of pathologic tissue. When possible, a first acquisition of several imaging frames is followed by a destruction pulse, which clears all contrast within the field of view. A second set of imaging frames can then be gathered as a no-contrast baseline to quantify image intensity increase due to molecularly targeted agents.

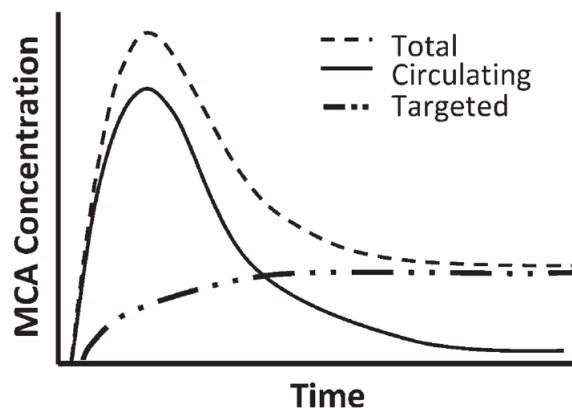


Figure 2.5: A cartoon graph illustrating how freely circulating and targeted microbubbles contribute to the overall concentration of contrast within an *in vivo* environment.[55] MCA = microbubble contrast agent.

### 2.2.2 Challenges in molecular imaging with ultrasound

Although ultrasonic molecular imaging has made significant progress over the last decade, this technology still faces several challenges before it can rise to its full diagnostic potential. It is the ideal goal of this technology to determine if a molecular target is present, and if so, to what degree. This requires that the contrast agents specifically adhere to their molecular target, and bind in quantities great enough to overwhelm the signal contributions from non-specific retention. Additionally, the ultrasound system should have sufficient sensitivity to detect the targeted agents present at the site of pathology, and be able to assess the pathology in its entirety. In this review, we hypothesize that several limitations have slowed the progression of ultrasonic molecular imaging - however, recent advances in contrast agent development, ultrasound technology, and detection strategies demonstrate the potential to substantially improve the capabilities and utility of ultrasonic molecular imaging. Two of these challenges are addressed in this dissertation: (1) low numbers of retained contrast agents and (2) ultrasound's limited field of view.

#### Low numbers of retained contrast agents

Since the magnitude of the detected ultrasound signal is a function of the quantity of contrast agents retained at the site of target endothelium it is intuitive that the retention of targeted contrast agents at a site of diseased tissue should be maximized, while non-specific contrast retention should also be minimized. For molecular imaging studies in small animals, the injected concentration of microbubbles is typically on the order of  $10^7$ - $10^8$  bubbles/kg. Prior studies assessing the adhesion of targeted microbubbles have observed only small amounts of targeted contrast retained *in vivo*, on the order of several bubbles per cubic millimeter.[56; 57] Correspondingly, video intensity due to targeted agents *in vivo* is typically only several fold higher than background.[58; 16; 59; 60]



It has also been proposed that radiation force might play a role in pulse sequences designed to enhance the detection of targeted contrast agents in molecular imaging. A transducer directing energy perpendicular to flow in a vessel can displace moving microbubbles to the wall of the vessel opposite of the sound source, and greatly enhance microbubble-endothelial interactions. It has been hypothesized that the ability to increase ligand-receptor proximity and reduce the velocity of flowing microbubbles would greatly increase the amount of targeted microbubble adhesion in molecular imaging studies [61; 62] (Figure 2.6).

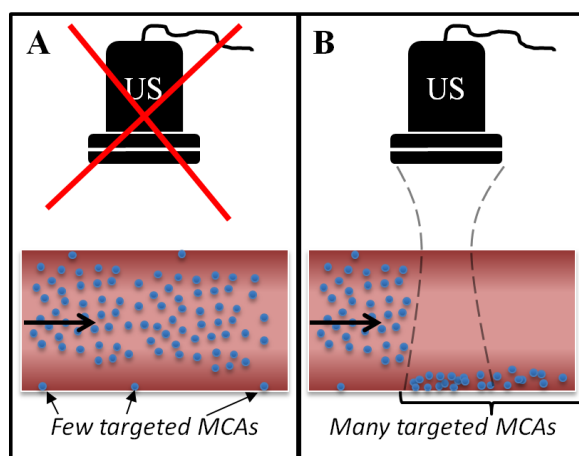


Figure 2.6: A cartoon illustration of radiation force enhanced microbubble targeting. A: no radiation force is administered, resulting in some passive targeting, but most microbubbles passing through unbound. B: radiation force is administered, greatly increasing the number of retained contrast agents.

### Limited field of view

One limitation of ultrasound imaging, in general, compared with modalities such as CT, MRI, PET, and SPECT is a smaller field of view. Until fairly recently, ultrasound imaging was largely a two-dimensional modality, depicting only a single image slice through tissue. In diagnostic imaging, the real-time imaging capability compensates for this, as it allows a sonographer to scan through the tissue of interest to view or measure target features. In ultrasonic molecular imaging, however, most current protocols

involve maintaining the transducer fixed in a clamp to observe the same slice of tissue. This is usually required because quantifiable measurement of signal from contrast involves a background subtraction after a destructive pulse, which creates artifacts in the presence of tissue or transducer motion. Recent advances in transducer technology have led to the implementation of matrix array transducers allowing real-time 3D ultrasound imaging (also called 4D, considering the time dimension). 3D ultrasound is still relatively new to the clinic, and is used primarily in obstetrics and cardiology. However, due to the complicated pulse sequences required to differentiate microbubble contrast agents from surrounding tissue, 3D contrast imaging has been challenging to implement on matrix array probes. Although some ultrasound system manufacturers currently have real-time 3D contrast imaging capability, the performance of contrast imaging modes on matrix array transducers still falls short of the resolution and contrast detection capability available on transducers for 2D imaging. Hence, to date ultrasonic molecular imaging has been largely limited to a single slice of tissue.

By acquiring multiple 2D images via a motorized stage and reconstructing the data offline, it has been hypothesized that heterogeneities within pathologic tissue volumes are observed that would be impossible to assess with traditional single-slice molecular imaging. 3D contrast imaging capabilities have been in development[63; 64] and continued improvements in low mechanical index, high resolution 3D imaging will eventually allow for the full volumetric characterization of tissue pathologies ensure consistent data collection in longitudinal studies.

## CHAPTER 3

### ACOUSTIC ANGIOGRAPHY - A NEW CONTRAST IMAGING APPROACH

The first section describes the characterization of the ultrasound transducers used throughout this dissertation (Chapter 3.1). The second section illustrates the implementation of the acoustic angiography imaging approach in *ex vivo* liver samples as a method to assess vascular architecture within these biomatrix scaffolds (Chapter 3.2). The final section presents several 3D datasets acquired of *in vivo* tissues and compares them to two other modalities for imaging preclinical vasculature: photoacoustics and CT (Chapter 3.3).

---

This chapter has three sections, some of which draw from previous published material. All previously published material was reprinted with permission from the publishers.

**Chapter 3.1:** Ryan Gessner, Marc Lukacs, Mike Lee, Emmanuel Cherin, F Stuart Foster, Paul A Dayton, *High-resolution contrast-enhanced imaging of the microvasculature using a dual-frequency transducer*, IEEE Trans Ultrason Ferroelectr Freq Control, 57(8):1772-81, 2010.

**Chapter 3.2:** Ryan C. Gessner, Steven Feingold, Avery Cashion, Ariel Hanson, Bryant Wu, Christopher Mullins, Stephen R. Aylward, Lola Reid, Paul A. Dayton. *New Ultrasound Perfusion Imaging Techniques Enable Functional Assessment of Biomatrix Organoid Scaffolds*. 2013. Submitted for publication.

**Chapter 3.3:** unpublished pilot studies.

### 3.1 Evaluating a prototype dual-frequency transducer

Recently, dual-frequency excitation-detection been demonstrated by using either two confocal transducers, or alternating elements in a linear array [65; 66]. Bouakaz demonstrated that a contrast-to-tissue ratio of 40 dB over conventional b-mode imaging could be attained using a dual-frequency imaging technique with excitation at 0.8 MHz and detection at 2.8 MHz [65]. Kruse demonstrated that when the bubbles were excited with several hundred kilopascals at 2.25 MHz, broadband frequency content could be detected from the contrast agents as high as 45 MHz [66]. These initial studies by Kruse provided the proof-of-concept for implementing the dual-frequency imaging method with higher frequencies suitable for implementation in small animal imaging studies. A dual-frequency approach enables the use of low frequencies to excite microbubble contrast agents, with simultaneous detection of the broadband backscatter produced by oscillating or fragmenting bubbles, preserving high spatial resolution while suppressing background from tissue. It became clear throughout this study that high resolution high contrast images resulted from this dual-frequency excitation-detection approach, and thus we hereafter refer to our specific pulsing and receiving scheme as ‘acoustic angiography.’

For *in vivo* acoustic angiography imaging, we have designed a prototype dual-frequency imaging transducer which has been integrated with a Vevo770 small animal imaging system (VisualSonics, Toronto, ON, Canada). In this section, we present

---

Note: This section was written in 2009 when only one dual-frequency prototype probe - hereafter referred to as the ‘generation 1’ probe - was built. Later, improvements were made and a second transducer - the ‘generation 2’ probe - was manufactured. Thus most of the data herein was acquired for the generation 1 probe, though the beamfields were later acquired when the generation 2 probe was tested and retroactively added to Figures 3.2 and 3.3. These will illustrate that the second generation probe’s beam alignment was superior, and all subsequent studies were performed with the generation 2 probe.

results from initial studies on the performance of the dual-frequency probe from several studies performed in rats. Our studies assess contrast-to-tissue ratios compared with traditional high-frequency b-mode imaging, and sensitivity to tissue motion compared with image subtraction and power Doppler, common methods utilized to detect contrast agents at high frequencies. Our acoustic angiography imaging strategy provides improved contrast over traditional high-frequency b-mode imaging as well as a reduction in sensitivity to animal motion compared with both image subtraction and power Doppler methods. Additionally, we examine the capacity of the probe to produce acoustic radiation force, which is maximized on microbubbles when excited near their resonant frequency [62]. Radiation force has been demonstrated to enhance the delivery of acoustically-active drug delivery vehicles [67; 68], and hypothesized to enhance the retention of targeted contrast agents [69; 70].

### **3.1.1 Materials and methods**

#### **The dual-frequency probe**

The confocal imaging probe designed by our group is an adaptation of a VisualSonics RMV707 ultrasound probe and is used with a VisualSonics Vevo 770 micro-imaging system, a commonly implemented preclinical ultrasound imaging system. Traditionally, the high-frequency piston transducer element within the RMV probe mechanically sweeps to obtain images. An additional 2.5 MHz transducer was added confocally outside the inner 30 MHz element in the adapted setup (Figure 3.1b). This outer low-frequency transducer enabled us to transmit at a frequency near microbubble resonance, while receiving the emitted high-frequency signal content with the inner transducer. A schematic displaying how the waveforms were delivered and received by the setup can be seen in Figure 3.1a.

After the low-frequency pulses are delivered into the animal, the 30 MHz inner

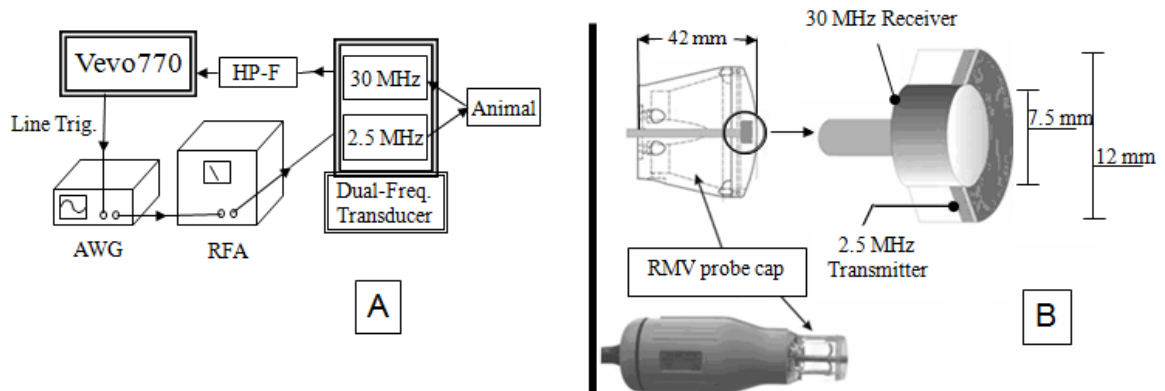


Figure 3.1: (A) Schematic for the operation of the prototype dual-frequency transducer. The arbitrary waveform generator (AWG) (Sony Tektronix) was triggered to send 512 low-frequency pulses through the RF amplifier (RFA) within each frame of image data by the Vevo770 line trigger. (B) A diagram displaying how the two confocal elements were constructed within the RMV probe scanhead.

element receives the reflected ultrasound signal. The unwanted backscatter of tissue is suppressed by sending each line of raw RF data through a seventh-order 10 MHz high-pass filter (HP-F, in the Figure 3.1) (TTE Inc., Los Angeles, CA) before being displayed and saved by the ultrasound imaging system.

### Characterizing the probe

Using a 40- $\mu\text{m}$  needle hydrophone (Precision Acoustic, Dorchester, UK) and a 3D motion stage, the beam-fields of the dual-frequency probe's two individual elements were measured at their foci. The pressure outputs of the two elements were also measured relative to the center of the high-frequency element. To determine the resolution achievable with our acoustic angiography imaging approach, two studies were performed. One of these studies was based on the collected RF data from single microbubble contrast agents, which enabled us to make estimations about the theoretical limits, or best case for axial resolution using our imaging parameters. The second study was based on video data collected from single bubbles, which allowed us to determine the point

spread function of our imaging system and thus determine the practical lateral and axial resolutions achievable in actual ultrasound studies implementing our parameters. Axial and lateral are defined as the parallel and orthogonal directions of wave propagation respectively. Within an image, axial represents the depth axis.

For the first resolution study, a dilute concentration of microbubble contrast agents was pumped through a 27-gauge needle tip coupled to a 380  $\mu\text{m}$  polyethylene tube (Becton Dickinson, Sparks, MD), which was then coupled to a 200  $\mu\text{m}$  capillary tube (Spectrum Labs, Rancho Dominguez, CA) The transducer was set to acquire data with a frame rate of approximately 1 Hz and bubbles were pumped through the capillary tube at 1 mL/h, which corresponded to a linear flow velocity of 9 mm/s. RF data was collected with the 30 MHz element of individual bubble responses for single cycle excitations at 2.5 MHz and at peak negative pressure of 617 kPa. After more than 100 bubble responses were acquired, the time-domain signals were Fourier transformed and averaged together in the frequency domain. Once all pulses had been averaged, the mean frequency-domain signal was then inverse-Fourier transformed to yield a mean time-domain signal. The envelope of this mean signal was determined using Matlab (The MathWorks, Natick, MA), via the absolute value of the Hilbert transform, and the full-width at half-maximum (FWHM) of the envelope used to yield the theoretical limit of the axial resolution for acoustic angiography imaging at our pulsing and receiving parameters.

For the second resolution study, a dilute concentration of bubbles was pumped through a setup similar to the one described for the first resolution study. The tube was oriented horizontally and imaged at 2.5 MHz at a 1 Hz rate. The video data were exported as uncompressed AVI files and analyzed offline in Matlab. Because the concentration of bubbles was dilute, not all frames contained images of bubbles, though in each video frame containing a bubble, its center was manually defined. The vertical and

horizontal cross-sections through this point were extracted from the image data (representing the axial and lateral components of the point spread function, respectively), interpolated, and the FWHM in each dimension was determined. Thirty samples were collected and averaged. The mean FWHMs in each direction-lateral and axial-were taken as their respective directional resolutions.

### **Animal and contrast agent preparation**

A total of eight Sprague-Dawley rats (Harlan Laboratories, Indianapolis, IN) were imaged in the course of this study: three during the contrast-to-tissue comparison study and five during the sensitivity to motion study. Before all imaging studies, animals were prepared in the same way. Each animal was first anesthetized in an induction chamber by introducing a 5% aerosolized isoflurane-oxygen mixture. Once sedated, the animal was removed from the induction chamber, the isoflurane concentration reduced from 5% to 2% and maintained via mask delivery. Its abdomen was shaved and a depilating cream was applied to the animal's skin to dissolve any remaining hair. A 24-gauge catheter was inserted into the animal's tail vein for the administration of microbubbles. The animal was then placed in dorsal recumbancy on a heating pad. Finally, ultrasound coupling gel was placed between the imaging transducer and the animal's skin to ensure the quality of signal transmission. Animals were handled according to National Institutes of Health guidelines and our study protocol was approved by the UNC Institutional Animal Care and Use Committee.

The microbubbles used in this study were the perfusion agent formulation made with a lipid shell and perfluorocarbon core (Appendix A). Contrast agents were diluted in sterile saline to result in a final concentration of  $2.2 \times 10^9$  bubbles/mL (unless otherwise stated) and a mean diameter of  $0.9 \pm 0.45 \mu\text{m}$ , determined with a particle-sizer (Accusizer 780A, Particle Sizing Systems, Santa Barbara, CA).



## Determining contrast-to-tissue ratios

Two studies were performed to examine how imaging pressure affected the probe's sensitivity to contrast. This sensitivity was quantified with the measure of contrast-to-tissue ratio (CTR). The first study was performed *in vitro*, and was designed to determine the acoustic responses of both tissue and contrast agents when subjected to the imaging parameters utilized by our probe. The second study was an *in vivo* study, which compared the CTRs achieved by the probe operating in both high-frequency and acoustic angiography imaging modes within an actual tissue environment.

### 1) *In Vitro CTR Study*

For the *in vitro* CTR study, individual microbubbles in a flow phantom were imaged in acoustic angiography mode at four different mechanical indices (MIs) between 0.33 and 0.57. Bovine muscle tissue was also imaged at the same parameters to simulate the acoustic response of non-perfused tissue. The lines of RF data from these scans were Fourier transformed and divided by the frequency bandwidth of the receiving element. This allowed us to appropriately weight the frequencies in the measured signal which were higher and lower than the probe's 30 MHz fundamental frequency. By doing this, we were able to compare the spectral power of the true bubble and tissue signals and thus, to compute a theoretical CTR versus frequency plot for multiple imaging pressures (regardless of our specific receiving element's sensitivity).

### 2) *In Vivo CTR Study*

Three animals were imaged for the CTR study. Their kidneys were selected as the imaging region of choice because of the organ's high degree of vascularization, thus providing an opportune target to image large numbers of injected microbubbles. Each animal had both kidneys imaged in both acoustic angiography and high-frequency modes, resulting in six independent trials. Contrast agents were delivered at a continuous infusion rate

<b>AA</b>		<b>HF</b>	
<b>PNP (kPa)</b>	<b>MI</b>	<b>PNP (kPa)</b>	<b>MI</b>
292	0.18	978	0.18
391	0.25	1318	0.24
492	0.31	1935	0.35
617	0.39	2347	0.43
716	0.45	2792	0.51
814	0.51	3295	0.60
900	0.57	3514	0.64
1030	0.65	3881	0.71

Table 3.1: A Summary of the Imaging Pressures and Mechanical Indices Used in the *In Vivo* Contrast-to-Tissue Study for Acoustic Angiography and High-Frequency Imaging Modes.

**AA:** ‘Acoustic Angiography’ (transmit 2.5 MHz)

**HF:** ‘High Frequency’ (transmit 30 MHz)

of 3 mL/h using a syringe pump (Harvard Apparatus, Holliston, MA). The microbubble solution was allowed one minute to reach equilibrium before any image data was collected. Approximately 20 video frames were acquired at 2 Hz in both high-frequency and acoustic angiography modes at each of the six imaging locations. The acoustic angiography mode was operated with a 2.5-MHz pulsing frequency and a 30-MHz receiver element. The high-frequency imaging mode was operated with pulse-echo only from the 30-MHz element. Both imaging modes used one-cycle sinusoidal driving pulses. Different image pulsing pressures were evaluated in both imaging modes, as summarized in Table 3.1.

For analysis of CTR at each tested parameter, the onboard software of our ultrasound system was utilized after all data had been collected. Regions of interest (ROIs) were defined for both contrast and tissue regions for each kidney imaged. The centers of all ROIs were defined within 1 mm of the transducers’ foci to ensure that we were consistently sampling from imaged regions of tissue that had received a similar amount of acoustic energy. Although different ROIs for both tissue and contrast regions were defined for the six different kidneys imaged, the same ROIs were applied to the data

sets collected in each of the kidneys at the different imaging parameters. B-mode images were acquired before and after each administration of contrast agents to ensure consistency of the contrast and tissue ROIs used for each kidney over time (i.e. to ensure they were not corrupted by global shifts in tissue). The mean pixel intensity in the ROIs were calculated at each imaging parameter and compared between animals.

### **Determining sensitivity to motion**

To test the robustness of the acoustic angiography method in the presence of respiratory motion, five animals were imaged with power Doppler, image-subtraction, and acoustic angiography imaging modes. The imaging protocol consisted of administering 150  $\mu$ L bolus injections of microbubble contrast agents, and observing the kidney without respiratory gating as the contrast washed out of the system. The goal was to examine the different imaging modes' abilities to detect the sharp increase in video intensity following the introduction of microbubbles into the renal volume, as well as their consistency in monitoring the steady decrease in intensity as the contrast agents were cleared from the different animals' systems. To record the entire contrast washout curve, the left kidney of each animal was imaged for at least 6 min following each injection. All three imaging modes were tested within the same anatomical region of each animal (meaning neither the animal nor the transducer was moved between data acquisitions with different imaging modes). Following the collection of data, videos were exported and examined offline in Matlab for analysis of these curves.

### **Production of radiation force**

The ability of the dual-frequency probe to produce radiation force was tested *in vitro* in a water bath. microbubbles were prepared and pumped through a 200  $\mu$ m cellulose tube using a syringe pump (Harvard Apparatus, Holliston, MA) at several different constant volumetric flow rates. These flow rates are summarized in Table 3.2 along

with the corresponding linear flow velocities.

<b>V-FR (mL/h)</b>	<b>L-FR (mm/s)</b>	<b>Analogous environment</b>
9.05	200	Large artery
1.81	40	Small artery
1.81	40	Large vein
0.90	20	Arteriole
0.45	10	Small vein
0.14	3	Venule
0.01	0.3	Capillary

Table 3.2: A summary of the range of blood velocities in different vasculature types. Modified from [71]. These velocities formed the basis for the tested range of flow velocities of contrast agents undergoing radiation force.

**V-FR:** ‘Volumetric flow rate’

**L-FR:** ‘Linear flow velocity’

The tube was oriented horizontally, and was located at the focus of both the dual-frequency probe and a high-speed camera (APX-RS, Photron, San Diego, CA) equipped with a 60x water immersion lens (LUMPlanFI/w, Olympus, Melville, NY). The axes of the camera and the transducer were perpendicularly aligned with the tube at the same location. This dual-focus setup was achieved by positioning a needle hydrophone in the optical focus, and aligning the pulsing transducer such that the measured signal from the hydrophone was maximized. The microbubble solution was then pumped through a 200  $\mu\text{m}$  tube at the different flow rates and exposed to 200-cycle low amplitude pulses [peak negative pressure (PNP)  $\sim 13$  kPa] at 4 MHz and a pulse repetition frequency of 15 kHz. This frequency was out of the optimal bandwidth of the low-frequency element, but was chosen to reduce bubble destruction. The effects of these pulses were observed in real time as well as recorded to later confirm the efficiency of the radiation force pulses offline.

### 3.1.2 Results

#### Characterizing the probe

The -6 dB beamwidth in the focal planes of the 30-MHz and 2.5-MHz transducers were determined to be 0.21 mm and 0.51 mm, respectively. The results of the beamfield maps acquired for each element can be seen in Figure 3.2. The axial -6 dB focal regions (depths of field) were determined to be 2.7 mm and 10.3 mm for the two respective elements. The experimentally determined limit of axial resolution, measured using the FWHM of the RF data for averaged microbubble bubble responses, was  $95 \pm 3.47 \mu\text{m}$ . The uncertainty in this measurement is the standard deviation of the FWHMs collected at the different mechanical indices tested ( $N = 8$ , between MI of 0.28 and 0.57). There was not a significant trend observed in this value with increasing low-frequency MI. The experimentally determined lateral resolution of the probe operating in acoustic anigraphy mode, as estimated from the average FWHM of a horizontal profile taken through a bubble response in multiple frames of video data, was  $296 \pm 67 \mu\text{m}$ . Likewise, the experimentally determined axial resolution was determined to be  $161 \pm 31 \mu\text{m}$  via the mean FWHM in the vertical profiles acquired in the same method. The uncertainty in these measurements is the standard deviation of the FWHM values ( $N = 32$  for both).

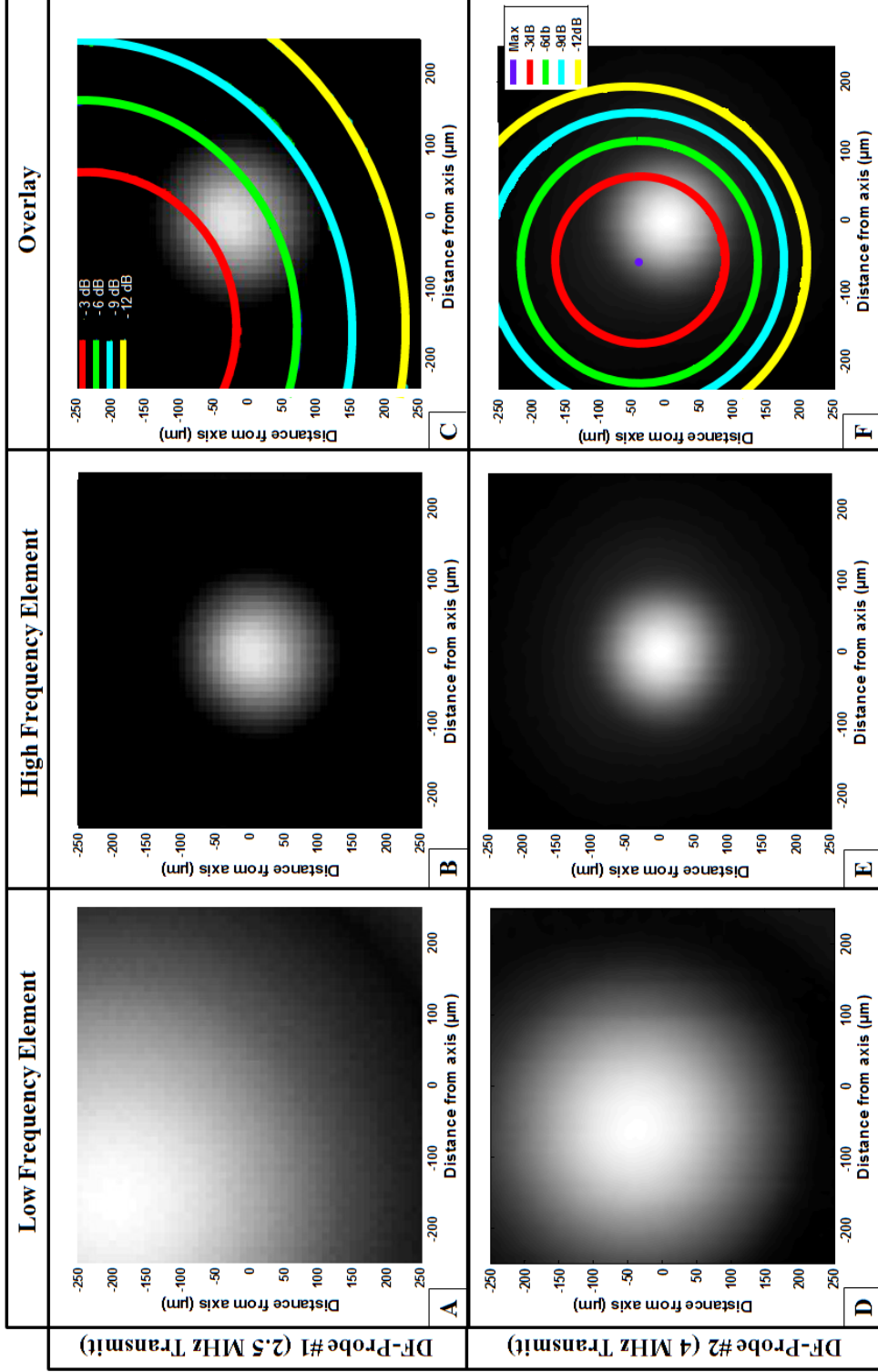


Figure 3.2: Beam field maps acquired centered around the acoustic focus of the 30 MHz element. Data from both the first (top) and second (bottom) generation dual-frequency ultrasound transducers. All data in this chapter was acquired with the first generation (2.5 MHz transmit). The second generation probe had a better alignment and an increase in pulsing frequency.

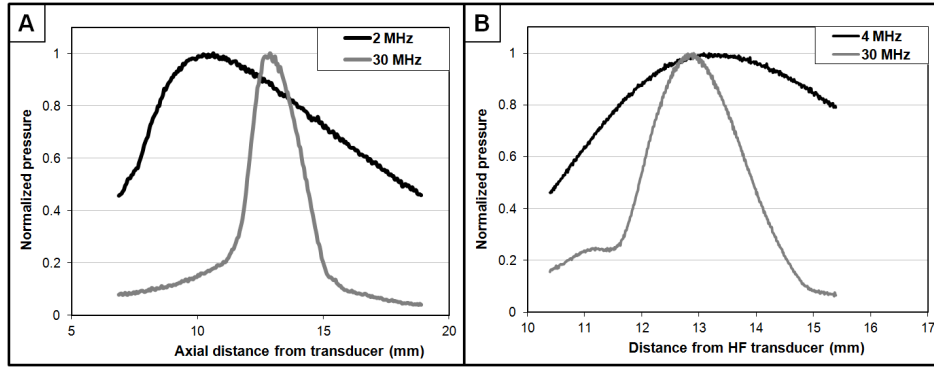


Figure 3.3: Axial dimension pressure maps for both (A) first generation and (B) second generation dual-frequency transducers.

### Contrast-to-tissue ratios: *in vitro*

The acoustic responses of both bubbles and tissue were used to create a measure of CTR versus receive frequency at several different mechanical indices for the imaging pulses. To illustrate the difference between the types of signals received from microbubbles and from tissue, time domain plots are provided (Figure 3.4). These data were acquired using the maximum transmit mechanical index for the study ( $MI = 0.65$ ).

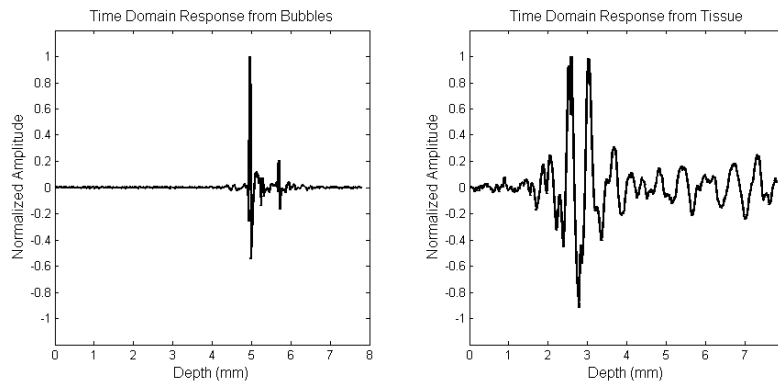


Figure 3.4: These data illustrate the difference between the nonlinear and nearly delta-function response from microbubbles (left) and more linear response from tissue (right). Speed of sound assumed to be 1540 m/s for conversion to distance.

To illustrate the frequency domain characteristics of these data, the Fourier transformed data are provided (Figure 3.5) with the receive transducer’s bandwidth superimposed for reference.

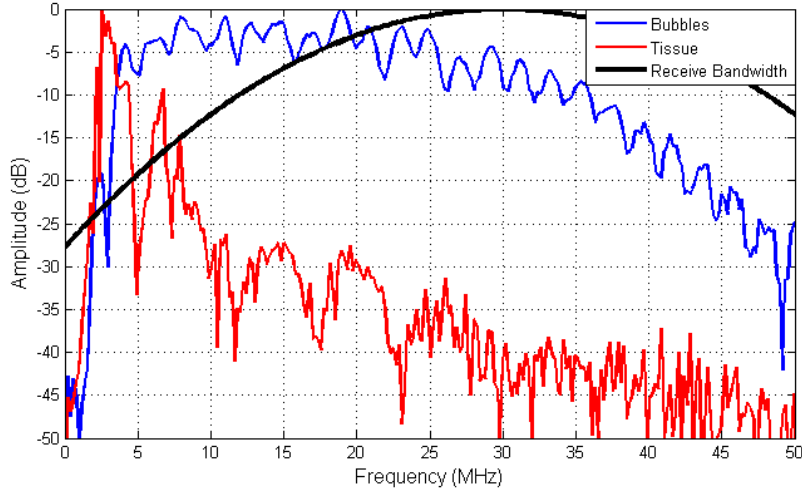


Figure 3.5: Frequency responses of the single lines of microbubble (blue) and tissue (red) RF data seen in Figure 3.4. The transducer’s receive bandwidth is approximated as a Gaussian with 100 percent bandwidth centered at 30 MHz.

CTR data was computed as the ratio of the averages of the frequency domain data seen in Figure 3.5 (i.e. Figure 3.5 shows the Fourier transform of single RF lines, whereas these frequency domain data were averaged over many acquisitions for the CTR plots). The CTR data can be seen in Figure 3.6a. The signals from both the microbubbles and tissue were corrected for the receiving element’s bandwidth to measure the ratios of their spectral content irrespective of the imaging system used to detect the signals. The data shows improved CTR with increasing mechanical index. The CTR versus frequency plots also demonstrate this improved contrast sensitivity relative to tissue with increasing mechanical index. Between the mechanical indexes tested, a similarly decreasing slope of 1 dB/MHz is observed throughout the bandwidth of the probe. The decibel values in Figure 3.6a are relative to the tissue responses at each frequency and MI.



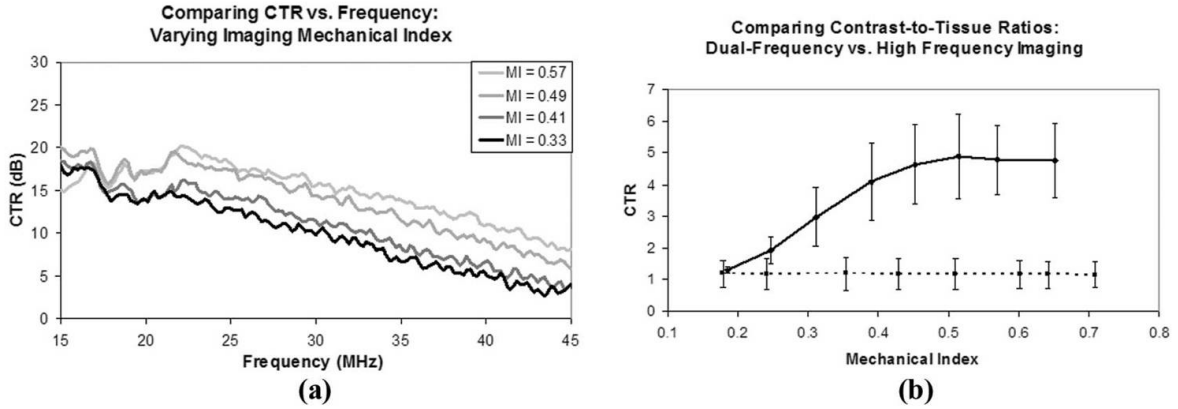


Figure 3.6: (A) Contrast-to-tissue ratios measured *in vitro* as a function of frequency at several different mechanical indices of incident pulses. Decibel values are relative to the tissue response at each frequency and MI. (B) Contrast-to-tissue ratios measured *in vivo* in six different kidneys which were imaged in both high-frequency b-mode (dashed line) and acoustic angiography mode (solid line).

### Contrast-to-tissue ratios: *in vivo*

The video data collected from contrast enhanced ultrasound studies on both kidneys of three different animals in both traditional high-frequency b-mode and acoustic angiography imaging modes were analyzed to determine CTR in an *in vivo* environment. Both a 2D slice and a 3D maximum intensity projection of a kidney imaged in acoustic angiography mode can be seen in Figure 3.7, providing a representative view of the extent of tissue suppression provided by this imaging method. In a 2D image slice of each kidney, ROIs were selected around regions of tissue and contrast for both the acoustic angiography and high-frequency imaging studies, and these values were used to determine the CTR at each imaging pressure. These values are plotted in Figure 3.6b.

The CTR in the high-frequency *in vivo* imaging studies was nearly constant as a function of pressure, with an average value of  $1.18 \pm 0.01$ . Across the pressures studied (1000 to 4000 kPa), the mean pixel intensity within regions of contrast flow were only 18% greater than those of tissue. The mean *in vivo* CTR values obtained in the

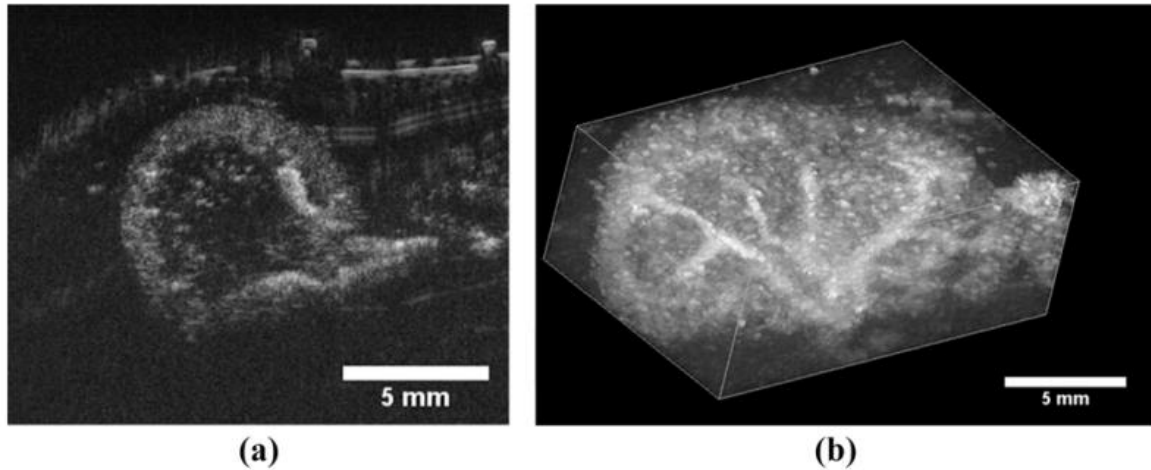


Figure 3.7: (A) A 2D transverse slice through a rat kidney with contrast agents seen entering the volume through the large renal vasculature. (B) A 3D maximum intensity projection through a rendered volume of sequential image slices as seen in (A). The multiple 2D slices were acquired using a translational motor stage with step sizes of  $200 \mu\text{m}$ . The images analyzed in the CTR portion of this study were identical to the cross-sectional slice seen in (A).

acoustic angiography mode ranged between 1 and 5 for the pressures tested, with a linear increase between  $\text{MI} = 0.19$  and  $0.51$  (290 and 813 kPa) with a slope of  $0.0074 \text{ kPa}^{-1}$  ( $R^2 = 0.97$ ). At acoustic angiography imaging pressures higher than 813 kPa, the CTR data leveled off and approached an average value of 4.8. Thus, at pressures greater than approximately 800 kPa, the acoustic angiography imaging method resulted in an average 12.3 dB improvement in CTR, compared with high-frequency b-mode imaging, for this range of mechanical indices. The maximum improvement in CTR between two images acquired from the same anatomical location with acoustic angiography imaging mode compared with high-frequency b-mode was 17.2 dB at a low-frequency MI of 0.51.

## Sensitivity to motion

Within the seven sets of image data collected in five different animals with power Doppler, image subtraction, and acoustic angiography imaging modes without respiratory gating, acoustic angiography imaging was significantly more robust at monitoring the presence of microbubbles. Because of the artifacts in the video data resulting from respiratory motion, the image-subtraction method was unreliable without respiratory gating. In this mode, the changes in video intensity caused by tissue motion were approximately the same amplitude as the signal from the circulating contrast, and we were only able to observe a decay slope of the contrast washout in the kidney ROI in one of the animals.

Similarly, 5 of 7 imaging studies using power Doppler were corrupted to the point that a washout curve could not be acquired. Examples of how these imaging modes were corrupted by breathing motion can be seen in Figure 3.8. In contrast, the acoustic angiography imaging experiments ( $N = 7$ ) produced a defined contrast washout curve in each case despite substantial respiratory motion. Figure 3.9 illustrates the relative success rates for the different imaging strategies, with acoustic angiography mode demonstrating a 3.5- and 7-fold improvement over power Doppler and image-subtraction, respectively.

## Production of radiation force

Using a dual optical-acoustic focus and contrast agents flowing in a 200- $\mu\text{m}$  cellulose tube, we have verified that the probe is capable of applying radiation force *in vitro*. The transducer was aligned above the tube and the incident radiation force pulses were capable of pushing a polydisperse distribution of flowing microbubbles perpendicular to their direction of motion against buoyancy. The proficiency of these sequences of radiation force pulses, administered with a single 3-second sweep, was tested at several

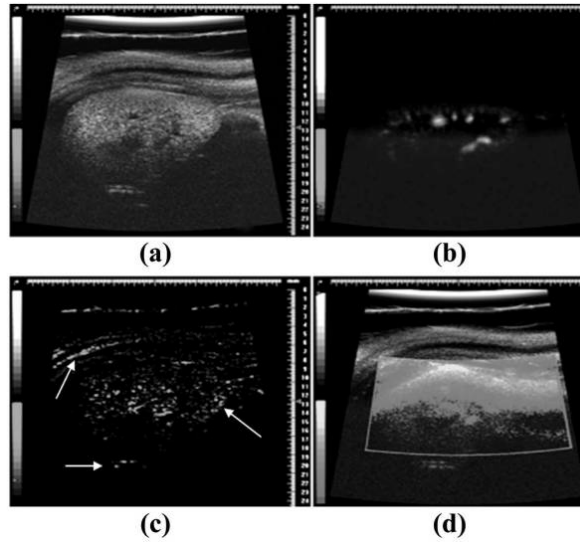


Figure 3.8: Example image data collected from the same animal without respiratory gating enabled. (A) B-mode imaging before the introduction of contrast agents. (B) Acoustic angiography data while contrast is circulating. (C) Image-subtraction frame while contrast is circulating. Note the strong artifacts near the tissue borders (indicated by white arrows). (D) Power Doppler with contrast circulating. Small regions of enhanced contrast can be seen near the bottom of the image, although most of ROI is washed out by motion artifact.

different linear flow velocities between 0.3 and 200 mm/s, as summarized in Table 3.2. The radiation force pulses from the probe were able to divert the flow of contrast agents a distance of 200  $\mu\text{m}$ -the diameter of the tube-at all linear flow velocities less than 50 mm/s. At flow rates faster than this, the direction of the microbubble stream was perturbed, though did not significantly divert within the viewing window of 500  $\mu\text{m}$ . At 200 mm/s, the stream was only estimated to divert approximately 50  $\mu\text{m}$  at our push parameters. The ability to divert the stream is well visualized with time-axis projections, an example of which is seen in Figure 3.10. In this image, the mean intensities of movie pixels throughout the time of data collection are mapped to pixels in a single 2D image.

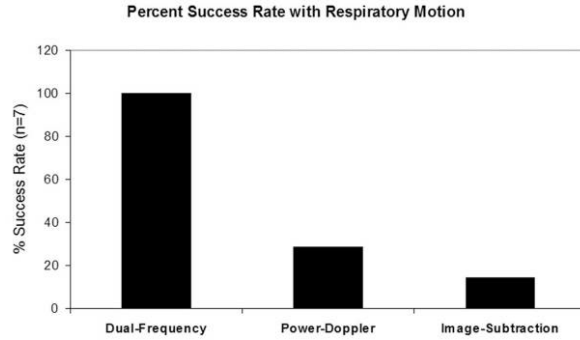


Figure 3.9: A plot comparing the abilities of the three different imaging modes to monitor contrast flow in the presence of respiratory motion. Values are expressed as a percentage of the seven attempted trials. Note: ‘Dual-frequency’ = acoustic angiography

### Potential for bioeffects

The interactions between ultrasound pulses and microbubble contrast agents have been shown in the past to potentiate bioeffects, both in *in vitro* assays as well as *in vivo* imaging studies. The following (Figure 3.11) is an overview of some recent studies performed using various commercially available contrast agents (Optison, Levovist, Definity, among others), insonified at a range of mechanical indexes. These studies (references in Figure 3.11 caption) represent data from a wide range of subjects (rat, human, mouse), anatomical locations (muscle, lung, tumor, kidney), and acoustic pulsing schemes (continuous wave Doppler, b-mode, harmonic imaging mode) and peak rarefactional pressure amplitudes. The specific pressures and frequencies used by our lab’s prototype dual-frequency transducers are also displayed on this plot, in addition to the pressure thresholds above which bioeffects have been observed. This data suggests that the two probes are unlikely to be causing adverse *in vivo* effects from microbubble contrast agent cavitation, though this has not been explicitly tested with these specific probes.

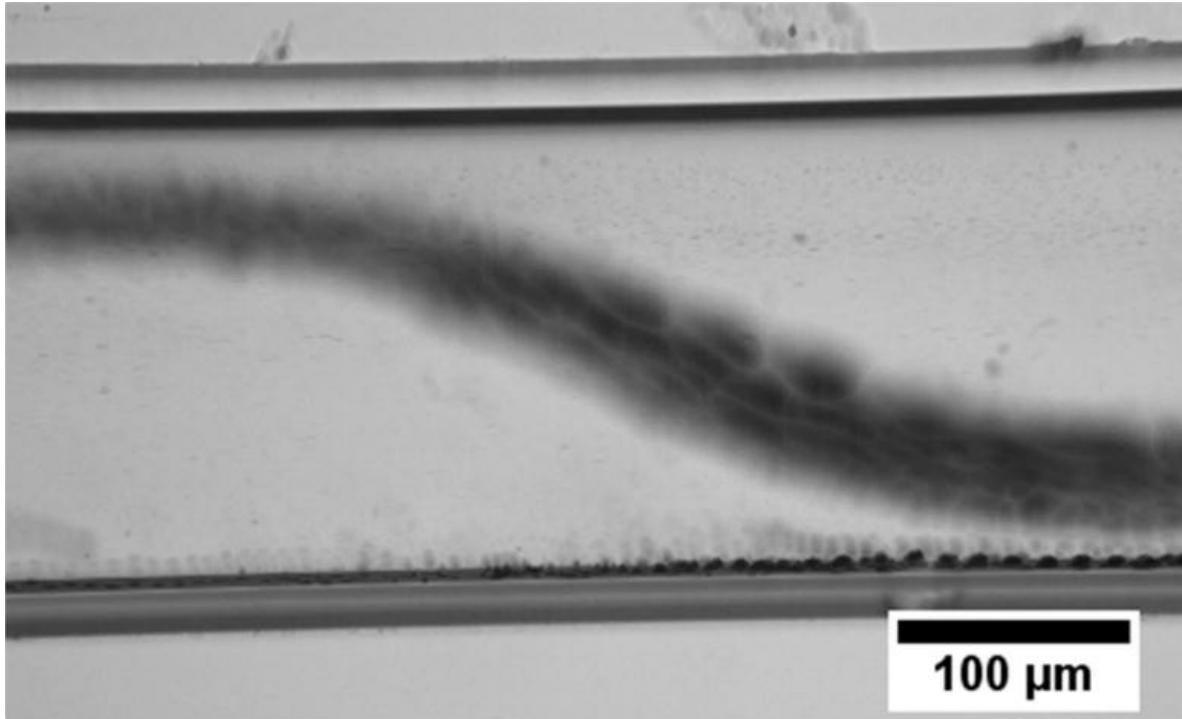


Figure 3.10: A time-axis projection image produced from bright-field optical video data, which demonstrates the proficiency of the dual-frequency probe at diverting a moving stream of microbubbles. The linear flow velocity in this image was 40 mm/s, a comparable speed to a human small artery or large vein.

### 3.1.3 Discussion

Based upon the work of Kruse et al. [66], we hypothesize that the high-frequency energy that we are detecting from the microbubbles is generated during the rapid collapse of the gas core during the low-frequency driving pulse. In the frequency domain, these emitted acoustic transients were confirmed to be very broadband, as seen in Figure 3.6a, allowing them to be detected at frequencies far away from the fundamental.

The 3D hydrophone scans performed to map the beam-fields of our dual-frequency probe's two elements revealed that the inner and outer elements were misaligned. Neither transducers' focus perfectly overlapped the center of the z-axis of the mechanically scanning arm, with the low-frequency element having an off-axis misalignment of 255

**Comparison of Gen 1 and Gen 2 transducers' pulse parameters to bioeffect-inducing pulse parameters**

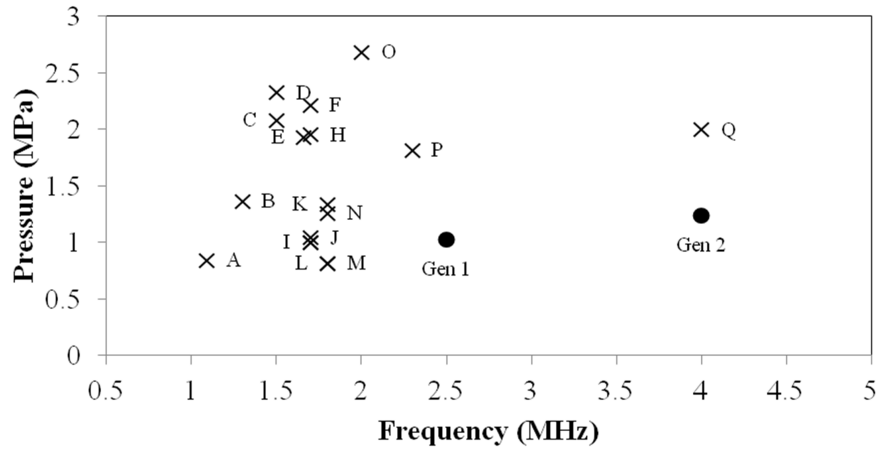


Figure 3.11: An overview of bioeffect-inducing acoustic parameters. These studies are referenced as follows. A:[72], B:[73], C:[74], D:[75], E:[76], F:[77], G:[78], H:[79], I:[80], J:[81], K:[82], L:[83], M:[84], N:[85], O:[86], P:[87], Q:[85].

$\mu\text{m}$  compared with the high-frequency element's 16  $\mu\text{m}$ . There were several consequences of this misalignment. One issue with this was that the focus of the 30-MHz element overlapped the 2.5-MHz element approximately -6 dB from the focus, and hence the signal intensity from the microbubbles detected during acoustic angiography mode was substantially less than optimal. One other consequence was that the microbubbles were rapidly destroyed outside of the imaging region because of a higher pressure at the focus of the misaligned 2.5-MHz transducer. This resulted in differences in the contrast intensity depending on whether the transducer was scanning with the focus of the 2.5-MHz element preceding or following the imaging element.

Another limitation of the prototype probe compared with the standard mechanically scanned probes made by VisualSonics was the reduced maximum frame rate. The maximum sweep speeds of for RMV probes vary between 25 and 75 Hz, depending on the model of the probe and the imaging depth of field, however, the speed of the prototype probe was limited as a result of the increased mass incurred by the outer confocal element to 20 Hz.

For all imaging pressures tested, the CTR versus frequency curve peaked at approximately 15 MHz, and decreased from there with increasing frequency (Figure 3.6). This decline in CTR was caused by the decrease in spectral power of the acoustical transients at the higher frequencies, because the spectral power of the tissue signal quickly approached the noise floor above the fundamental imaging frequency of 2.5 MHz. The CTR increased uniformly across all frequencies in the bandwidth of the receiving element with increasing imaging MI, which can be attributed to more violent collapses of the microbubble gas cores at increasing pressures.

The results obtained during the *in vivo* CTR portion of the study showed that the acoustic angiography imaging method could be used in animal studies to improve contrast sensitivity over conventional high-frequency imaging methods. High-frequency b-mode imaging showed little improved contrast signal over tissue signal regardless of imaging pulse pressure. The average CTR in high-frequency b-mode was 1.18. Acoustic angiography imaging of the same animals and the same imaging locations showed a linearly increasing trend in average CTR ranging from 1.3 to 4.8, increasing as a function of increasing imaging pressure. After approximately 800 kPa, the rate of increase in the contrast signal was similar to that of the tissue signal and the CTR did not noticeably improve at higher imaging pressures.

There was an approximately 10-fold difference between the *in vitro* and *in vivo* CTR studies when implementing acoustic angiography imaging at the pressures listed in Table 3.1. It is important to note that the *in vitro* analysis of CTR was performed without consideration for several realities present in the *in vivo* study, and in all ultrasound imaging exams. The simplifying factors of the *in vitro* setup which artificially enhanced the measured CTR were, namely, the absence of signal attenuation expected to occur in a tissue medium, and the analysis of RF data mitigated the loss of signal



information inherent in any imaging system's compression and video-data display algorithms. Instead, this data served to provide a basic understanding of the acoustic responses of microbubbles and tissue at frequencies higher than previously examined.

In Figures 3.7 and 3.8b, it is clear that the larger vasculature within the kidney is brighter and better delineated from the surrounding tissue than smaller blood vessels. Thus the contrast provided by our acoustic angiography imaging method appears to be, predictably, a function the quantity of contrast agents present within the imaging ROI. If the probe is to be operated within a destructive pressure regime for microbubbles (a range which provided the best contrast within our *in vivo* CTR study [88]), one potential limitation of our imaging strategy would be the need to delay imaging pulses to allow contrast refresh within the micro-vasculature. This decreased frame rate would be beneficial for imaging tissues with slow perfusion times.

The acoustic angiography method was compared with power Doppler and image-subtraction, two common methods to monitor the presence and flow of contrast with ultrasound on high-frequency imaging systems. Power Doppler is very effective at detection of contrast agents because of the high-amplitude post wall-filtered power produced by moving or breaking bubbles. However, as a result of this detection strategy, power Doppler also proved very sensitive to tissue motion. Image-subtraction, another method to monitor contrast presence, compares a pre-contrast baseline image to contrast enhanced images on a pixel-by-pixel basis, and likewise proved very sensitive to tissue movement. This tissue motion resulted in many pixels differing from their original baseline values, yielding substantial artifacts, especially along boundaries between tissue types, as indicated by the white arrows in Figure 3.8(c). Our results suggest that both of these methods require respiratory gating to produce consistent results in a high-tissue-motion environment. Even when respiratory gating was enabled, implementing these two imaging methods could be a challenge if tissue motion is excessive,

because global tissue migration will invalidate the original pre-contrast baseline images. Acoustic angiography imaging, on the other hand, exploits the nonlinear response of microbubbles to enhance contrast signal intensity and thus proved significantly more robust in the presence of respiration-induced tissue motion than either power Doppler or image-subtraction methods.

Although not shown here, we were able to generate overlays of contrast data over the b-mode tissue by utilizing a relay circuit to toggle excitation of the low-frequency and high-frequency elements with successive imaging frames, and then displaying successive tissue and contrast frames together by color coding the contrast data.

Based on the results of the *in vitro* radiation force experiments, the dual-frequency probe could be utilized to direct microbubbles to the endothelial wall in targeted imaging studies over a range of physiologically relevant flow velocities. Additionally this ability could be implemented in acoustically-mediated drug delivery studies, because the probe is also capable of delivering acoustic energy above the bubble destruction threshold, which would facilitate site-specific release of therapeutic agents.

Although the studies within this section were performed in rats, its resolution as well as its sensitivity makes its implementation in mice studies also highly attractive. However, the high-frequency components come at the cost of a loss in penetration depth (less than  $\sim 2$  cm), and thus our specific parameters are less suitable for clinical application and more appropriate for translational research with small animal models. The combination of high contrast-to-tissue ratios and high spatial resolution achievable with our prototype probe make novel approaches to understanding and quantifying specific morphologies of pathologic vasculature an exciting possibility. For an additional perspective on our imaging strategy's ability to visualize microvessels *in vivo*, the reader is referred to a supplemental video in which a volumetric rendering of the vasculature within a subcutaneous rat fibrosarcoma tumor model is displayed.

### 3.1.4 Conclusion

We have demonstrated that acoustic angiography imaging can be utilized *in vivo* at higher frequencies than previously demonstrated to produce high-resolution images with high contrast-to-tissue ratios. Because of the substantial tissue suppression, this technique is robust in the presence of tissue motion. Additionally, the probe effectively produced radiation force *in vitro* on microbubbles with flow-rate parameters analogous to most types of environments found within a wide range of vasculature types.

### 3.2 High resolution assessment of vessel architecture - *ex vivo* tissue samples

Liver transplantation is the gold standard for end-stage liver disease. Currently, more than 16,000 adults and children are in need of liver transplants, but unfortunately the amount of livers available for transplantation is in short supply [89]. Therefore, alternatives, such as bioartificial organs, are being explored. Clinically relevant bioartificial livers typically use hepatocytes from xenografts, seeded in a semi-permeable membrane and based on hemodialysis of the patient's blood [90]. Unfortunately, these bioartificial livers only provide temporary relief until a transplantable organ is available. In order to provide a true replacement for live donor transplantations, a more sophisticated artificial organ is needed. The desire to produce an artificial liver to replace the dependency on living donors has led to a push to develop decellularized liver organs that, after recellularization, would house patient-specific human hepatic cells. The method of decellularization converts an *ex vivo* or cadaveric liver organ to an acellular, three-dimensional structure of naturally occurring scaffold materials. These scaffolds would then be reseeded with a patient's own cells and, in theory, would act as a functional liver. The new organoid would provide the same, albeit improved, metabolic operations as their original liver, theoretically without the need for the heavy

immunosuppressant treatments associated with liver transplants. Thus, it is these extracellular matrix scaffolds prepared from decellularized tissues that are the hope for stable organoids. Ongoing efforts are focused on establishing human liver organoids by seeding liver biomatrix scaffolds with stem cells, hHpSCs<sup>10</sup> or biliary tree stem cells<sup>11</sup>, and with their mesenchymal cell partners (angioblasts and precursors to endothelia and hepatic stellate cells)[91].

Protocols to decellularize organs vary among labs, and thus the resulting scaffolds contain varying amounts of matrix molecules. The matrix molecules that are retained after decellularization are important for cell engraftment, mitosis and differentiation [92]. Some labs have been able to achieve cellular engraftment in the decellularized scaffolds, though the reported functional data - such as albumin and urea secretion - from reseeded cells has been lower relative to healthy hepatic output. For reseeded scaffolds to provide either an adequate organ transplantation alternative, or *in vivo* model for drug discovery, cell function must meet that of normal human livers. It is thus one of the common objectives in tissue engineering to optimize scaffold reseeding protocols, thereby maximizing the structural integrity and functionality of the organoids. Since cell seeding and organoid functionality are directly related to the patency and structure of the microvascular scaffold, there is a crucial need to non-destructively assess the structural characteristics of the scaffold vascular matrix. Without adequate perfusion, the reseeding process of biomatrix scaffolds with new cells cannot be accomplished, as this process relies on fluid transport through the matrix remnants of the vascular bed for the delivery of the cells. Also, after cells have been engrafted throughout the 3D volume of tissue, their continued function depends on a long-term delivery of nutrients and oxygen. In the past, perfusion in biomatrix scaffolds have been assessed in different ways, but it generally was achieved by qualitatively examining the color of the tissue sample, with regions of discoloration in the sample indicating a lack of adequate

internal flow. This approach can be useful for identifying insufficient flow within large regions in the sample, such as throughout an entire lobe, but it is insensitive in detecting subtle variations in volumetric perfusion over time. Thus a method to image both the anatomy and flow within the sample is highly desirable. Hence, in these studies, we have developed a protocol to enable rapid yet detailed assessment of vascular structural and functional characteristics within liver biomatrix tissue scaffolds.

### **Imaging methods for assessing tissue engineering scaffolds**

There are many methods used to image tissue scaffolds, including scanning and transmission electron microscopy (SEM and TEM) and optical microscopy[93], magnetic resonance (MR) imaging and microscopy [94], computed tomography (CT) [95], optical coherence tomography (OCT) [96], and Doppler ultrasound[97]. The selection of any one modality will always yield inherent tradeoffs, such as cost, invasiveness to the sample, field of view, resolution, acquisition time, and type of information gleaned. For an extensive assessment of the tradeoffs, the reader is referred to a review by Mather [98]. The only imaging modalities in the above list which can holistically (i.e. image a sample in its entirety) and non-invasively image a rodent tissue biomatrix scaffold sample in its entirety are MR, CT, and ultrasound. MR and CT are widely available in both clinical and research contexts, though require expensive hardware, are not real time, require long image acquisition times (MR), can cause radiation damage to cells (CT), and suffer from poor soft tissue contrast (CT). Ultrasound, on the other hand is real-time, relatively inexpensive, non-invasive, does not use ionizing radiation, and has excellent soft-tissue contrast. In addition to these, ultrasound is able to assess multiple different facets of a tissue volume (applicable to both *in vivo* volumes and *in vitro* biomatrix scaffolds), including tissue structure with standard b-mode[99], mechanical stiffness[100], microvascular perfusion architecture[101], parametric perfusion

speed[31]. One possible challenge hindering ultrasound’s utility for scaffold perfusion assessment has likely been the modality’s limited field of view, allowing for freehand visualization of different 2D slices, or small 3D sub-volumes, but never holistic visualization or quantitation. Our objective in this study was to design a tissue preparation, restraint, and imaging protocol to enable the 3D visualization and quantification of perfusion throughout a biomatrix scaffold.

### **Contrast ultrasound imaging**

In addition to traditional grayscale ultrasound to provide reference images of the scaffold physical structure, two different contrast enhanced ultrasound techniques were utilized in this work to provide functional information about biomatrix scaffold microvasculature. The first technique, referred to as “flash replenishment” (sometimes called “destruction reperfusion”), allows relative blood flow rates to be spatially mapped by assessing the speed at which contrast agents refill a sample volume after clearance[25]. While this technique is not new, it has not previously been performed in this type of *ex vivo* scaffold imaging application. The other contrast imaging approach implemented in this study is new technique we refer to as acoustic angiography. Acoustic angiography is a newly developed imaging method differing from traditional ultrasound imaging in that it is designed only to visualize vascular and microvascular structure, rather than tissue anatomy [66; 102]. Unlike, flash replenishment, acoustic angiography does not yet have the ability to parametrically map perfusion rates, however, it can provide detailed visualization of vessel architecture, and provided a high resolution dataset from which vessels can be segmented and quantitatively mapped (vessel network volume, length, etc.). Thus, our protocol involves three imaging scans, first defining the biomatrix scaffold physical structure (anatomy), mapping vessel architecture with high resolution acoustic angiography for vascular network visualization and

quantitation, and then mapping perfusion rates with flash replenishment. Note that all three studies could be performed sequentially with appropriate system hardware.

### **3.2.1 Materials and methods:**

The scaffold preparation procedure is provided in Appendix C.

#### **Sample imaging chamber**

The sample imaging chamber was designed to allow a tissue sample to be imaged while submerged under a fluid. This allows for non-contact image acquisition - as opposed to gel-based coupling, which is typical for ultrasound imaging exams - and thus no tissue warping was caused during imaging, resulting in better registrations of multiple sub-volumes of image data. The imaging chamber designed for this purpose was composed of two concentric 0.25 inch thick acrylic cylinders (Figure 3.12, A+B) each 3 inches tall. The outer diameters of the outer and inner cylinders were 6 and 5 inches, respectively. This outer cylinder was mounted to the 6x6x0.3 inch acrylic base of the imaging chamber via acrylic glue. The inner cylinder was fit to the imaging chamber's base over a Vaseline-lubricated silicone O-ring allowing for quick coupling with a tight seal. Though not implemented in this study, this O-ring design also enabled bidirectional imaging orientations (i.e. it was possible to rotate the inner chamber and image the contralateral side of the tissue sample). The interior cylinder served several purposes. It provided a frame for the tissue sample support webbing, made of 5-0 silk suture (Ethicon - Somerville, New Jersey). This support webbing held the sample suspended in the interior of chamber. Additional suture was loosely tethered over the top of the tissue to prevent flotation or shifting during the imaging study. The interior cylinder of the sample imaging chamber also acted as a buffer for the circulating bubble clearance fluid circuit (described later in this section), as the larger holes in it allowed for efficient fluid transfer but also limited turbulence near the sample.

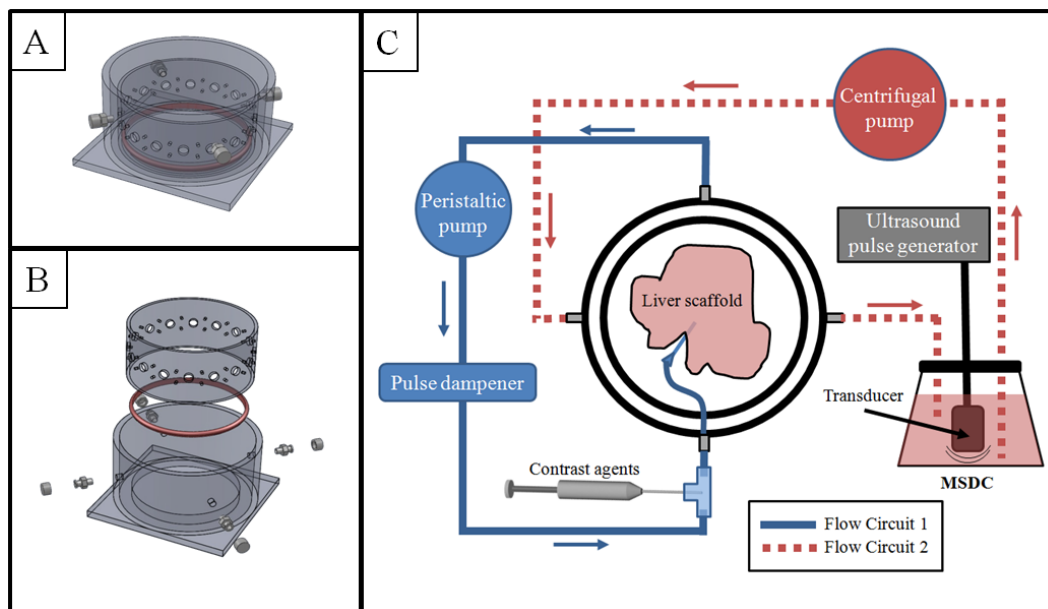


Figure 3.12: Schematics for the sample imaging chamber. A) Assembled sample imaging chamber and B) exploded view of the sample imaging chamber. C) A top-down cartoon schematic illustrating the two flow circuits in the setup. Flow Circuit 1 provided perfusion and microbubbles to the liver scaffold, while Flow Circuit 2 provided continuous circulation through the microbubble sequestration and destruction chamber (MSDC) to remove contrast excreted from the sample.

Preliminary studies showed that the peristaltic pump, which powered flow circuit #1 (Figure 3.12C), caused a slight periodicity in the flow rate through the scaffold samples as a result of the pump's rotary wheel design. The frequency of this periodicity would scale with the speed of the peristaltic pump. This would result in beat frequencies between this pump frequency and the frame rate of our imaging systems, which manifested as large cyclic variations in contrast intensity between adjacent imaging planes. To prevent this artifact, a pulse dampener (Model 07596-20 - Cole Parmer, Vernon Hills, IL) was placed between the output from the peristaltic pump and in the input to the sample. Preliminary studies also showed that microbubbles exiting the sample into the surrounding fluid after perfusing through the portal circuit resulted in a decrease in image quality over time. These freely flowing microbubbles in the fluid surrounding the biomatrix scaffold caused excessive attenuation of imaging signal. To



prevent this, a bubble clearance fluid circuit was implemented (Flow circuit 2 in Figure 3.12C). This circulated the fluid surrounding the scaffold sample through a microbubble sequestration and destruction chamber (MSDC) before reinjection back into the imaging chamber. The MSDC was a 2 L Erlenmeyer flask in which was suspended a 1 MHz unfocused piston transducer (Valpey-Fisher - Hopkinton, MA) designed to facilitate contrast destruction. The 1 MHz piston transducer was pulsed at 10 Hz with a pressure of 460 kPa via a pulser (Model 801A, Ritec - Warwick RI). Media surrounding the biomatrix scaffold was continually pumped through this chamber at 1 mL/min via a centrifugal pump (model PQ-12, Greylor - Cape Coral, FL) powered by an external DC power supply (model DIGI360, Electro Industries - Westbury, NY). Four nylon luer fittings were attached to the outer cylinder for coupling the sample imaging chamber to the two flow circuits. All fluid circuits used 0.125 inch inner diameter Tygon tubing, except between the catheter entering the scaffold sample and the outer cylinder of the imaging chamber: this was 0.062 inch diameter tubing.

### **Contrast imaging**

Flash replenishment imaging was performed using an Acuson Sequoia 512 equipped with a 15L8 transducer (Siemens Medical Solutions USA Inc, Mountain View, CA). The “CPS Capture” software algorithm was used to measure perfusion time. 3D images of the liver scaffold were acquired by scanning the transducer in the elevational direction using a linear stage and motion controller (UTS150PP and ESP300, Newport, Irvine, CA) interfaced through LabVIEW (National Instruments, Austin, TX) as described in [31]. Perfusion images were parametrically mapped to contrast arrival times between 1 and 10 seconds. These images were stored in DICOM format with JPEG compression and analyzed offline in Matlab (Mathworks - Natick, MA). Perfusion times within the regions of interest were assessed.

Acoustic angiography was performed on the second generation dual-frequency probe described in Chapter 3.1 with imaging parameters previously described [101]. Briefly, the imaging system was a VisualSonics Vevo770 (Toronto, ON, Canada) pulses were emitted at 4 MHz at 1.23 MPa, and echoes were received on a 30 MHz transducer with 100% bandwidth after being passed through a 15 MHz high pass filter to remove non-contrast signal. 3D images were acquired with the VisualSonics 1D motion stage with inter-frame distance of 100  $\mu\text{m}$  to yield nearly isotropic voxels. Images were acquired with a frame rate of 2 Hz, with 5 frames averaged at each location. High resolution b-mode images were also acquired on the Vevo770 system with the same imaging parameters, except the transmit frequency changed to 30 MHz. After imaging, data was exported from the ultrasound system as 8 bit uncompressed AVIs.

The microbubbles used in this study were prepared with the Perfusion Agent formulation as described in Appendix A. Microbubbles were introduced to the perfusion fluid circuit through a T-valve injection port located between the pulse dampener and the biomatrix. A 24 gauge needle was used to pierce the septum, and microbubbles could then be injected into the fluid circuit via a computer controlled syringe pump (Harvard Apparatus - Holliston, MA). Microbubbles were administered into the fluid circuit at a rate of 20  $\mu\text{L min}^{-1}$  and concentration of  $1.5 \times 10^9 \text{ mL}^{-1}$  out of a 1 cc syringe.

Three different livers scaffolds were imaged for this study, hereafter referred to as samples numbered 1 through 3. The left lateral lobe (LLL) of each liver scaffold was selected as the lobe of interest for this study because it is easily accessed for imaging. Another advantage of this lobe was its narrow morphology - the Vevo770 has a fixed acoustic focus, and thus has a narrow depth of field ( $< 1 \text{ cm}$ ). Our goal was to provide a holistic assessment of perfusion throughout a volume of tissue, and thus the left lateral lobe was most amenable to this objective. That said, the techniques presented herein could be extended to the entire volume of tissue if one had a transducer with a larger

axial field of view. Each liver biomatrix scaffold was imaged with two imaging modes: flash replenishment, and acoustic angiography.

### **Validating imaging consistency**

Microbubble buoyancy and floatation within syringes is known to cause a reduced concentration output from a syringe over time [103]. It was hypothesized that the change in microbubble concentration input to the tissue sample would cause different perfusion values reported for the same location in tissue, as this has been observed for *in vivo* kidney studies [31]. To mitigate this effect the syringe was gently agitated throughout the imaging procedure as described previously [103]. To characterize the degree to which this affected the consistency in the reported perfusion data extracted from the image data, a study was performed in which the transducer was fixed at a single location and flash replenishment images acquired approximately every minute for 30 minutes. The data was exported to Matlab for analysis. A region of interest (ROI) was defined around the perimeter of the lobe being imaged. Two quantities were assessed at each timepoint within the ROI: the total number of perfused pixels, and the average perfusion value. If the output microbubble concentration into the scaffold perfusion circuit was dynamically changing, it would be expected that both of these quantities would also change. If a perfectly stable concentration of bubbles was maintained, then neither quantity would change. Two scaffolds were used for this study; the first was imaged with the non-agitating protocol susceptible to microbubble floatation. After data was analyzed offline, a second liver scaffold was imaged to observe the effects of syringe agitation on perfusion assessment consistency.

## Registration of sub-volumes

Because the lateral field of view of the ultrasound transducers used for these imaging studies was insufficient to capture the entirety of the liver lobe of interest, multiple “sub-volumes” were acquired on each system and later registered together offline. Throughout this manuscript, sub-volume is used to describe a 3D volumetric image that does not holistically capture a tissue of interest. Registration of these sub-volumes was performed within the open source 3D Slicer environment (ver 4.2.1, National Alliance for Medical Image Computing - [www.slicer.org](http://www.slicer.org)) using the Merge module, part of the TubeTK extension. This module is designed to register together two images that have a small degree of overlap along one of the axes. When the sub-volumes were registered together using the Merge module, they would form a single cohesive volume for the liver lobe of interest for each image type (b-mode, flash replenishment, and acoustic angiography). The transforms module was used to then register the three types of ultrasound image data to each other, creating a single composite 3D image for each of the livers imaged.

## Assessing liver biomatrix perfusion

The two perfusion imaging modes implemented in this study (acoustic angiography and flash replenishment) were acquired on different ultrasound systems, thus an initial registration step was necessary prior to the merged volumetric datasets being in the same coordinate system. This registration step was performed via a rigid transform within the Slicer Transforms module. The lobe of interest could then be manually segmented and the same ROI used for all three datasets. The manual segmentation of the LLL was performed in Matlab using the function *roipoly.m*. Because the segmentation and registration process was performed entirely offline, it was impossible to re-collect the ultrasound data of a scaffold if it became clear that small portions of the tissue were

not imaged. In these cases, ROIs were defined to the edge of the available image data, or across regions of tissue if it was obvious to the viewer what path the tissue boundary was taking.

Each voxel within the flash replenishment images represented a spatially localized estimate of perfusion speed. To assess perfusion throughout the volume of tissue, all values were vectorized and histograms were created for each sample. These perfusion histograms were binned by perfusion time, and area normalized by total perfused voxels (i.e. the integral of the histogram was set to unity). To segment the vessels out of the acoustic angiography datasets, a previously described segmentation algorithm was used [51]. These segmentations were used to compute total length and volume of the vessel network, vascularity ratio (volume of vessel network/volume of liver lobe). The volume of each discretized location in the segmented vessel network was computed and summed to yield total vessel network volume and length. The proportion of the vessel network occupied by vessel segments of a range of radii between 50  $\mu\text{m}$  (minimum voxel size) and 500  $\mu\text{m}$  was computed.

### **3.2.2 Results**

#### **Validation of imaging consistency**

An improvement in imaging consistency was observed as a result of the rotation of syringe during the infusion of microbubble contrast. The percent deviation ( $\% \sigma = \sigma / \mu$ ) in the normalized perfused area (NPA) within the 2D region of interest was reduced from 13.3% to 6.3%, and the percent deviation in the normalized perfusion speed (NPS) was reduced from 15.1% to 6.6%. The NPA and NPS values are normalized to the starting value at the beginning of the 30 minute acquisition. Additionally, there was a 10-fold reduction in slope magnitude for the linear fit in the NPS measurements after changing the protocol (Figure 3.14 B and D), changing from -0.0081 to 0.0008, indicating a

more consistent measurement for perfusion speed over time. The change in slope for the NPA was less dramatic, changing from 0.0006 to -0.0035 (Figure 3.14 A and C), corresponding to a 0.2 fold change, suggesting that the same number of pixels were, in general, perfusing throughout the data acquisition period for both the syringe rotation and non-syringe rotation protocols.

### **Liver biomatrix lobe imaging, segmentation, and perfusion assessment**

All three scaffold samples imaged required the registration of multiple sub-volumes for holistic visualization. Perfusion rate information required two sub-volumes for all samples, while the anatomical information and acoustic angiography data required three sub-volumes for sample #1 and two for samples #2 and #3. Once completed, the acoustic angiography data was displayed via maximum intensity projections (MIPs) (Figure 3.15). Anatomical b-mode data cannot be displayed in this fashion, so XZ slices through the merged volumes were displayed. The reperfusion rate data were displayed both as 2D slices through the volume.

Sample #1 was noticeably different than samples #2 and #3, from a qualitative standpoint in both the acoustic angiography and perfusion images. There were fewer smaller vessels visible within perfusion data. This was due to an experimental error during setup of the sample the biomatrix scaffold's surface was pierced during its placement in the sample imaging chamber. The result was several low resistance outlets for contrast exiting the system. One large perforated outlet was clearly visible within the acoustic angiography image set (Figure 3.15, Sample #1, yellow arrow).

Another insight gleaned from the visualization of the scaffold samples (Figure 3.15) was the ability to delineate vessels as part of either the hepatic or portal circulatory networks within the tissue volume (white vs. black arrows, respectively). Because

contrast was infused through the portal vein, the hepatic circuit did not contain microbubble contrast and thus was not visualized under acoustic angiography. When the b-mode volumes were registered to the acoustic angiography volumes, flow voids in the b-mode, which were not perfused within the acoustic angiography dataset, could be classified as components of the hepatic circuit.

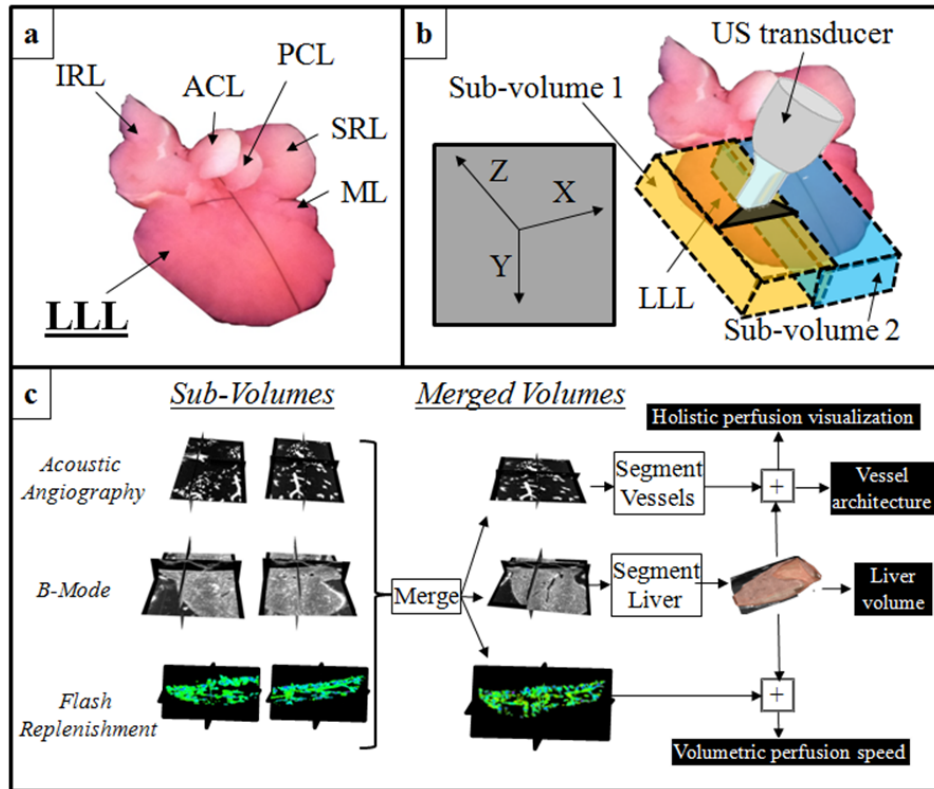


Figure 3.13: A: The orientation of the biomatrix scaffold sample as viewed from above with the following visible lobes labeled: left lateral lobe (LLL), inferior right lobe (IRL), anterior caudate lobe (ACL), posterior caudate lobe (PCL), superior right lobe (SRL), and median lobe (ML). The LLL was the lobe we imaged in this study. Lobes were identified in this figure via an available surgical guide [104]. B: Orientation of the imaging sub-volumes relative to the tissue sample. XY dimensions were lateral and axial axes within the ultrasound coordinate space, with the Z axis being the elevational scan direction. C: Schematic explaining the registration of multiple 3D volumes from three distinct ultrasound imaging approaches into the final composite volume, and what quantities could be extracted



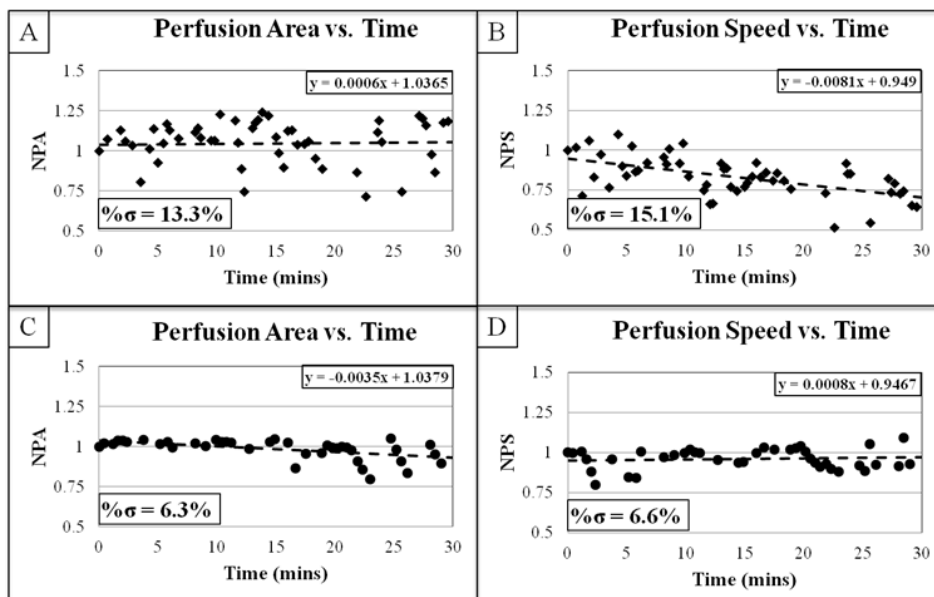


Figure 3.14: Data illustrating the stability of the normalized perfusion area (NPA) and normalized perfusion speed (NPS) before and after modifying the contrast injection protocol. A+B represent data before syringe mixing, while C+D show after syringe mixing. Note the improvement in consistency (i.e. the reduction in percent standard deviation) for both parameters after implementing syringe mixing.

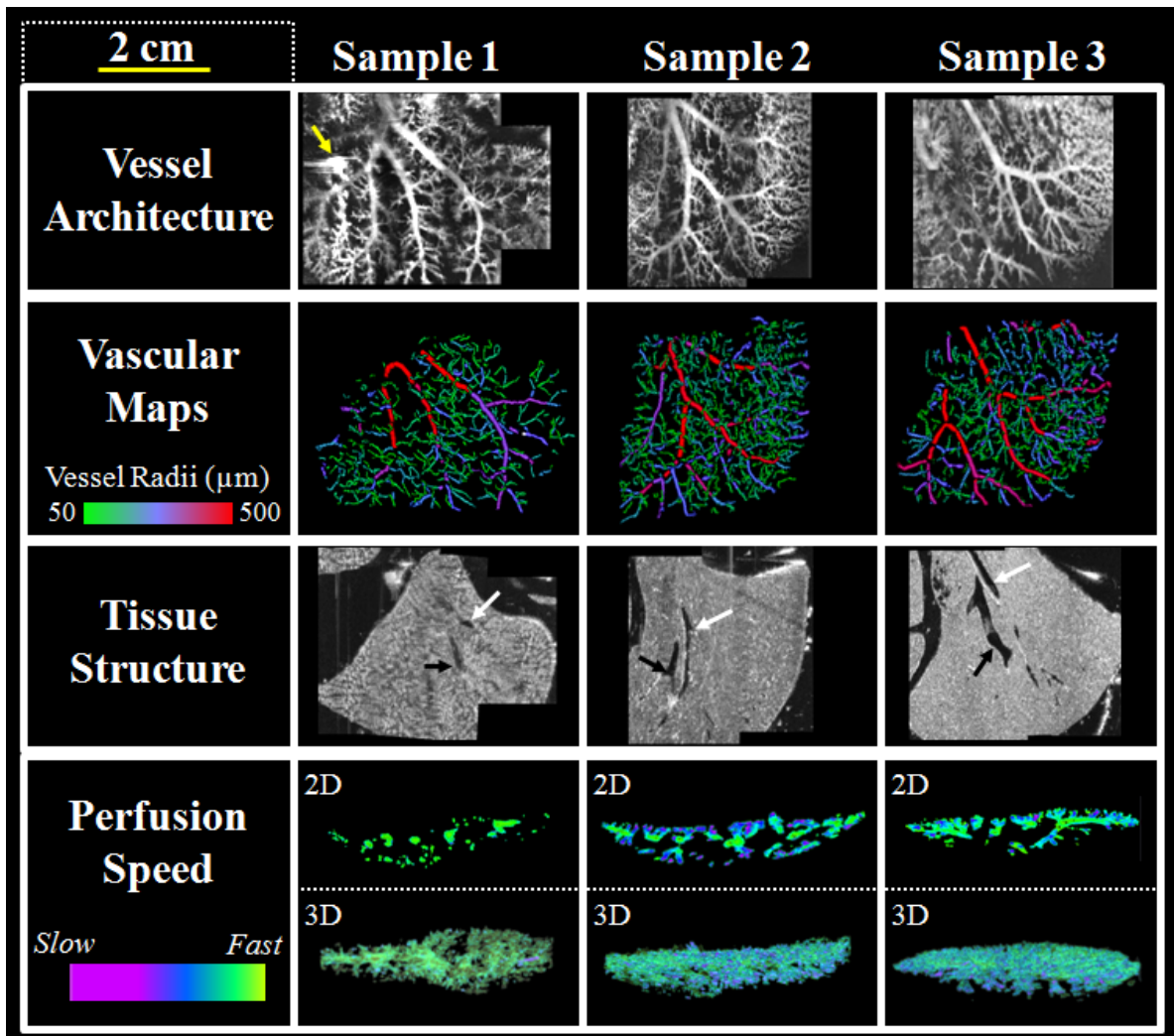


Figure 3.15: A compilation of all image data acquired of the three biomatrix scaffold samples. Yellow arrow indicates location of sample #1 which were perforated, and thus leaking microbubbles. Each row was acquired with the following imaging modes (from top to bottom): Acoustic angiography, vascular segmentations, b-mode, manually defined regions of interest, and flash replenishment. White and black arrows on the b-mode images indicate vessels identified as part of either the portal or hepatic circuits, respectively. In the flash replenishment images, the top images are 2D XY slices, and the bottom are Z-projection renderings. The flow rate colorbar indicates pixels mapped to between 10 and 1 second reperfusion times for slow to fast flow, respectively.

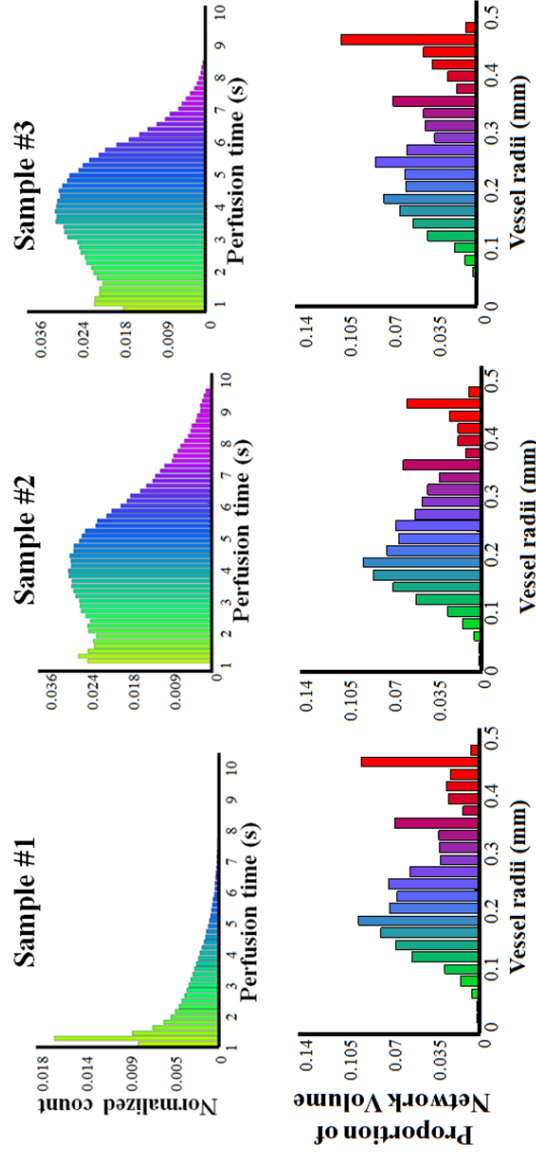


Figure 3.16: Perfusion comparisons between liver scaffolds. (Top) Area normalized perfusion speed histograms from merged 3D flash replenishment volumes. The colors of the histogram bins in B-D correspond to the colormap for perfusion in Figure 4. (Bottom) Area normalized vessel size histograms computed from the vessel segmentations. The colors of each bin correspond to the colors of vessel radii within Figure 3.15.

Vessel network architecture was assessed via over 1,700 vessel segmentations (Figure 3.15) extracted from the acoustic angiography image data (image data from which these were extracted in Figure 3.17). These data were rendered in 3D and color coded by whether vessels are inside or outside the manually defined tissue boundary. Different numbers of vessels were extracted from each sample: for sample #1 (N = 415 vessel segmentations), sample #2 (N = 702 vessel segmentations), and sample #3 (N = 671 vessel segmentations). The volumes and total length of these vessel network segmentations were computed to be 142.6, 226.6, and 241.3  $\mu\text{L}$  and 1.0245, 16177, and 1.4646 m for samples #1, #2, and #3 respectively. The vascularity ratios were 1.97%, 3.82%, and 3.10% for samples #1, #2, and #3 respectively (Figure 3.17D). While these metrics each reveal sample #1 to be contain fewer perfused vessels (both in total volume of the vessel network, and as a proportion of total volume of the biomatrix tissue) the distribution of vessel sizes were similar between all three of the samples (Figure 3.16, bottom).

### **3.2.3 Discussion and concluding remarks**

Biomatrix scaffolds are complex, 3D tissue extracts of extracellular matrix that can be used as substrata for establishment of organoids. They are chemically and functionally tissue-specific but not species-specific. Thus scaffolds prepared from rat and murine tissues can be used to establish human organoids. Their potential for tissue engineering is implicated by the findings that they can be isolated rapidly (in a few hours), contain essentially all of the collagens (>98%) and all known collagen-bound matrix and matrix-bound growth factors/cytokines and with localization of the components to relevant histological sites. Prior reports demonstrated that frozen sections or pulverized forms of biomatrix scaffolds can be used as substrata for cells; they enable cell attachment within seconds to minutes; maintain adult rodent and human cells in a fully

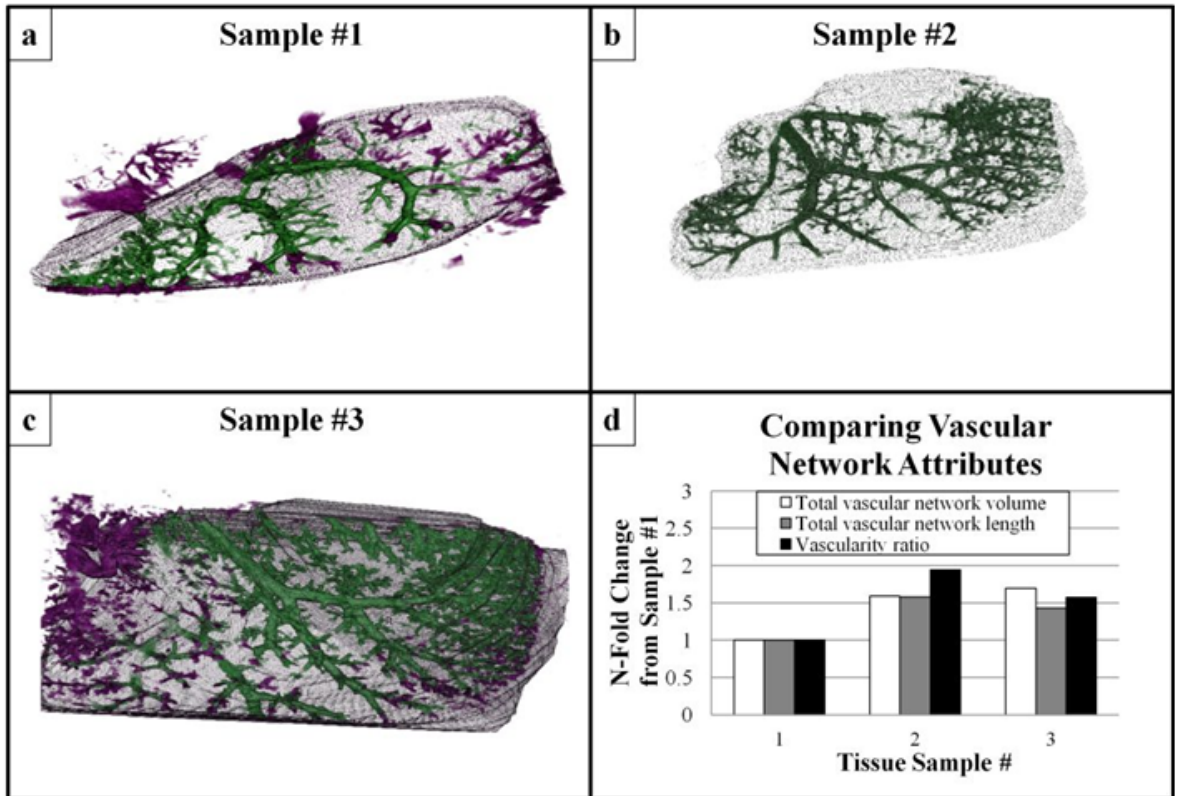


Figure 3.17: 3D renderings of the biomatrix acoustic angiography data (A-C). Color is defined as either inside (green) or outside (blue) of the manually defined tissue border. D: quantitative assessments of vascular network volume, length, and vascularity ratio. Data are normalized to sample #1.

differentiated state for more than 8 weeks; and induce lineage restriction of stem cells to mature cells in approximately a week after which they remain stably differentiated for months[105]. The ultrasound images provide novel insights into the complexity of the matrix remnants of the liver architecture and of the vascular channels. The dimensions of the channels can be quantified precisely using these ultrasound technologies and corresponding segmentation algorithms, allowing one to identify categories of blood vessels for which such dimensions are known. Important experimental logistics. During the development of this acoustic imaging protocol for assessing liver biomatrix scaffold perfusion, several experimental techniques were discovered to be of significant importance for effective experimental outcomes. The first was the importance of maintaining a consistent microbubble concentration input to the scaffold, suggested by [31], and evaluated via the longitudinal consistency analysis (Figure 3.14). Agitating the microbubble-containing syringe during infusion doubled the reported perfusion consistency values, and reduced the variability in the reported perfusion speeds to below 10%. The minimization of contrast administration-induced variability in perfusion assessments is critical for accurate inter-sample comparisons. The second experimental technique found to result in significant variability in reported perfusion was the care with which the samples were handled prior to imaging. While it may seem self evident that biomatrix scaffolds ought to be handled with care, we would not have known we had compromised sample #1 without examining the image data.

The plume of contrast visibly exiting the scaffold boundary, and the vast differences in reported perfusion between sample #1 (perforated surface) and samples #2 and #3 (both undamaged) (Figures 3.15, 3.16, and 3.17) highlight the importance of being mindful of biomatrix scaffold fragility during decellularization and imaging setup procedures. The observation that dramatic differences in image quality and reported

perfusion rate distributions result from damaged samples also suggest that these imaging methods could be used as screening methods to assess the integrity of a biomatrix scaffold, and thus reducing waste. An imaging study after decellularizing sample #1, for example, would have revealed that efforts to reseed cells within the scaffold would surely have failed, thereby saving time and reagents. Offline data analysis. During the offline registration and segmentation processing steps, it was discovered that some portions of the LLL were excluded from analysis. This was due to the transducers form factors being too large to image the portions of the scaffold tissue close to the sample imaging chamber's wall (b-mode images for samples #1 and #2 in Figure 3.15 illustrate this). We estimate this lack of image data to result in relatively minor errors in ROI definition, and thus relatively small errors in the estimates for perfusion (since the periphery of the LLL would be most affected by this). Thus, since the periphery of the liver's lobes are predominantly occupied by slowly perfusing vasculature[104], the mean perfusion values reported via these manual segmentations will not be affected by the exclusion or inclusion of a small proportion of this region of tissue. Nonetheless, these errors are preventable, and can be avoided by placing the sample with the lobe of interest as close to the center of the sample imaging chamber as possible, thereby preventing contact between the transducer face and inner cylinder wall. Alternatively, a sample imaging chamber with a larger interior diameter could be selected as a way to circumvent this, but care must be taken when increasing the size of the chamber; volume of a cylinder increases proportionally to the radius cubed. A sample imaging chamber with a significantly larger volume would require a much faster flow rate through the microbubble sequestration and destruction chamber (MSDC in Figure 3.12) to prevent contrast accumulation. Though not explicitly implemented in this study, it was discovered during the registration and display of the merged volumetric b-mode and acoustic angiography data (Figure 3.15) that the hepatic and portal circuits could be delineated

by comparing speckle voids in the b-mode data to acoustic angiography data contrast enhancement regions of overlap are the portal circuit (since this was the circuit perfused by microbubbles) and those without mutual overlap are the hepatic circuit. Alternatively, we could have infused contrast into the hepatic circuit to elucidate that vascular network instead.

### **Significance of these novel ultrasound imaging methods**

Evaluation of biomatrix scaffolds (or any form of decellularized tissue scaffold) prior to use for recellularization and during the recellularization process can be achieved with the protocol contained herein for perfusion assessment of scaffolds via multiple ultrasound imaging modes. The method necessitates a sample imaging chamber to hold and restrain the *ex vivo* sample, a systematic method for acquiring overlapping sub-volumes, a registration method for merging the sub-volumes into cohesive 3D images of the entire volume. The form factor of the sample imaging chamber designed for these studies allows for contact-free imaging, mitigating the tissue warping effects of imaging studies implementing coupling gel, and therefore registrations between the sub-volumes were straight forward. All the image visualization and most of the image analysis can be performed in freely available open source software. The ultrasound approaches described herein offer a real time and inexpensive technique (relative to CT, and MR) for visualization of biomatrix scaffold perfusion, with anatomical images acquired with the same probes as vascular perfusion data acquisition. Additionally, these approaches offer a better depth of penetration into the scaffold than optical imaging approaches, allowing for the visualization of the entirety of the LLL (at the expense of both axial and lateral resolution, which is worse than systems imaging at optical wavelengths). Finally, the method was non-destructive to the sample, unlike microscopy-based methods of scaffold assessment.



While advantages to the protocol presented in this manuscript are numerous, there are also several drawbacks worth mentioning. Currently, there are no ultrasound transducers capable of acquiring both types of contrast imaging approaches implemented in this study: high resolution acoustic angiography and dynamic perfusion speed mapping. In addition to multiple image acquisitions requiring more time to collect the data, this also necessitates the experimentally cumbersome maneuver of transferring the sample imaging chamber between systems. Also, while several groups have made strides toward calibrating flash replenishment imaging against absolute values for perfusion rate calibrated against gold standards[25; 106] the technique currently only provides relatively quantitative measures for perfusion. This is adequate for assessing differences in regions within a given sample, such as would be necessary for identifying pockets of occlusion, it does not yet allow one to determine absolute flow rates ( $\text{mL s}^{-1}\text{cm}^{-3}$ ) within the biomatrix scaffold.

Nondestructive 3D perfusion imaging of decellularized organs and tissues could have significant value in the field of tissue engineering. To date, recellularization of entire liver biomatrix scaffolds after imaging the vasculature has not been demonstrated but is currently the focus on ongoing studies. Future studies could include the correlation of structural information, such as vessel diameters, perfusion rates, and patency with the gold standard of histological data after reseeding and recellularization procedures are complete. Additionally, these structural details could later be correlated to regions of cell attachment and cell differentiation to help identify and tune optimal cell seeding perfusion rates and incubation times. Finally, ligand-bearing microbubbles could be implemented in a 3D ultrasonic molecular imaging study to spatially map specific regions and types of adherent cells within the scaffold.

### **3.3 Acoustic angiography for assessing microvasculature structure: pilot *in vivo* studies**

In this section the technique of high-resolution microvascular imaging using a prototype dual-frequency transducer is examined in greater detail. This transducer enables vascular imaging with both extremely high contrast sensitivity and imaging resolution. With this technology, the traditional resolution vs. contrast-sensitivity tradeoff can be partially circumvented by detecting of the high-frequency components from the wideband acoustic energy produced by microbubbles excited at low frequencies near their resonance, as reported initially by [66]. A more detailed discussion of the transducer design, resolution, and contrast-to-noise performance has been presented earlier in this chapter (Chapter 3.1). The resulting ultrasound images illustrate high-resolution depictions of the microvasculature, without background from surrounding tissue, not unlike x-ray angiography images. Furthermore, through use of traditional single-frequency pulse-echo, a tissue b-mode image can be acquired for anatomical reference. Thus, we refer to images acquired with this technology as “acoustic angiography.” In this collection of pilot studies, we present examples of high resolution *in vivo* 3D images acquired with our prototype transducer which display both healthy and diseased vascular networks. For qualitative comparison, we also provide contrast enhanced CT and photoacoustic images, and we compare and contrast acoustic angiography with these other imaging techniques.

#### **3.3.1 Animal imaging**

All animal studies were approved by the UNC Chapel Hill Institutional Animal Care and Use Committee. All imaging studies were performed in rats. Seven animals were imaged for this study: three healthy controls were imaged in their flank region, three animals with a tumor model contained within the same type of tissue were imaged, and

one animal was imaged for a healthy kidney for comparison to contrast enhanced CT imaging. The tumor model (fibrosarcoma) was initiated by propagating tumor tissue through subcutaneous implant in the rodent flank. Initial tumor samples were provided by the Dewhirst lab at Duke University. The nonlinear ultra-broadband ultrasound imaging strategy necessitates the use of contrast agents to provide signal from the vasculature. In these studies, microbubble contrast agent with a polydisperse diameter distribution centered at  $0.9 \mu\text{m}$  with a standard deviation of  $0.45 \mu\text{m}$  were prepared with the perfusion formulation. Microbubble contrast was diluted in saline and administered via a tail vein catheter with a syringe pump at  $70 \mu\text{L}/\text{min}$  at a concentration of  $3.3 \times 10^9$  bubbles/mL. Imaging pulses were 4 MHz single cycle sinusoids with a peak negative pressure of 1.23 MPa ( $\text{MI} = 0.62$ ). 3D ultrasound images were acquired with interplane step sizes of 150-200  $\mu\text{m}$ , and required fewer than 3 minutes to acquire. Since the tissues of interest were in the lower abdomen and flank, respiratory motion artifacts were limited. All ultrasound images were acquired coplanar with the axial anatomical plane with animals in dorsal recumbency.

The CT images were acquired of the rat kidney 45 minutes after the injection of contrast. The contrast agent implemented was Fenestra VC (Advanced Research Technologies, Montreal, QC), an iodinated lipid blood pool CT contrast agent injected at a concentration of 3 mL/450 g tissue. CT images were acquired using the GE eXplore SpeCZT CT 120 SPECT/CT (GE Healthcare - London, ON) at 90 kVp using 900 views over 360 degrees with total output 576 mAs. The total dose delivered was 300 mGy. Reconstruction was performed on 100  $\mu\text{m}$  isotropic grid with a standard FDK algorithm.

### 3.3.2 Results

#### Tumor imaging

One likely application of acoustic angiography will be the visualization of tumor microvascular structure. Figure 3.18A illustrates the ability of the probe to acquire both vascular images and tissue images of the same *in vivo* sample volume. Vessels imaged in acoustic angiography mode are overlaid on a traditional high-frequency b-mode image, thereby enabling the visualization and spatial characterization of vessel-tissue integration.

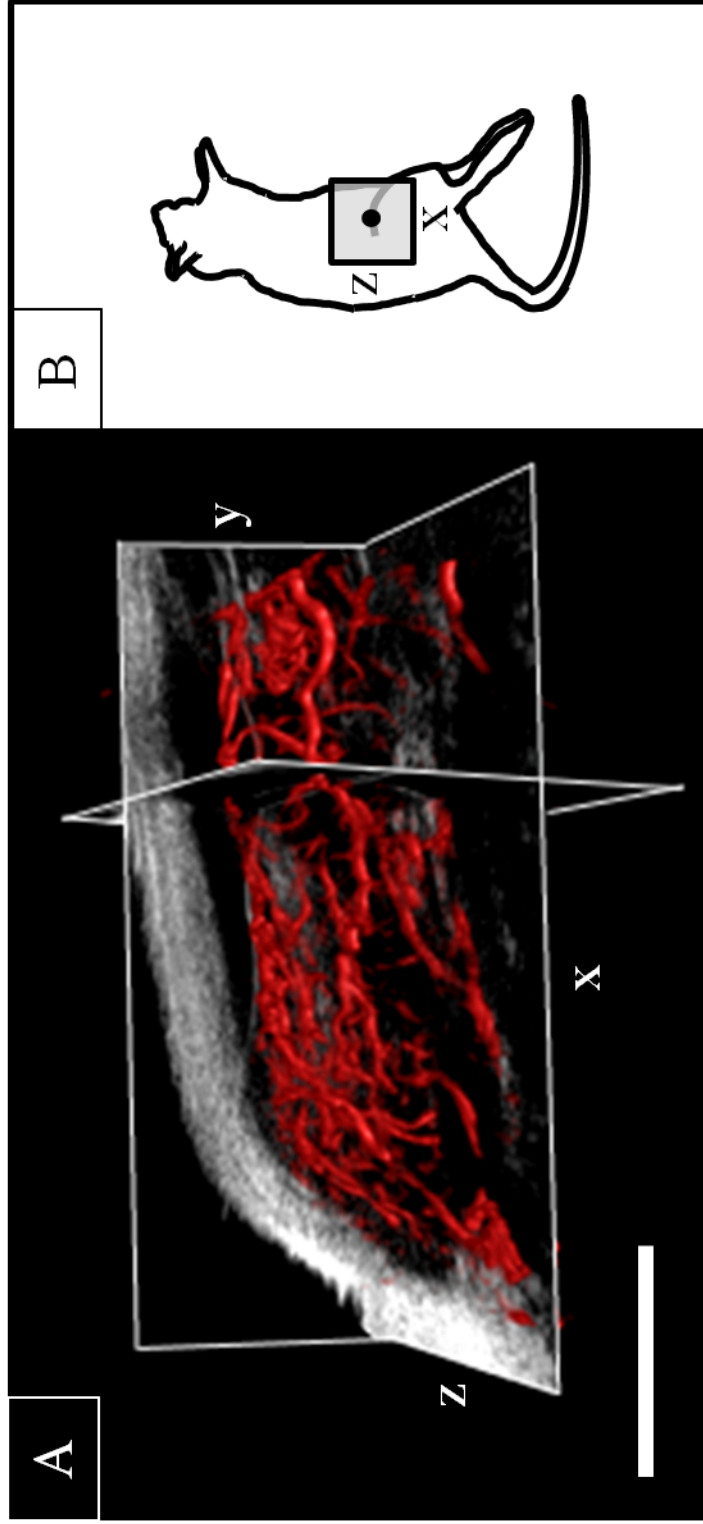


Figure 3.18: A: An overlay of the microvasculature within a tumor provided by acoustic angiography (red) onto a tissue-only image provided by high frequency b-mode (grayscale). This figure was created using 3D Slicer with a 3D rendering of the acoustic angiography data simultaneously displayed with a grayscale orthoslice of the b-mode data. Displaying data in this fashion illustrates microvessel and tissue morphologies, as well as vascular-tissue integration. Scale bar = 0.5 cm. B: A cartoon illustrating the approximate location of this 3D image volume.

Figure 3.19 depicts both b-mode and acoustic angiography images of the microvasculature surrounding two different tumors versus microvasculature from two normal tissue volumes. Differences in the vascular architecture within these two types of tissue volumes are immediately observable. Highly tortuous vessel structure is typical of angiogenic tumor vasculature [48; 35] and is not observed with as much frequency in the data for the healthy flank as it is in the tumor-bearing tissue volumes (Figure 3.19). Moreover, the angiogenic nature of tumors can be visualized by the many vessels gravitating toward the tumor lesion. Further analysis of microvasculature morphology is outside of the scope of this section, though appears later in this dissertation (Chapter 5.1). These images provide compelling evidence of the possibility of applying this imaging technique toward quantitative approaches to assessing vessel architecture.

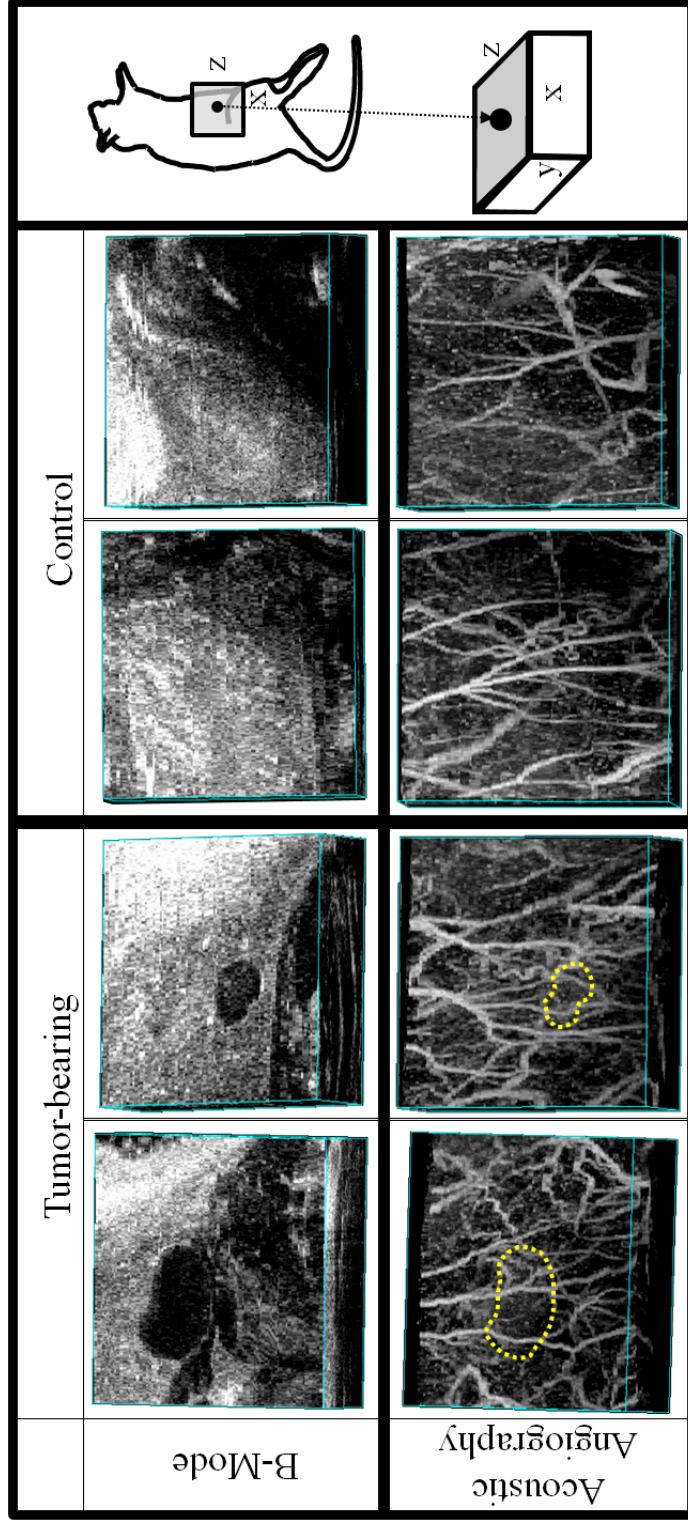


Figure 3.19: Multiple comparisons of 3D tissue volumes: two containing a tumor (left) and two healthy controls (right). The bottom images are acoustic angiography maximum intensity projections, while the top images are b-mode acquisitions of the same tissue volumes. The tortuous, and chaotic morphologies of the vessels in the presence of a lesion are contrasted by the relatively homogeneous vasculature in the healthy volume (tumor boundaries delineated in acoustic angiography image with dotted line). Image volumes = approx 0.75 x 1.25 x 1.5 cm (axial, lateral, elevational). A cartoon on the right indicates the imaging location and orientations of image volumes.

## Acoustic angiography compared to photoacoustic imaging and micro-CT

To compare acoustic angiography images against images acquired with a photoacoustic imaging system, we present data of subcutaneous microvasculature in rodents with both imaging methods. Figure 3.20A illustrates vasculature in the lower abdomen of a rat acquired with contrast ultrasound at transmit 4 MHz and receive 30 MHz. Figure 3.20B illustrates vasculature around the abdomen of a mouse obtained by photoacoustics using an excitation wavelength of 590 nm as acquired by [107]. The ultrasound transducer in the photoacoustic apparatus was a 38  $\mu\text{m}$  thick FPI polymer spacer, with a -3 dB acoustic bandwidth of 22 MHz. Its frequency response is characterized by a smooth roll-off, with its zero response occurring at 58 MHz [107]. In this image, the photoacoustic resolution was approximately 90  $\mu\text{m}$  (depth) by 130  $\mu\text{m}$  (lateral), and the imaging depth of field was 2 mm. The acoustic angiography images are of lower resolution (approximately 150  $\mu\text{m}$  (depth) by 200  $\mu\text{m}$  (lateral)), however illustrate a greater depth of penetration in this particular data set (5 mm in this case). Although not presented here, newer photoacoustics techniques have illustrated sub-100  $\mu\text{m}$  spatial resolution at depths of almost 10 mm. [108] Similarly, we estimate that acoustic angiography could be achieved at depths up to several centimeters by reducing the receiving frequency, albeit at the expense of a reduced spatial resolution and with more background noise from tissue.

We also qualitatively compared acoustic angiography to contrast enhanced micro-CT. Coronal maximum intensity projections (MIP) through the ultrasound and CT acquisitions of the same kidney were performed (Figure 3.21). The CT dataset was reconstructed with a 100  $\mu\text{m}$  voxel grid, which resulted in an improved SNR, compared to the ultrasound image's 50  $\mu\text{m}$  voxel grid. Despite the slightly lower resolution of the ultrasound, previously measured to be approximately 150  $\mu\text{m}$  [102], the two imaging techniques illustrate similar anatomical microvascular features within the rat kidney.



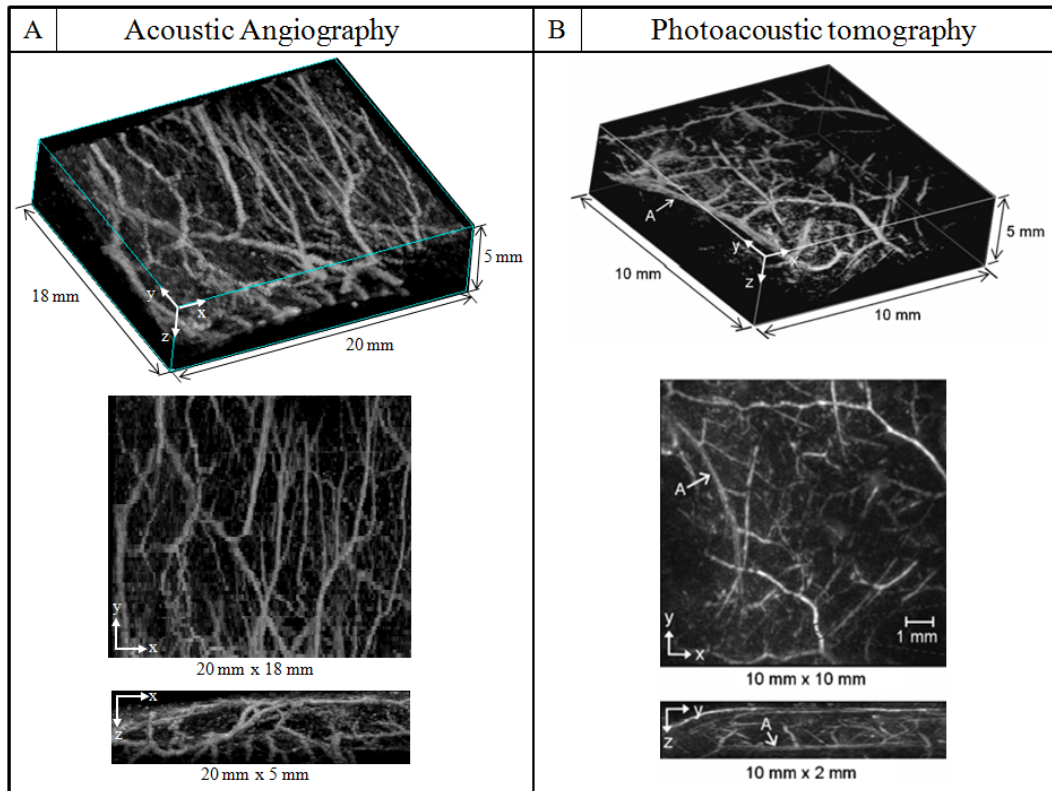


Figure 3.20: Comparison of acoustic angiography (A) to a photoacoustic imaging approach (B). The orientations of the acoustic angiography images have been purposefully arranged to mimic the photoacoustic images (adapted, with permission, from [107]) to allow a quick comparison between the two modalities. The imaging location in (A) is similar to the ones indicated in Figures 3.18 and 3.19

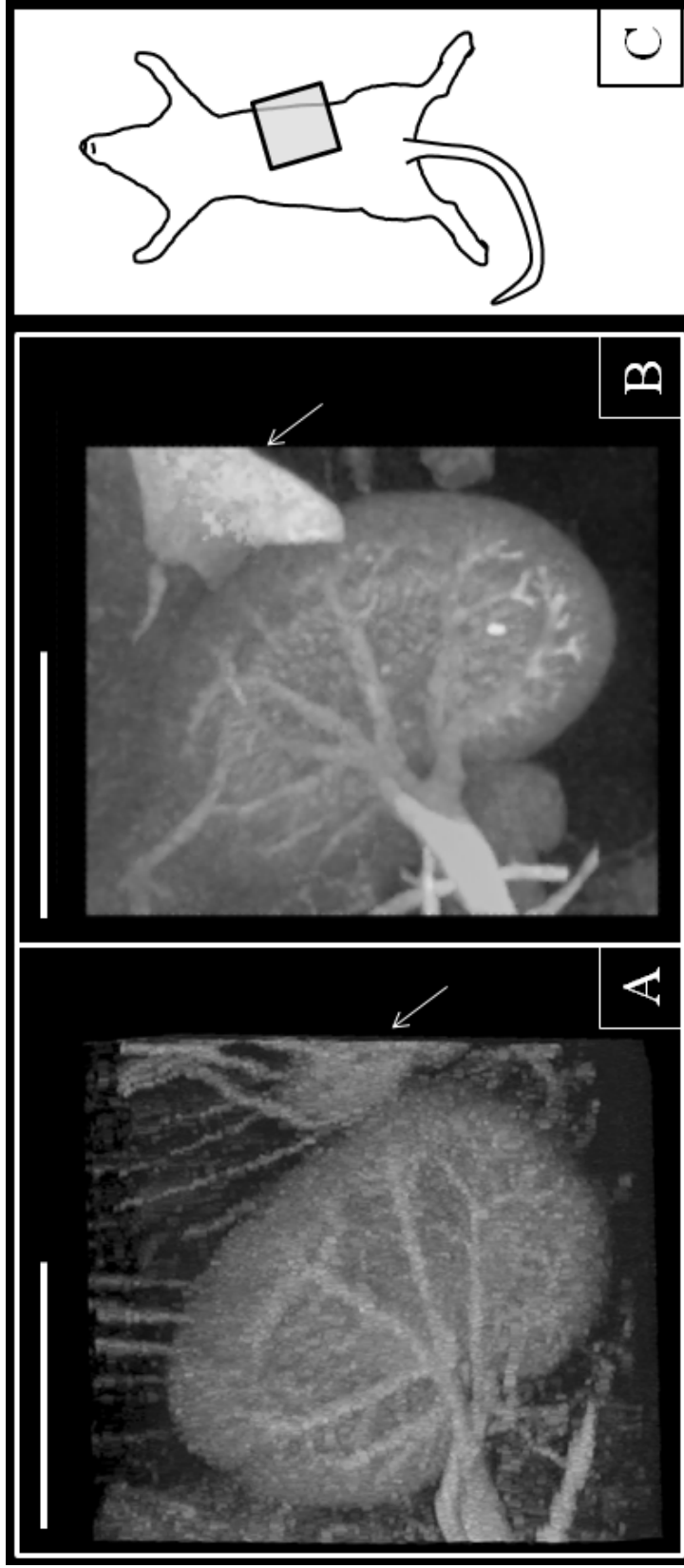


Figure 3.21: A comparison of maximum intensity projections of image data for the same kidney acquired with two different modalities: (A) acoustic angiography, (B) contrast enhanced CT. Scale bars in both images indicate 1 cm. The spleen is visible in each of these images to the right of kidney (arrows). A cartoon illustrates the approximate boundaries and orientations of these images (C).

### 3.3.3 Discussion and summary

The contrast ultrasound technology demonstrated herein has the capability to obtain high-resolution angiographic images of the microvasculature in rodents. This type of noninvasive and high throughput imaging technique could provide researchers and clinicians a new tool in the assessment of disease and response to therapy, while avoiding drawbacks associated with CT and MR, such as high cost, long acquisition times, and ionizing radiation dose (for CT). Although photoacoustics has advantages in improved resolution, optical techniques remain fundamentally limited with penetration depth.

The tradeoff between resolution and depth of penetration is the primary limitation of the acoustic angiography imaging approach. Due to the increased absorption of sound at high frequencies, penetration depth is limited to a few centimeters. For our prototype probe, this limitation is further exacerbated by the fixed focus of the transducer's current form factor, as not only does it suffer from a limited depth of penetration but also a fairly narrow depth of field (approximately 1 cm). However, this depth and depth of field are sufficient for nearly all mouse and most rat imaging. A transmit low-receive high array with dynamic focusing would alleviate this problem, though such an array has yet to be constructed in the frequency range optimal for small animal imaging. Another limitation of the acoustic angiography technique is the need for an imaging path unobstructed by strong acoustic reflectors; bowel gas and skull bone would hinder imaging, for example. Finally, because this is a contrast-based technique, the method does require an intravascular injection of microbubbles.

While the studies presented in this section are by no means comprehensive, the tissue signal suppression and microvascular imaging ability they have demonstrated motivation for the development of additional transducer designs to implement acoustic angiography. The approach could enable numerous applications for both preclinical and clinical interrogation of disease presence and response to therapy. Preclinical arrays

could be designed for larger animal models, such as for rabbit or dog imaging. It is possible that in each of these clinical and preclinical applications the presence of disease-associated vascular abnormalities could be detected by acoustic angiography, as could the modifications to these vascular networks (such as the elimination or normalization of tumor vasculature) by effective therapeutic regimens.

## CHAPTER 4

### TOWARD THE DETECTION OF ABERRANT VESSEL MORPHOLOGIES WITH ACOUSTIC ANGIOGRAPHY

The first section in this chapter describes a method to create microvessel phantoms to test the segmentation algorithm (Chapter 4.1) and the second section describes its implementation to test the limits of the microvessel segmentation algorithm's accuracy and repeatability (Chapter 4.2).

#### 4.1 3D microvessel-mimicking ultrasound phantoms produced with a scanning motion system

The development and implementation of ultrasonic vascular imaging techniques, along with their corresponding image analysis strategies, necessitates an understanding of their resolution and detection sensitivity as well as their sensitivity to corruption by the unfortunate realities of *in vivo* imaging studies, such as respiratory motion and signal attenuation. *In vitro* phantoms are utilized as a means to simulate anatomically relevant structures in a controlled environment to test sensitivity as well as the effects of

---

*Note:* This chapter has two sections, both of which draw from previous published material. Previously published material was reprinted with permission from the publishers.

**Chapter 4.1:** Ryan C. Gessner, Roshni Kothadia, Steven Feingold, Paul A. Dayton. *3-d microvessel-mimicking ultrasound phantoms produced with a scanning motion system*, *Ultrasound Med Biol*, 37(5):827-33, 2011.

**Chapter 4.2:** Ryan C. Gessner, Roshni Kothadia, Steven Feingold, Stephen Aylward, Elizabeth Bullitt, Paul A. Dayton, *Blood vessel structural morphology derived from 3D dual-frequency ultrasound images*, IEEE International Ultrasonics Symposium Proceedings. 2010

these variables. Blood vessel mimicking flow phantoms are often constructed of either acoustically transparent cellulose tubes set in gelatin for support, or wall-less gelatin bores through which contrast agents can be flowed and imaged. While these techniques are sufficient to test an imaging strategy's sensitivity or signal to noise ratio, they are suboptimal in creating environments for simulating blood vessel networks which have nontrivial structural details. Furthermore, attempts to simulate structural features in the hundred-micron range can be prohibitively difficult simply due to the challenge of working with materials on a sub-millimeter scale. This is a problem which most affects those seeking to characterize the structural morphologies of individual vessels or vessel networks as markers for disease.

Presented in this section is a novel method of generating individual 3D vessel phantoms with predefined coordinates of nearly any morphology. Our microvessel phantoms can be constructed with  $<10 \mu\text{m}$  precision. The technique is extended to the generation of entire vasculature networks via basic image addition of the independently constructed vessels. The principle behind our strategy is that an object is continuously imaged while also being translated in a controlled manner by a computer-controlled motion stage. If this motion occurs between imaging frames, it will appear smooth and continuous in the final 3D image. The strategy could be beneficial for determining the accuracy and sensitivity of imaging and image-analysis techniques seeking to quantify the structural morphology of vessels or vessel networks, as well techniques quantifying blood flow speed. It can also assist in determining imaging resolution, sensitivity to artifacts, and detection sensitivity for any of the ultrasound imaging strategies commonly implemented for vascularity assessment.

### 4.1.1 Materials and methods

#### Microcapillary and contrast agents

The complex microvessel flow phantoms generated in this manuscript were created by spatially manipulating a contrast-filled microcapillary during imaging. The microcapillary was a single thin-walled 200  $\mu\text{m}$  cellulose microtube (Spectrum Labs - Rancho Dominguez, CA) coupled with hot-melt glue to 380  $\mu\text{m}$  polyethylene tubes (Becton Dickinson, Sparks, MD). The cellulose tube region was imaged, while the larger polyethylene tubes were implemented to facilitate coupling with the syringe for contrast injection. A polydisperse distribution of perfusion microbubble contrast agents (mean diameter 0.9  $\mu\text{m}$ , standard deviation 0.45  $\mu\text{m}$ ) (Appendix A) were prepared and pumped through the tubes via coupling with a 27-gauge blunt needle. The tube was suspended in a water bath from one of the arms of a precision three-axis motion stage (Newport model XPS - Irvine, CA). A contrast-specific high resolution imaging method was implemented on a Vevo 770 ultrasound system (VisualSonics, Toronto CA), as previously described (Chapter 3.1).

#### Motion system

A custom LabView (National Instruments - Austin, TX) program was written on a personal computer (PC) to control the motion stage, as seen in Figure 4.1A. The transducer was positioned above the tube, with the tube's axis oriented normal to the imaging plane, and parallel to the direction of the transducer's translational motor stage as seen in Figure 4.1B. The frame trigger from the ultrasound system was used to trigger the PC, which then activated the motion stage to move the cellulose tube to the next X-Y coordinate in its centerline. The imaging system was set to acquire images at a fixed rate of 2 Hz, and the motion stage would increment the position of the microtube once between each image frame acquisition. 3D images were acquired via

the ultrasound system’s stepwise translational motor stage, with an inter-frame step size of 0.05 mm. This yielded isotropic voxels in the resulting 3D images.

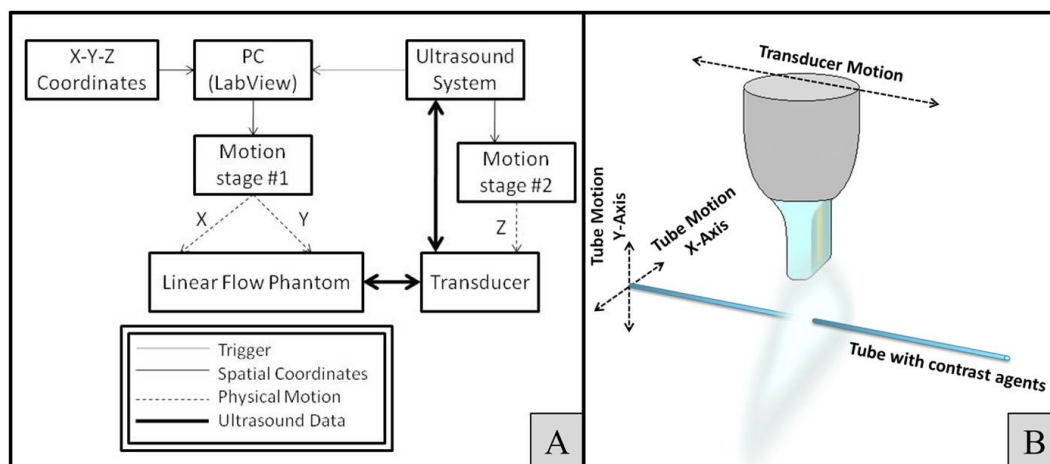


Figure 4.1: (A) Schematic block-diagram of the phantom generation system. Motion stages 1 and 2 correspond to the Newport and VisualSonics stages, respectively. (B) Drawing schematic of the spatial relationships between the physically moving components of the setup.

## Image acquisition

Prior to phantom imaging, X-Y-Z coordinates of the desired vessel’s centerline were generated in Matlab (The Mathworks - Natick, MA) and exported as tab-delimited text files. For the remainder of this manuscript, the X, Y, and Z axes correspond to the transducer’s lateral, axial, and elevational directions respectively. Any arbitrarily-shaped vessel curve could be generated, provided the resulting centerline did not fail the “vertical line test” in the X-Y plane. This caveat was due to the method by which we were acquiring our 3D images: the transducer only would acquire a single image at every Z location, thus it was impossible for a vessel to loop back on itself in the Z direction, although this could be done with future modification to the system.

Single vessel phantoms were generated and imaged with different morphologies, including helical-shaped and meandering vessels with random tortuosity added. Additionally, by summing up images of single vessel phantoms, we were able to create a



multiple vessel composite phantom to simulate a vessel network. Our methodology for 3D single vessel phantom generation is illustrated by the cartoon diagram in Figure 4.2. The transducer's Z position is in red, and is controlled by the ultrasound system. In these examples, as the probe is scanned the Newport motion stage moves the tube A) up and down, or B) in a circle within the 2D ultrasound imaging plane. The result is a sinusoid or a helix in the resulting 3D ultrasound image.

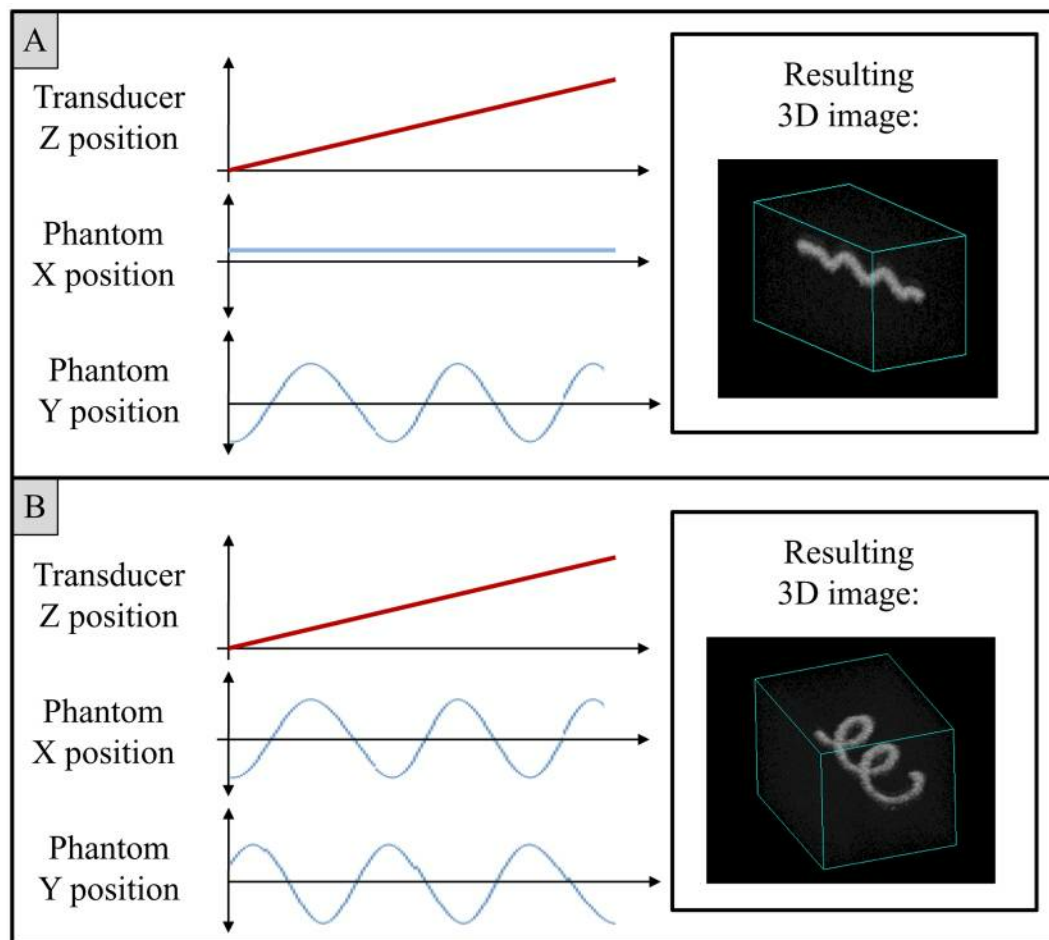


Figure 4.2: Two cartoons illustrating the methodology of simulating complex 3D vessel structures by independently controlling the X and Y locations of the vessel's centerline. Blue curves are controlled by the Newport motion stage. Red curves are controlled by the VisualSonics motion stage. (A) Sinusoid is generated. (B) Two out-of-phase sinusoids result in the generation of a helix

In order to use this system to assess contrast intensity as a function of axial depth

and pulsing pressure, coordinates were generated for a simple linear and diagonal phantom originating deep in the field of view and concluding very close to the transducer. The gradual slope of this phantom enabled a precise characterization of contrast sensitivity as a function of depth, in 100  $\mu\text{m}$  intervals (this distance is two pixels on screen). Moreover, by modulating the pressure output of the transducer, we characterized contrast sensitivity for depth of field over multiple pulsing pressures between 300 and 650 kPa.

#### **4.1.2 Results**

##### **3D tortuosity vessel phantom generation**

We discuss specifically the generation of two types of vessel phantoms of potential interest to those studying vessel structure and morphology. The first, seen in Figure 4.3, is a single vessel which develops tortuosity abnormalities along its path. In this study, a single gently meandering vessel, representing “healthy” vasculature has noise randomly added to the X and Y coordinate of each point along its centerline. The amplitude of the noise is modulated to create a more tortuous vessel. The most tortuous vessel has a mean deviation of 445  $\mu\text{m}$  from the healthy vessel’s centerline. This type of phantom could be utilized to simulate morphological abnormalities relevant to tumor response to treatment, as described by [37].

##### **Bifurcating vessel phantom generation**

Another type of phantom generated was a composite-vessel structure composed of multiple independent vessel phantoms. First, X-Y-Z coordinates were independently generated for each of the four vessels in Matlab, and the resulting four 3D images of each vessel added together to simulate a single continuous vessel network (Figures 4.4A-C). The 3D ultrasound image in Figure 4.4D was rendered in ImageJ (National Institutes of Health - Bethesda, MD). This vessel network was designed to have three different

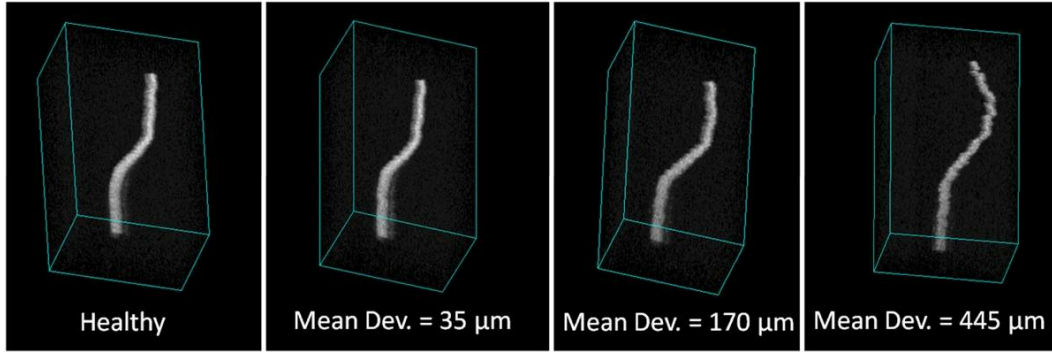


Figure 4.3: 3D maximum intensity projections of ultrasound data collected of various vessel phantoms. These phantoms represent simulations of a healthy vessel developing high spatial-frequency tortuosity abnormalities that are typical of cancerous vasculature. Mean deviations (Mean Dev.) from the healthy vessel’s centerline range between  $35\ \mu\text{m}$  and  $445\ \mu\text{m}$ .

bifurcations. At each bifurcation, the two daughter vessels diverge in opposite directions. Prior to a bifurcation, the daughter vessels resulting from that bifurcation trace equivalent paths to ensure smoothness at these junctions. By varying the angles at which daughter vessels diverge, one could simulate vascular changes due to the onset of disease. The angles at which vessels diverge have been linked to the presence of liver disease [32], with the fibrous tissue in diseased livers causing wider divergence angles between hepatic vessels. Thus, this type of phantom could be used to measure an imaging system’s sensitivity to these types of morphological changes occurring in *in vivo* vasculature.

### Measuring contrast sensitivity

By simulating a diagonal phantom oriented in the Y-Z plane, we were able to measure our contrast detection sensitivity as a function of imaging pressure and location within the field of view. The tube was raised in  $100\ \mu\text{m}$  increments between images, and was imaged at points  $\pm 6\ \text{mm}$  from the acoustic focus. Images were acquired at eight different pulsing pressures between 300 and 650 kPa. The data is summarized in Figure 4.5A, with a corresponding cartoon demonstrating the orientation of the transducer

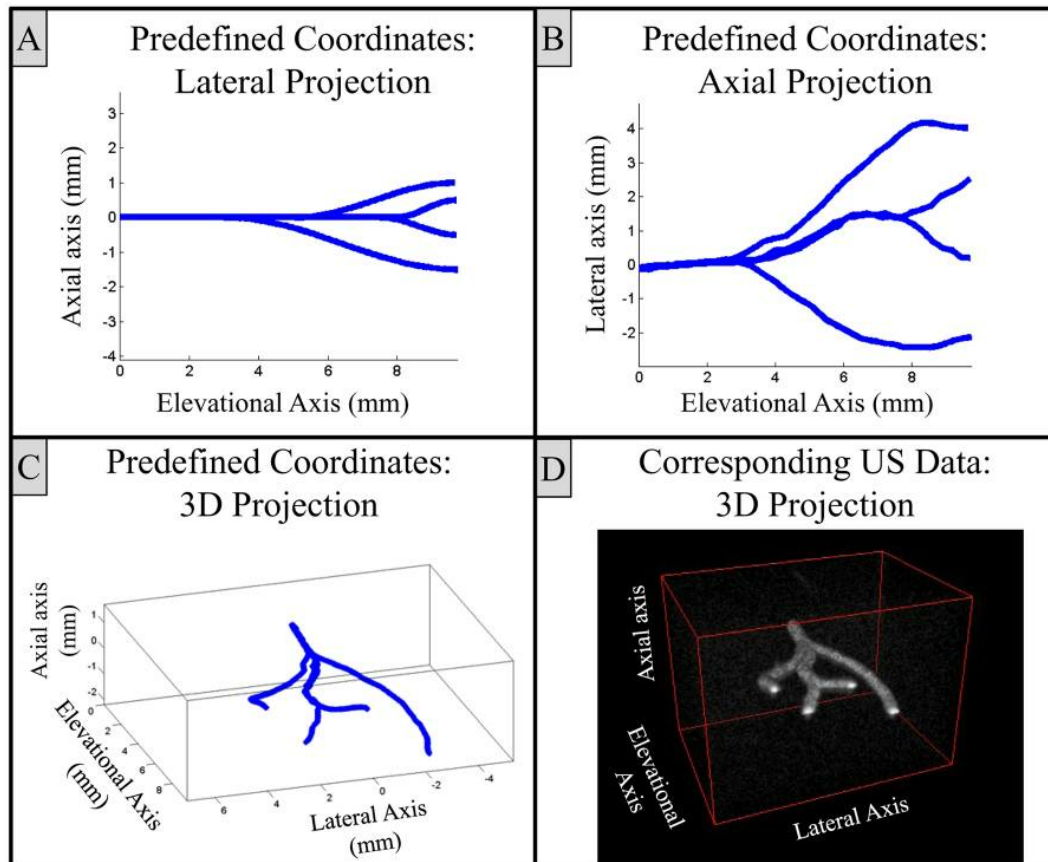


Figure 4.4: (A,B) Lateral and axial projections of 3D vessel network coordinate data, respectively. The network was designed so that all bifurcations result in daughter vessels diverging in opposite axial directions, as seen in (A). (C,D) 3D projections of vessel network coordinate data and ultrasound (US) data, respectively.

and tube in Figure 4.5B. The detection sensitivity in Figure 4.5A was quantified by averaging the pixels with image intensities above the noise floor in each 2D image in the 3D dataset. The phantom tube's mean intensities in each 2D image could be directly mapped to the distance from the tube to the transducer's focus since this relationship was governed by the coordinates used by the motion stage to create the phantom.

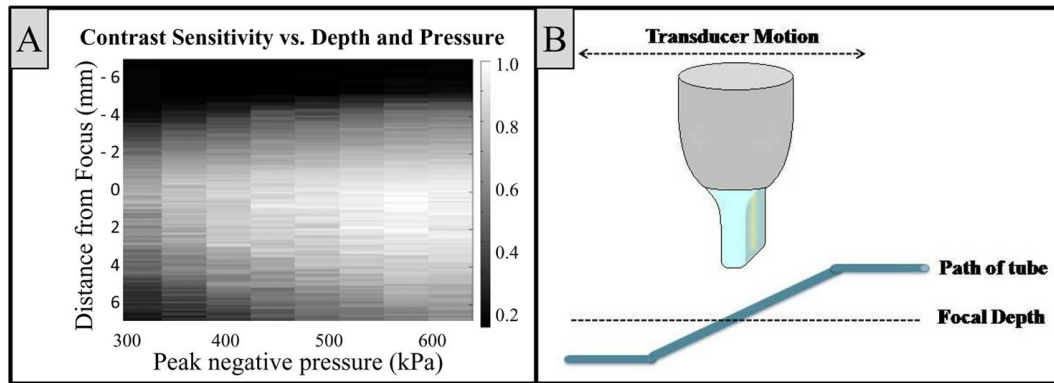


Figure 4.5: (A) An image displaying the sensitivity of our ultrasound probe to contrast as a function of pulsing pressure. The rows in this image correspond to the distance from the transducers focus to the tube. The columns in the image represent the discrete pulsing pressures tested between 300 and 650 kPa. (B) A drawing illustrating how the tube was moved to simulate a diagonal-sloped ramp phantom through 3D space.

### 4.1.3 Discussion and conclusions

#### Advantages of the phantom generation technique

The most enabling component of the technique described in this chapter for 3D flow phantom generation is the ability to create precise structures in the ultrasound data that would otherwise be prohibitively difficult or impossible to construct using conventional flow phantom materials. We have demonstrated the capability to generate phantoms with shapes such as helices, sinusoids, vessels with varying degrees of tortuosity, and bifurcating vessels; all with effective diameters on the order of  $200\ \mu\text{m}$ . Additionally, the micron-level accuracy of today's computer controlled motion stages offers fine control over phantom precision.

There exist other applications of this phantom generation technique which were not tested in these studies. For example, the motion stage-tube apparatus could be used to determine the sensitivity to slowly flowing blood by modulating the speed of the motion stage and measuring the reported flow speed against the known speed of the tube. One could also use the setup to simulate respiration artifacts of different magnitudes in order

to determine an imaging strategy's sensitivity to this reality of *in vivo* imaging studies. Finally, the approach could be used to measure an imaging strategy's resolution. If two tubes are simulated which pass through each other at a shallow angle of attack, the actual separation distance between the tubes' centerlines is known, so one could extract the last point at which they appear distinct and know the analogous physical separation between them (i.e. the imaging system's spatial resolution).

### **Limitations of the phantom generation technique**

While the phantom generation technique presented herein is a novel means to more accurately construct micro-flow phantoms for ultrasound imaging studies, there are several limitations of the technique worth noting. First and foremost, it must be implemented in a water bath, as the tube needs a smooth acoustically transparent medium through which to move. This then makes it necessary to add speckle noise as a post-processing step if one is interested in analyzing vessels in a more realistic imaging context. Since the process of building up vessel networks presented in this manuscript is via simple voxel addition, the signal to noise ratio between the vessels and the background noise in the final composite vessel images is spatially variant as a function of how many vessel signals are added together at a given location. The noise power increases uniformly throughout the image volume of the composite vessel phantom as each individual vessel phantom is added to the composite image; the signal power within the vessels does not always increase at all locations, however. In some locations of a composite image multiple vessels can be present, such as in the region before a bifurcation, and thus when they are added the final "vessel signal" increases  $N$  times (where  $N$  is the number of vessels present at a location). After vessels bifurcate and trace unique trajectories through the image space, their signals do not add any longer and thus are reduced relative to the increased noise power. While this was not

accounted for in these preliminary proof-of-concept imaging studies, one could compensate for this by characterizing the noise of the imaging system and normalizing the noise to the vessel signals in a post-processing step after the composite vessel networks had been constructed, as the centerlines of each vessel within the network are known. An additional limitation of the phantom generation technique is the amount of translation which can be used while still maintaining the illusion of a smooth and continuous tube through 3D space. Because the tube was oriented normal to the imaging plane, every 2D image has a nearly circular cut through the tube. If phantoms with steep angles relative to the plane of the image are created, the circular tube will need to translate many pixels between imaging frames and thus have a stratified appearance in the final 3D image. This effect can be partially accounted for by choosing small elevational step sizes. Although it was not necessary to consider the orientation of the tube relative to the imaging plane with our contrast detection strategy, those implementing Doppler techniques for contrast detection would need to take this into consideration to avoid the detection sensitivity issues associated with 90 degree Doppler angles. Additionally, if one is interested in achieving non-trivial velocity streamlines within a vessel phantom generated by the method presented herein, additional degrees of freedom must be added to their experimental apparatus. For instance, if one wanted to simulate a change in flow direction at a bifurcation they would need to rotate the transducer relative to the tube at the appropriate location along the vessel's centerline (or equivalently: rotate the tube beneath the transducer). This would become increasingly difficult in situations where a vessel's trajectory varied in both the X and Y dimensions, such as those in Figure 4.4, as the transducer would need to undergo two independent rotations. While not impossible, it is likely that this type of imaging procedure would be prohibitively difficult. Thus, we propose this phantom generation method as primarily of interest for those interested in assessing complex vessel morphology.

## 4.2 Quantifying vessel structure in controlled *in vitro* context

The work presented in this section demonstrates the use of a segmentation algorithm previously written for clinical MR images. It has been used to quantify total vessel number, vessel radii histograms, blood vessel density, number of vessel trees, number of branches within each tree, and several 3D quantitative measures of vessel tortuosity (distance metric, sum of angles metric, inflection count metric). To date, this type of vascular analysis has been challenging on preclinical ultrasound data. This was due to the difficulty of obtaining images of the microvasculature in 3D, with minimal tissue background. Our recent implementation of ultra-broadband contrast imaging with a prototype dual-frequency ultrasound probe (Chapter 3) has enabled the acquisition of 3D maps of rodent microvasculature with high resolution and a high contrast-to-tissue ratio. The objective of this study was to examine the feasibility of implementing our segmentation algorithm on this data. We estimate the limit of our imaging system's sensitivity to these quantitative metrics of morphology, and demonstrate the repeatability of our segmentation algorithm in this new imaging context.

### 4.2.1 Methods

#### Image acquisition

Images were acquired with a prototype dual-frequency transducer and a preclinical ultrasound system (Chapter 3). Our pulsing sequence was a single-cycle 2 MHz sinusoid and our receiving transducer had a 30 MHz center frequency with 100% bandwidth. A 10 MHz 7th order high pass filter was placed in-line with all received RF data, thus eliminating nearly all signal contributions from non-contrast agents. Perfusion contrast agents used in this study were implemented and had a mean diameter of  $0.9 \pm 0.45 \mu\text{m}$  (Appendix A).



## Vessel phantom creation

Vessel-mimicking flow phantoms were created from 200  $\mu\text{m}$  acoustically transparent cellulose tubes. Both the tendency of these tubes to crimp upon rapid changes in orientation, and their small size encouraged alternative means to simulate vessels with various morphologies in our *in vitro* setup. A novel method of simulating custom-shaped vessels in 3D with  $<10 \mu\text{m}$  resolution was implemented with a precision motion stage (Newport model XPS - Irvine, CA). A LabView (National Instruments - Austin, TX) program was written to control the position of the tube in each 2D ultrasound imaging frame, and was mastered by the frame trigger of the imaging system. Using predefined X-Y coordinates, the program would move the tube between imaging frames to different locations in the 2D image, and thereby effectively re-create a curved flow-phantom through 3D space. This approach is outlined in Chapter 4.1.

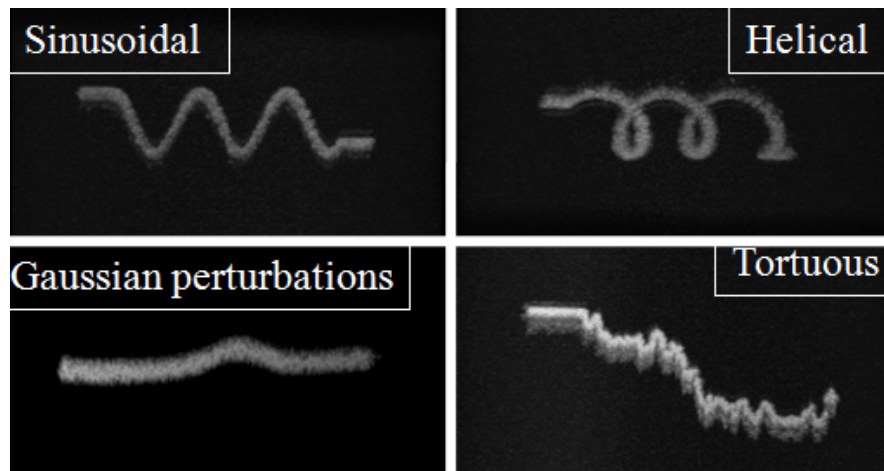


Figure 4.6: 3D maximum intensity projections of ultrasound data acquired of the various types of phantoms implemented in this study. The helical phantom is an extension of the sinusoidal phantom, with both x and y axes varied out of phase with one another.

Multiple vessel morphologies were simulated for this study: sinusoidal curves, straight lines smoothly perturbed by Gaussians, and meandering curves to which high frequency noise was added. These types are heretofore abbreviated SP (sinusoidal phantom), GP (Gaussian phantom) and TP (tortuous phantom) respectively. All phantom types were

used for the segmentation consistency analysis, and SPs were used for the segmentation sensitivity analysis. Examples of each type of phantoms can be seen in Figure 4.6.

### Vessel segmentations

Our vessel segmentation algorithm, originally developed in 1996 [109] has since been implemented extensively in human MRI images. [38; 37; 44; 110; 48] The algorithm is semi-automated, and it is initialized by a user-defined seed point in the center of a vessel. The user also provides an approximate radius for the vessel at the seed point location. The algorithm then iteratively tracks the vessel's centerline along both directions away from the seed point. The algorithm is guided by eigen values of the Hessian matrix calculated for the 3D image. The segmentation ends when any one of several criteria fail to be satisfied, such as vessel termination, encountering a T-junction with another vessel, or losing a circular cross section.[51]

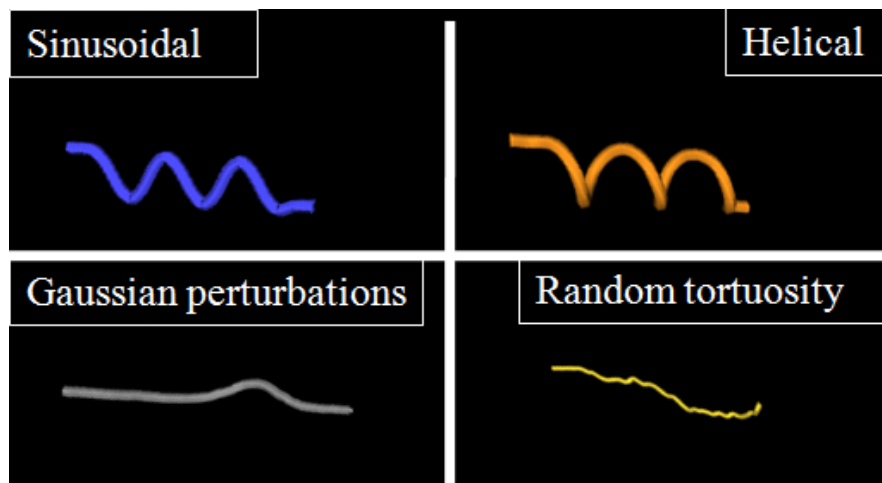


Figure 4.7: Example centerline segmentations corresponding to the ultrasound data in Figure 4.6

#### 1) Testing segmentation consistency

Two tests were implemented to estimate the consistency of our image-segmentation pipeline. The first tested intra-image repeatability (the same image segmented multiple

times), and the second tested inter-image consistency (the same phantom parameters imaged multiple times, and each image independently segmented). The three phantom types were imaged for this portion of the study: a GP with an amplitude of 1 mm and a FWHM of 2 mm, an SP with a period of 3 mm and an amplitude of 0.2 mm, and a TP with an average deviation from normal of 310  $\mu\text{m}$ . The 3D curves were generated in both the axial-elevational and the lateral-elevational planes, and are referred to as the “axial” and “lateral” phantoms, respectively. For the inter-image repeatability test, both lateral and axial phantoms were imaged five times and the vessel segmented from the images. For the intra-image repeatability test, one of the five images was randomly selected for both axial and lateral phantoms and the vessel within it segmented five different times with a random seed point location. Consistency was quantified by comparing both the tortuosity metrics output by the segmentation algorithm, and by comparing the maximum deviations and standard deviation of each point along the centerlines of the segmented vessel centerlines. “Deviations” in this case meant as the distance from the  $n$ th point of the segmentation to the mean X-Y-Z values of same  $n$ th point in all other segmentations for that vessel. In other words: if all five segmentations pass through the same voxel of the 3D image, then the deviation at that location of the centerlines would be reported as zero.

## *2) Measuring sensitivity to morphology abnormalities*

To estimate our sensitivity to subtle changes in vessel morphology, SPs were generated with various amplitudes between 0.05 mm and 0.4 mm. The lower end of this range was approximately the voxel size in our images. The quality of the resulting sinusoidal outputs were analyzed by comparing the extracted centerlines with the ground truth coordinates and determining the average displacement between the true centerline and the extracted centerline.

	Phantom type				
	SP-Lat	SP-Ax	GP-Lat	GP-Ax	TP
Max Dev.	0.042	0.022	0.073	0.023	0.187
Mean Dev.	0.013	0.008	0.033	0.003	0.038
Max Dev.	0.012	0.017	0.015	0.024	0.019
Mean Dev.	0.004	0.004	0.004	0.005	0.005

Table 4.1: Summary of segmentation consistency results. Deviation (‘Dev’) is assessed the distance from the true location of the vessel centerline. Note: and correspond to inter-image and intra-image segmentation tests, respectively. Units are in mm.

## 4.2.2 Results

### Vessel segmentations

All types of vessel phantoms were successfully segmented using our algorithm without the need to implement any post processing filtering strategies. Examples of these segmentations can be seen in Figure 4.7, which correspond to the analogous ultrasound data seen in Figure 4.6.

#### 1) Segmentation consistency

The inter-image segmentation and intra-image segmentation repeatability were both tested. A summary of these values can be found in Table 4.1, wherein deviations are reported as the displacement from the centerline. With the inter-image segmentation comparisons, there was a difference between the axial and lateral orientations of the SPs and GPs tested in this study, with both the mean and max centerline deviations being larger in the lateral cases for both. Additionally, there was a significant difference between all phantoms and the TPs. The maximum deviation was 187  $\mu\text{m}$ , which represents an approximately 4 voxel error, though the mean deviation of 38  $\mu\text{m}$  was much lower than this, and below the imaging system’s voxel resolution. The inter-image and intra-image consistencies were within 20  $\mu\text{m}$  and 5  $\mu\text{m}$  when averaged across all respective phantom types.

The two tortuosity metrics examined in this study, the distance metric and the sum

of angles metric, had inter-image variability of 0.29% and 4.27% respectively, while their intra-image variability was 0.09% and 3.68%. Thus, the small intra-voxel deviations had more effect on the sum of angles metric than the distance metric, though both were within 5% error for all cases tested. The intra-image segmentations demonstrated a much higher degree of consistency, on average 4 times more consistent across all phantom types. This was expected, as the only variable introduced in these cases was the random seed point. It is unclear whether the principle variable introduced in the inter-image segmentation causing the increased variability relative to the intra-image segmentations was the 3D phantom generation technique, or the irregular characteristics of the acoustic response from the tube.

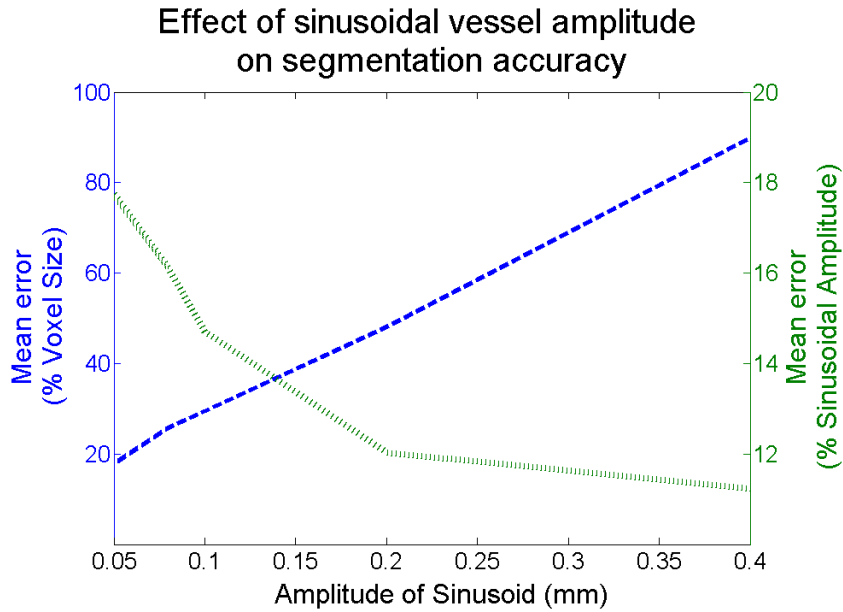


Figure 4.8: A plot demonstrating the effect of sinusoidal vessel amplitude on the resulting segmentation errors. While the mean segmentation error increases with increasing sinusoidal amplitude between 0.05 and 0.4 mm, the error when normalized to the feature size decreases.

## 2) Measuring sensitivity to morphology abnormalities

To test the sensitivity of our imaging-segmentation pipeline to tortuosity abnormalities, we generated multiple SPs and modulated the amplitude from 0.05 mm up to 0.4 mm.

The results of this test are displayed in Figure 4.8. Error was calculated by comparing the location of the segmentation with the ground truth location of the phantom at 200 discrete locations throughout the segmentation. The displacement between the true value and the measured segmentation was averaged for all segmentations. While the absolute deviations between the extracted centerlines and the true coordinates of the phantom were larger with greater sinusoidal amplitudes (darker curve), the magnitude of the deviations relative to the sinusoidal amplitudes increases as the sinusoidal amplitude approaches the size of the voxels in our images (lighter curve). While we did not examine curves with amplitudes below the 0.05 mm, we can say that our segmentations are accurate to within a single voxel ( $50 \mu\text{m} \times 50 \mu\text{m} \times 50 \mu\text{m}$ ) for all curves tested between 0.05 mm and 0.4 mm.

### 4.2.3 Conclusions and proposed future work

Our preliminary *in vitro* work presented in this manuscript demonstrates the possibility of implementing a blood vessel segmentation algorithm, originally written for the extraction of tubular objects from clinical MR angiogram images, in our ultra-broadband 3D contrast ultrasound images. We tested three different phantom morphologies at various spatial orientations and observed a high degree of repeatability in both intra-image and inter-image segmentations. Each of the consistency analyses was performed on five unique phantoms and tested five times per phantom. For these tests, the average deviations from the mean centerline were less than  $50 \mu\text{m}$ , which was the voxel size of our images. When the sensitivity was tested by comparing the accuracy of segmentations as a function of sinusoidal amplitude, we found that we maintained sub-voxel resolution for sinusoidal vessels with amplitudes between 0.05 and 0.4 mm.

Future work should focus on a more rigorous segmentation quality analysis. Monte Carlo simulations should also be performed, in which reported vessel morphology (via

the two tortuosity metrics) are set as the dependent variables, and noise, vessel structure, and initialization location randomized to more rigorously study the limits of the technique's sensitivity. Because these experiments were conducted in a noise-free water bath, special attention will be paid during the next stages of the *in vitro* work to ensuring that our methods will translate effectively *in vivo* by adding tissue-simulating noise after the phantom images are acquired. Additionally, the effects of frequency dependent attenuation (and thus loss of resolution) should be simulated. The eventual goal of our work is to implement our segmentation algorithm on 3D acoustic angiography images of diseased vasculature in order to improve sensitivity and accuracy of the ultrasonic assessment of response to therapy.

## CHAPTER 5

### DETECTING AND ASSESSING CANCER WITH ACOUSTIC ANGIOGRAPHY

For both studies, vascular features were extracted from acoustic angiography images acquired of *in vivo* cancerous lesions. The first study uses direct observations of vessel morphologies to detect the presence of a tumor (Chapter 5.1), and the second uses more global and indirect assessments of tumor perfusion to assess therapeutic response to radiation therapy (Chapter 5.2).

#### 5.1 Detecting aberrant vessel morphologies with acoustic angiography

Demonstrated herein is a combination of an algorithm for vessel segmentation, metrics for vessel morphologic analysis [52], and a high-spatial-resolution high-contrast imaging approach, which together form a system for vascular mapping. Similar vessel segmentation and analysis methods have been previously implemented for tissue disease and tumor response assessment in magnetic resonance (MR) angiographic data [111; 48; 110; 44]. The physics of dual-frequency contrast-enhanced imaging, which enables the acoustic angiographic approach essential to microvessel segmentation, have

---

*Note:* This chapter has two sections, one of which draw from previous published material. Previously published material was reprinted with permission from the publishers.

**Chapter 5.1:** Ryan C. Gessner, Stephen Aylward, Paul A. Dayton, *Mapping Microvasculature with Acoustic Angiography Yields Quantifiable Differences between Healthy and Tumor-bearing Tissue Volumes in a Rodent Model*, Radiology, 264(3), 733-740, Sept 2012

**Chapter 5.2:** Unpublished pilot study.



been previously described by Kruse and Ferrara [66], and the design of the prototype imaging transducer has been previously presented in [102]. The purpose of this analysis was to test our hypothesis that the morphologies of microvessels could be extracted from US images and used as a quantitative basis for distinguishing healthy from diseased tissue volumes in a rat model.

### **5.1.1 Materials and methods**

#### **Animal and contrast agent preparation**

All animal protocols used in this prospective study were approved by our institutional animal care and use committee. Animals used in this prospective study were female Fischer 344 rats (approximately 250 g, Charles River Laboratories, Durham, NC). A fibrosarcoma tumor model was established through the implantation of a 1 mm<sup>3</sup> sample of tissue in the right flank region of the animals as previously described [54]. Animals were imaged after the tumor had grown larger than 0.5 cm in each of the three principal axes. The right flanks of control (N = 7) and tumor-bearing (N = 10) animals were imaged. Prior to imaging, the area around the right flank was shaved with an electronic clipper. A depilating cream was also applied to remove the remaining hair in the area. A 24-gauge catheter was placed in the tail vein for the administration of contrast material.

Lipid-encapsulated microbubble contrast agents were prepared with the perfusion agent formulation (Appendix A), resulting in a polydisperse size distribution of contrast agents with a mean diameter of 0.9  $\mu\text{m}$  and concentration of  $1.3 \times 10^{10}$  bubbles per milliliter. Prior to intravenous administration, microbubbles were diluted in saline to a concentration of  $3.3 \times 10^9$  bubbles per milliliter. Contrast agent was continuously infused through a syringe pump (Harvard Apparatus, Holliston, Mass) at a rate of 70  $\mu\text{L}/\text{min}$ .

## **Image acquisition**

All images were acquired, processed, and analyzed by a PhD graduate student (R.C.G., with more than 3 years of experience working with high-spatial-resolution preclinical US images). Volumetric US images were acquired with a prototype probe described in Chapter 3.1. The difference between pulsing and receiving frequencies of this transducer enables the suppression of tissue signal, because echoes from tissue contain substantially less high-frequency harmonic content than those of microbubbles. The pulsing pressure for all images was 1.23 MPa (mechanical index = 0.62), with a 15-MHz high-pass filter used on the received lines of data to further suppress tissue signal.

Images were acquired with a frame rate of 3 Hz, with a five-frame averaging step at each location to suppress spurious signal from contrast agent flowing in vessels smaller than the spatial resolution of the system. Imaging began less than 1 minute after the initiation of contrast material infusion, and each three dimensional acoustic angiographic image required approximately 5 minutes to acquire. All three-dimensional images were acquired with an inter image elevational step size of 0.2 mm by using the linear motion stage of the US system. Control tissue volumes in this study were defined as the three-dimensional images acquired in non-tumorbearing animals, against which the images acquired in tumor-bearing animals were compared. The tissue imaged in the control animals was the right flank, which was the same location imaged in the tumor-bearing population. Both b-mode and acoustic angiographic images were acquired, enabling retrospective vascular-tissue overlays and the delineation of tumor boundaries.

## **Offline image analysis**

All image data were exported from the US system as uncompressed audio video interleave (AVI) files. The images were upsampled in the elevational direction by using a custom trilinear interpolation script written in Matlab (MathWorks, Natick, Mass) to

yield isotropic voxels with a width, length, and height of 0.05 mm. This interpolation helped expedite the vessel segmentation algorithm. Microvessels were extracted from each animal's image data by using the previously described vessel segmentation algorithm based on multiscale extraction of centerlines [51]. Previously described vessel morphologic metrics, the DM and SOAM [52], were then applied. Occasionally, a vessel would exhibit an extremely high tortuosity value, several standard deviations away from the mean for the animal from which it was extracted. These values may have been true estimates or may have been artifacts from the imaging or analysis method. To prevent these outliers from grossly skewing the distribution of vessel tortuosities, we excluded from further analysis any vessel with either a DM or SOAM value greater than 3 standard deviations from the mean for the animal from which it was extracted. As a result of this step, between zero and two vessels were removed from each of the 17 animals in the study, with an average of  $1.06 \pm 0.66$  vessels ( $\pm$  standard deviation) being removed per animal. This corresponds to an average of less than 4% (number of vessels removed from an animal divided by total vessels originally extracted from that animal) of the total vessels being removed as outliers from each animal (maximum of two vessels, minimum of zero vessels). Additional information about the statistics of vascular morphologies can be found in [112].

### **Statistical analyses**

Four types of variability in vessel tortuosity were assessed: interpopulation, intrapopulation, interanimal, and intraanimal. These types of vessel tortuosity variability are defined as follows. Interpopulation variability is the differences in vessel tortuosity occurring between group types (i.e., pooled tumor-bearing animals vs pooled control animals). Intrapopulation variability is the differences in vessel tortuosities occurring within a single population (a single tumor-bearing animal vs the pooled tumor-bearing

population). This is computed by taking the standard deviation of the average tortuosity values for each animal in the population. Interanimal variability is the differences in vessel tortuosity occurring between a single animal and one or more other animals of a different animal population (a control animal vs the pooled tumor population). Finally, intraanimal variability is the range in tortuosity values reported within a single animal (a large range suggests a more heterogeneous vascular network). The mean intraanimal variability is the average intraanimal variability across all animals in the population. The relative intraanimal variability is expressed as a percentage and is computed by normalizing an animal's original intraanimal variability (i.e. standard deviation) with the mean tortuosity value, thereby enabling comparisons between the variability of two different tortuosity metrics.

The statistical significance of the differences between the ensembles of microvessel segmentations of the two animal populations was assessed by using a two-tailed Student t test. Ensembles are defined as a collection of DM or SOAM values; they can consist of these tortuosity metrics computed on either the vessels extracted from a single animal or the pool of all vessels from the animals in a population. When animals were compared with their own group, equal variances were assumed for the t test; although when animals were compared with the opposite group, unequal variances were assumed. Three statistical comparisons were made between individual animals and their respective populations, as well as between the two animal populations themselves. The first comparison was used to test interpopulation variability in vessel tortuosity. All vessel segmentations were pooled into two groups, and the reported tortuosity metrics were compared to assess gross differences between the healthy and tumor-bearing populations. For this first comparison, a total of two tests were performed: the DM and SOAM ensembles from the tumor-bearing group versus the control group. The second comparison was implemented to test interanimal variability in vessel tortuosity. The

ensemble of tortuosity values reported for the vessels extracted from each tumor-bearing animal was compared against the pooled control population to allow us to retrospectively simulate a “diagnosis” of these animals (i.e., an individual patient’s image data compared with a healthy control population’s data set). Similarly, the ensemble of tortuosity values reported for the vessels extracted from each control animal was also compared against the vessels of the pooled tumor population. For this second comparison, a total of 34 tests were performed: the DM and SOAM ensembles for each of the 17 animals compared against the opposite animal group’s pool. Finally, a third statistical test was used to assess intrapopulation variability in vessel tortuosity. The ensemble of tortuosity values reported for the vessels extracted from each animal in the study was compared with the pooled aggregate of their respective population (with their own data removed from the pool) to assess the consistency of the tortuosity of vessels found within each of our two populations. For this third comparison, a total of 34 tests were performed: the DM and SOAM ensembles for each of the 17 animals compared against their own animal group’s pool. All three of these statistical tests were performed by using Matlab. For the first assessment, which tested the differences in vessel tortuosity between the vessels extracted from the two populations, statistical significance difference was set at  $p$  less than 0.05. In the second and third statistical assessments in which multiple comparisons were made, a Bonferroni correction was implemented and statistical significance difference was set at  $p$  less than 0.00147 (original significance level 0.05 divided by the 34 tests).

### **Estimating diagnostic utility of vessel maps**

In addition to testing the statistical significance of the differences in vessel ensembles (sick vs. healthy), an additional statistical test was conducted to evaluate how *many vessels* needed to be extracted in order to achieve the an accurate estimation of disease

state. This was performed by taking the complete vessel ensembles for all tumor-bearing animals and sampling between 4 and 30 vessels from each animal. These smaller pools extracted from the total ensembles were called ‘sub-samples,’ since they were a subset of the original. The process itself was called ‘retrospective subsampling’ because it was extracting these smaller pools from previously existing ensembles. The subsamples were compared on an animal-by-animal basis with the pooled control population’s vessel ensemble for both the DM and SOAM metrics. This process was repeated 1000 times at each sub-sample size (between 4 and 30) and the resulting  $p$  values for the statistical tests pooled. The rationale behind this experiment was to determine  $N$ , the number of vessels required, which would result in the average  $p$  value for this iterative retrospective test to fall below the 0.05 level. The statistical test performed was a two-tailed Student's  $t$ -test assuming unequal variance. All tests were performed in Matlab.

Receiver operator characteristic (ROC) curves were determined by using the pooled ensembles for the two animal groups (tumor-bearing vs. healthy) and were parameterized by the cutoff in tortuosity value which delineates the two populations. This value was modulated between the minimum and maximum tortuosity values reported in the study. The area under the curve was determined for both and used as a surrogate for diagnostic classification utility.

### **5.1.2 Results**

A total of 438 microvessels were extracted and analyzed from the acoustic angiography image data (Figure 5.1). The average number of vessels extracted from the image data of control flanks was 51.51% lower ( $15.86 \pm 2.41$  vessels; range, 13-19 vessels) than that of the tumor models ( $32.7 \pm 9.08$  vessels; range, 20-50 vessels). The average size of the 10 tumors imaged in this study was  $11.4 \pm 3.6$  mm (range, 5.8-16.8 mm) for the longest axis, corresponding to a volume of  $0.452 \text{ cm}^3 \pm 0.331$  (range, 0.070-1.076  $\text{cm}^3$ ). Examples

of segmented centerlines taken from acoustic angiographic image data can be seen in Figure 5.2. The average DM for the tumor population was 23.76% higher ( $1.34 \pm 0.40$ ) than that for the control population ( $1.08 \pm 0.08$ ) ( $p < 0.0001$ ) (Figure 5.3). The average SOAM was 50.73% higher in the tumor population relative to the control population ( $22.53 \pm 7.82$  compared with  $14.95 \pm 4.83$ ) ( $p < 0.0001$ ). The intraanimal variation for the DM was 0.07 and 0.33 (control vs tumor), which corresponds to a relative deviation of 6.60% and 24.90%, respectively. For the SOAM, the average intraanimal variation was 4.82 and 7.79 (control vs tumor), which corresponds to a relative deviation of 32.10% and 34.53%, respectively (Table 5.1).

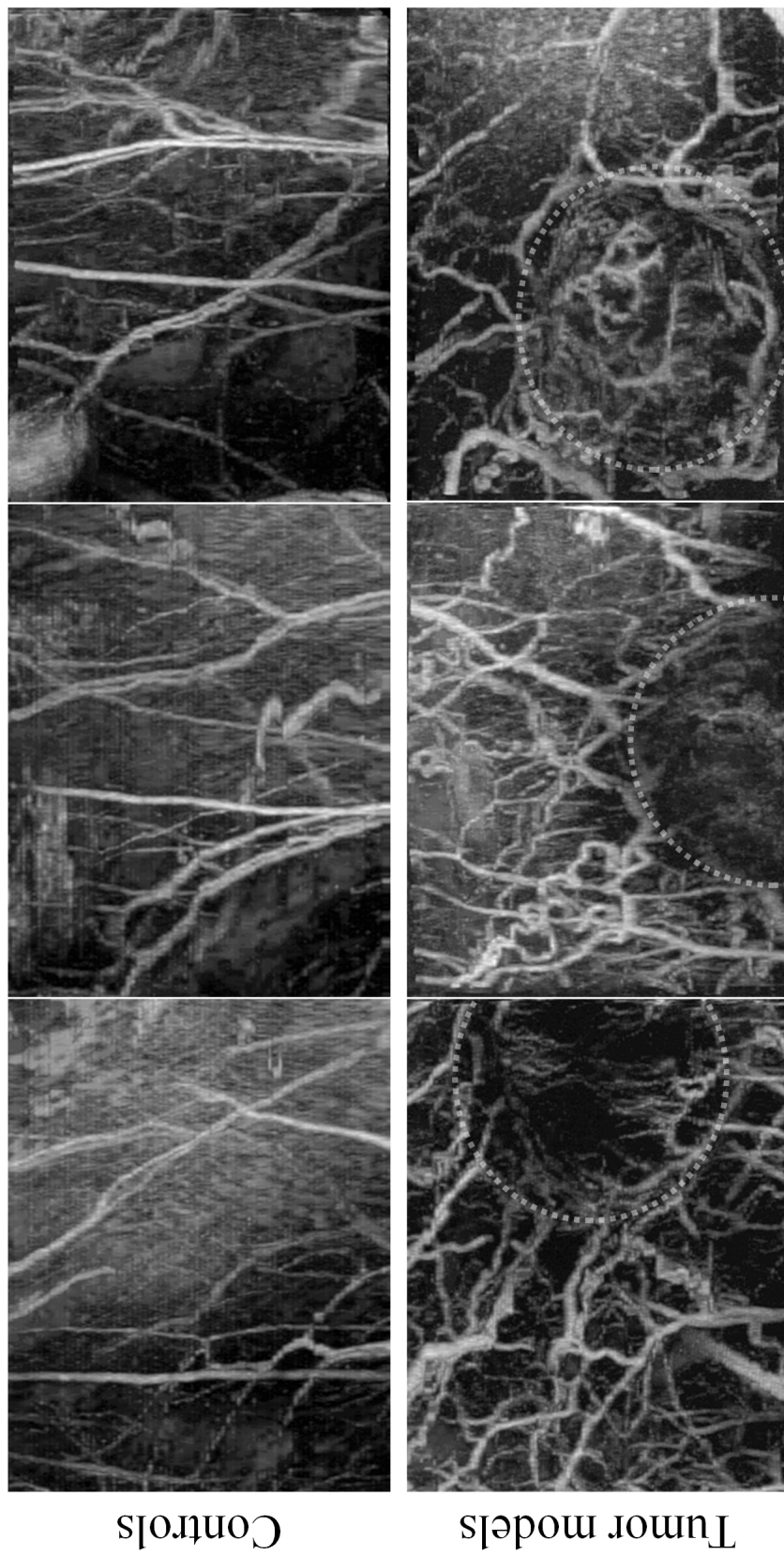


Figure 5.1: Maximum intensity projections through three-dimensional acoustic angiographic image data for six animals. Because these six three-dimensional data sets were projected along the axis of sound propagation, the resulting two-dimensional images are oriented in the coronal anatomic plane. The field of view for these images is 2.5 cm in the horizontal (lateral) direction and approximately 2 cm in the vertical (elevational) direction. Morphologic differences are apparent between the animal types both within and outside tumor margins. Dashed lines = approximate tumor boundaries.









	Control			Tumor		
						
DM	1.03	1.06	1.05	1.34	1.30	1.30
SOAM	6.59	14.64	7.57	19.07	29.74	20.85

Figure 5.2: Six extracted vessels show how different morphologic features influence the quantitative tortuosity metrics. A slowly meandering vessel will have a higher DM, and a vessel with high-frequency oscillations will have a higher SOAM.

The difference between the pooled DM ensemble for the tumor-bearing population ( $1.34 \pm 0.40$ ) and the control population ( $1.08 \pm 0.08$ ) was significant ( $p < 0.0001$ ) (Figure 5.3). Similarly, the difference between the pooled SOAM ensemble for the tumor-bearing population ( $22.53 \pm 7.82$ ) and the control population ( $14.95 \pm 4.83$ ) was significant ( $p < 0.0001$ ).

Parameter	DM		SOAM	
	Control Pop.	Tumor Pop.	Control Pop.	Tumor Pop.
Max	1.47	4.45	30.48	53.67
Min	1.01	1.01	4.64	7.05
Mean	1.08	1.34	14.95	22.53
Intrapop. var	0.08	0.40	4.83	7.82
Intraan. var	0.07	0.33	4.82	7.79
Rel intraan. var (%)	6.60	24.90	32.10	34.53

Table 5.1: Summary of the two tortuosity metrics for control and tumor-bearing animal populations. Computations for these quantities are found in the text.  
 Intrapop. var = intrapopulation variability,  
 Intraan. var = intraanimal variability,  
 Rel = relative (i.e. standard deviation divided by the mean)

	DM		SOAM	
	Pooled Controls	Pooled Tumors	Pooled Controls	Pooled Tumors
<b>Control Animals</b>				
<b>1</b>	0.62	†	0.75	†
<b>2</b>	0.66	†	0.47	0.0010*
<b>3</b>	0.025	†	0.41	†
<b>4</b>	0.63	†	0.19	†
<b>5</b>	0.09	†	0.18	0.002
<b>6</b>	0.61	†	0.95	†
<b>7</b>	0.09	†	0.99	†
<b>Tumor Animals</b>				
<b>1</b>	†	0.89	†	0.007
<b>2</b>	0.0002*	0.41	†	0.79
<b>3</b>	0.0002*	0.004	†	0.79
<b>4</b>	†	0.91	†	0.47
<b>5</b>	0.0006*	.76	0.0016	0.28
<b>6</b>	†	0.94	†	0.85
<b>7</b>	0.0005*	.81	0.0004*	0.38
<b>8</b>	0.0006*	.78	0.0002*	0.046
<b>9</b>	0.0056	.16	0.0014*	0.11
<b>10</b>	†	0.14	†	0.86

Table 5.2: Summary of  $p$  values for the statistical tests used to assess interanimal and intrapopulation variability in vessel tortuosity. Each cell indicates a comparison between the ensemble of vessel tortuosities for the animal in each row and the pooled population in each column.

\* indicates the  $p$  value is less than the Bonferroni-corrected  $p$  value of 0.00147.

† indicates  $p$  values are greater than 1 order of magnitude smaller than the Bonferroni-corrected  $p$  value of 0.00147.

The ensemble of tortuosity values computed from the vessels extracted from each tumor-bearing animal was compared against the pooled control population. The  $p$  value range for the 20 tests was  $2.42 \times 10^{-12}$  to  $5.63 \times 10^{-3}$ . Of the 20 tumor animal versus control group comparisons made, 18 had  $p$  values less than the Bonferroni-corrected  $p$  value of 0.00147. Similarly, the ensemble of tortuosity values computed from the vessels extracted from each control animal was compared against the pooled tumor-bearing population. The  $p$  value range for the 14 control animal versus tumor group tests was  $1.11 \times 10^{-16}$  to  $2.09 \times 10^{-3}$ . Of the 14 tests, 13 had  $p$  values less than the Bonferroni-corrected  $p$  value of 0.00147. A summary of the  $p$  values for these tests is listed in Table 5.2.

Finally, tortuosity ensembles for each of the animals were compared against the pooled vessel ensemble for their respective group to assess intragroup heterogeneity. Thirty-four comparisons were made: one for each of the two tortuosity metrics in all 17 animals in the study. (These tests can be visualized by comparing the distributions in Figure 5.3, A and C, with the animal's own population pool in Figure 5.3, B and D.) While some of these comparisons resulted in  $p$  values less than 0.05, none had  $p$  values less than the Bonferroni-corrected  $p$  value of 0.00147. This suggests that while marked differences between control and tumor-bearing animal groups were apparent (as per the first and second statistical assessments), the groups were fairly consistent relative to themselves. Despite their lack of significance below the Bonferroni-corrected  $p$  value, there were two animals in the tumor animal versus tumor group comparisons with  $p$  values less than 0.05 compared with only one animal in the control animal versus control population comparisons with  $p$  values less than 0.05 (Table 5.2). This trend could suggest that the degree of intragroup vessel morphologic heterogeneity was slightly greater in the tissue volumes containing a highly angiogenic tumor.

An exponential model was fit to the means of the  $p$  value distributions at each

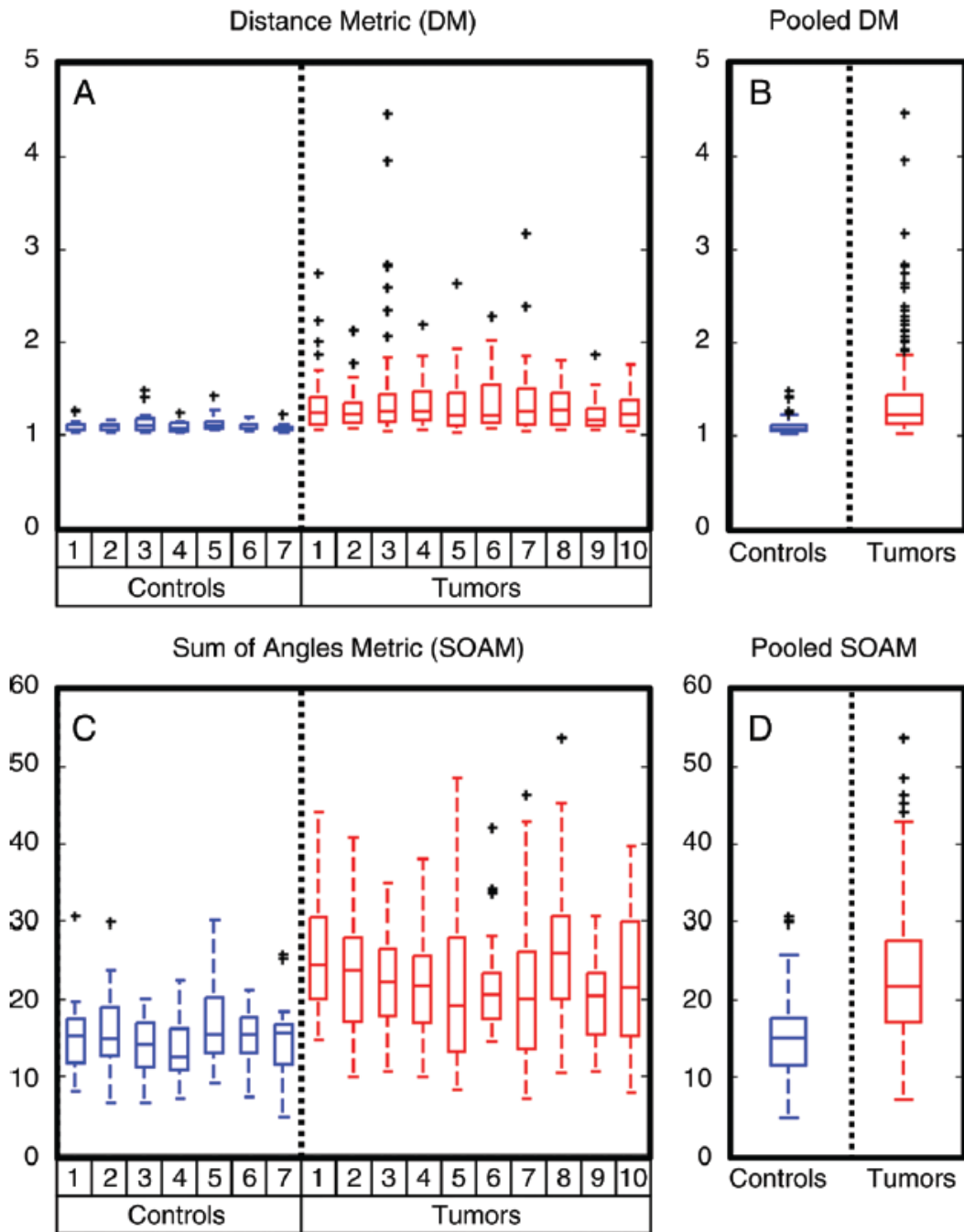


Figure 5.3: Box plots show the ensembles of the reported DM and SOAM values for the vessels extracted from the right flanks of the two different animal populations: healthy (Controls) and tumor-bearing (Tumors) animals. A, C, The ensemble of each animal in the study. B, D, The pooled ensemble for the control and tumor-bearing groups.

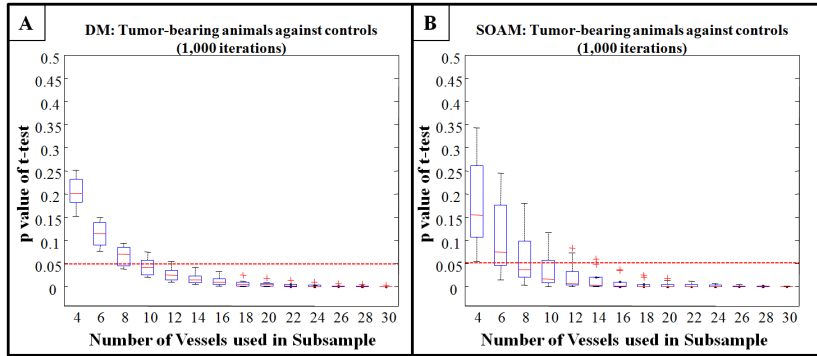


Figure 5.4: Box plots showing the  $p$  values determined by both DM (A) and SOAM (B) retrospective subsampling experiments. The 0.05 significance cutoff is shown in dotted red lines for both.

subsample size to determine the intersection with the 0.05 cutoff. The intersections were similar, with the DM and SOAM models intersecting the 0.05 cutoff at 9.45 and 9.17 vessels, respectively.

The results of the ROC analysis for the two pooled ensembles of vessels extracted from the tumor-bearing and healthy imaging subjects are presented in (Figure 5.5).

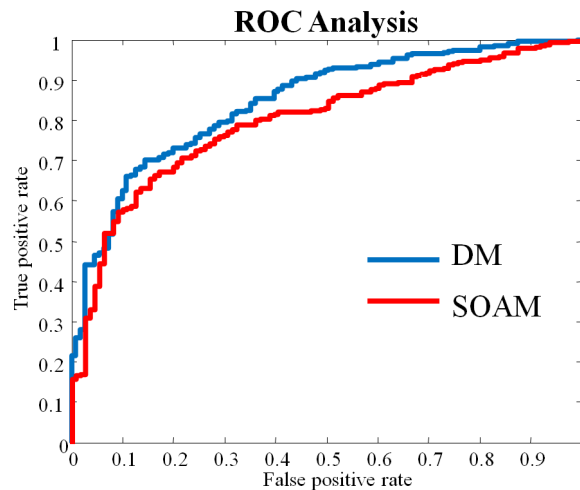


Figure 5.5: ROC curves determined from the pooled control and tumor-bearing vessel ensembles.

The area under the curve (AUC) for these two ROC curves were 0.84 and 0.80 for the DM and SOAM, respectively.

### 5.1.3 Discussion

In this study, we presented a high-spatial-resolution minimally invasive imaging approach and a quantitative analysis of microvessel structure extracted from these three-dimensional acoustic angiographic images. All tumor-bearing animals had significant increases in both of the reported tortuosity metrics (DM and SOAM) compared with those of the vessels in the control population. The results from this study indicated we can use microvessel centerlines extracted from high-spatial-resolution acoustic angiographic images to provide a quantitative basis for distinguishing healthy from diseased tissue volumes. The fact that animals within both control and tumor-bearing populations had significant differences from the aggregate pool of their respective groups suggests that heterogeneity is present within the microvasculature of these rodents, although our results also demonstrated there is a greater degree of vascular heterogeneity in the presence of cancer.

There were several limitations of this study. First, the prototype acoustic angiographic transducer enables excellent visualization of microvasculature but only within a narrow depth of field (1 cm) centered around the acoustic focus (located approximately 1.3 cm into tissue). This means that vasculature beneath tumors is rarely captured on our images unless the tumors are very small, nor are entire tumors visualized if their diameters in the axial direction exceed 1 cm. Further developments in transducer and US system technology would need to be achieved before acoustic angiography could be implemented clinically with widespread utility. Performance of this technique is currently in a similar realm of resolution and penetration depth as offered by photoacoustic imaging [113]. While photoacoustic imaging does not necessitate a contrast agent to interrogate the microvasculature - an advantage over our acoustic angiography approach - to our knowledge, there are not yet systems demonstrated in the literature

with simultaneous resolution and depth of penetration as utilized here. Typically, photoacoustic systems can achieve either similar spatial resolution at shallower depth of penetration [107] or similar depth of penetration at a lower resolution [114]. Moreover, these systems do not possess the portability offered by acoustic angiography, and they necessitate computationally intensive reconstruction algorithms to achieve volumetric imaging.

Another limitation of the study was tumor size heterogeneity. While the tumors imaged in this study were all at least 0.5 cm in diameter, they were not all the same size and thus not at the same point in the progression of the tumor model. Because tumor volume was not standardized across the tumor-bearing animal population, the degree to which the heterogeneity between subjects (tumor volumes, percentage of necrosis, growth rates, etc) affected the interanimal deviations in the reported DM and SOAM values is unknown. In addition, the relationship between tissue perfusion speed and vessel tortuosity remains to be studied with our acoustic angiographic imaging technique; however, this is of substantial interest because a previous human MR study demonstrated that these two techniques (vessel morphologic analysis and perfusion analysis) provide independently useful diagnostic information in the assessment of brain tumors [44]. Finally, the syngeneic tumor grafts utilized here likely will have different microvascular development characteristics than spontaneous tumors. Hence, although we have demonstrated the utility of the imaging and analysis techniques described here, the trends between tumor-bearing and healthy tissue may translate differently to human conditions.

Future studies using this quantitative morphologic analysis of vessel structure will test the relationship between vessel tortuosity and other ultrasonic methods for assessing disease state in genetically engineered animal models to compare their relative



sensitivities and uniqueness of diagnostic information. In addition, the temporal sensitivity of the technique will also be evaluated, because vascular tortuosity abnormalities have been observed when fewer than 100 cancer cells are present [35]; thus, techniques capable of resolving microvasculature are exciting candidate strategies for early cancer detection and rapid assessments of response to therapy. Practical applications: An ideal bedside clinical imaging modality is one which can sensitively, accurately, safely, and inexpensively predict therapeutic response, particularly in an era when medicine is becoming increasingly personalized. Thus, the capability of advanced US imaging and analysis techniques may have a substantial role in the future of cancer diagnostics and assessment. We predict that the technique for detecting the presence of cancer demonstrated in this article, with further development, could be used for rapid bedside disease assessment in several clinical settings.

## **5.2 Assessing tumor therapeutic response with acoustic angiography**

Over 20 years ago, the effects of single high doses of radiation on tumor vasculature were reported in a very elegant study on human melanoma cells in mice.[115] These effects were studied via the gold standard of histological analysis. Vascular effects were observed by perfusing the vasculature with a radio-opaque medium, and then taking x-ray images from subsequent histological tumor sections through the volume. This provided a time-intensive but effective method of quantifying various features of tumor vessel architecture, including vessel length, diameter, surface area, and volume per unit tumor volume. These studies demonstrated several interesting findings. First: a single dose of between 5 and 25 Gy could severely damage a large proportion of vasculature within the irradiated tumors, and this decrease in the number of functional vessels appeared between 3 and 10 days after irradiation. They observed a relationship between dose and size of vessel affected; about 35-45% of the original vessels with

diameters in the range 5-15  $\mu\text{m}$  were nonfunctional 1 week after doses of 10 to 15 Gy, while vessels with larger diameters required higher doses to be affected in the same amount of time. In their study they found that doses of 16, 21, and 20 Gy were required to knock out greater than 50% of vessels in the following respective diameter ranges: 5-15, 15-25, and 25-35  $\mu\text{m}$ . Finally: at their highest doses, they found that despite the considerable loss of tumor vessels following irradiation, tumors exposed to 20-25 Gy eventually became hypervascularized, and those tumors which eventually regrew could even be more vascularized than control (non-irradiated) tumors.

Many research groups have been attempting to leverage the fundamental advantages of ultrasound (cost, noninvasive nature, portability, realtime imaging) in cancer treatment followup studies, whether treated by radiation or otherwise. Table 5.3 lists several preclinical studies within the last 10 years which have implemented ultrasound vascular imaging approaches in preclinical studies assessing response to radiation therapy (either alone, or in conjunction with other anti-cancer agents). While clinically, radiation therapy is rarely used as a stand-alone treatment regimen for tumors, the subsequent effects of radiation on tumor vasculature can be visualized with several different ultrasound imaging approaches, and there is a wide array of existing literature, including the gold standard of histology mentioned previously [115], to which we could compare our own acoustic angiography imaging results. To this end, we designed an imaging study in which we could evaluate the efficacy of acoustic angiography at assessing the functional status of tumors during their response to radiotherapy. Tumors were irradiated by varying levels of radiation (0, 5, and 20 Gy), and were subsequently imaged over the following weeks. Naturally, because acoustic angiography is not yet widely available, there exist no studies in the literature demonstrating its utility in assessing tumor response to therapy.

Most of the preclinical studies performed to date implement power Doppler as their

Year	Animal Model	Tumor type	Treatment type		Ref
			Radiation alone	Combination	
2002	Rat	Breast		x	[116]
2003	Mouse	Lung/Brain	x		[117]
2003	Rat	Breast	x		[118]
2003	Rat	Breast		x	[119]
2005	Mouse	Lung		x	[120]
2006	Mouse	Lung	x		[121]
2007	Mouse	Lung		x	[122]
2008	Mouse	Prostate		x	[123]
2010	Mouse	Lung		x	[124]

Table 5.3: Recent studies implementing ultrasound vascular imaging approaches to assess various preclinical tumor models' responses to radiotherapy

method of spatially mapping blood flow. Power Doppler, if used with microbubble contrast, is much more sensitive to slowly flowing blood flow (i.e. the microvasculature in tumors) than the other widely implemented Doppler imaging approach, color Doppler. The principle drawbacks of power Doppler are (1) like acoustic angiography, it provides only a measure of the extent of blood flow (not a map of perfusion speeds), and (2) unlike acoustic angiography, it is highly susceptible to respiratory motion artifacts. It was our goal to evaluate tumor response to radiation therapy with acoustic angiography, and compare the observed results against previously reported values obtained by power Doppler.

### 5.2.1 Methods

### 5.2.2 Tumor model

All animal studies were conducted in accordance with approved protocols granted by our institution's IACUC. Fibrosarcoma tumor tissue samples, propagated from existing tissue as previously described [101], were implanted in the lower flank area of 15 female rats ( $126.8 \pm 7.4$  g) (Charles River Laboratories - Durham, NC). The volume of the tumor tissue was approximately  $1\text{-}2\text{ mm}^3$  at the time of implant. After 14 days, the

wound at the surgical site had healed and the tumors could be imaged with high frequency b-mode to evaluate tumor size. The animals were then randomized into the 3 treatment groups: 0 Gy, 5 Gy, and 20 Gy. In an effort to limit the effect of tumor size at time of therapy on resulting treatment efficacy, the distributions in tumor sizes between the 3 groups were tested for statistical significance (2 tailed Student's t-test assuming equal variance). If any of the three groups were significantly different ( $p < 0.05$ ) than another group, the groups were randomized again and re-tested for significance.

### **Tumor irradiation**

14 days after tissue implantation, the animals were imaged, sorted into their groups, and taken to the UNC Cancer Hospital for treatment. To avoid the possibility of patient exposure to the animals, the irradiations were performed after normal hospital operating hours as per the IACUC protocol. A clinical broad beam system was used (Siemens PRIMUS linear accelerator) for all treatments. Animals were treated one by one; prior to each treatment, animals were anesthetized in an induction chamber with 5% isoflourane-95% oxygen gas. They were then transferred to the computer controlled patient stage beneath the treatment gantry, where anesthesia was maintained via mask delivery at 2% isoflourane. (Figure 5.6A)

Each animal was palpated to identify the tumor location, and the center of the tumor was indicated on the skin's surface using a permanent marker. The animal was then positioned appropriately such that the beam was centered at the tumor's center. A targeting light beam, coincident with the treatment beam, was used to position the animal (Figure 5.6B). A beam size of 1.8x1.8 cm was used to ensure adequate coverage of radiation dose, as this was larger than any tumor's diameter at the time of treatment (the largest tumor was 1.2 cm in diameter). A depth of 1.4 cm was used for treatment targeting, and a 1 cm bolus was used to ensure maximum dose was delivered to the

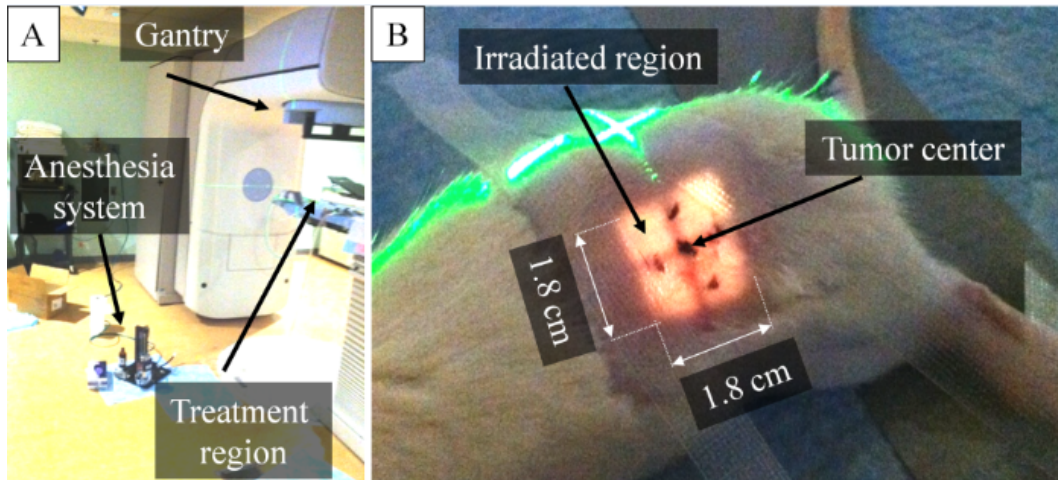


Figure 5.6: Labeled images of (A) the clinical irradiation system setup, (B) a top-down view of an animal immediately prior to an irradiation procedure.

center of the tumor (0.4 cm into tissue) in the depth dimension. The doses delivered to each animal were either 0 Gy (monitor unit = 0, control animals), 5 Gy (monitor unit = 559) or 20 Gy (monitor unit = 2234) with 6 MV x-rays.

It is well known that radiation has an adverse affect when interacting with the tissues within the gut. A previous study showed irradiating the exteriorized intestine of rats at 15.5 Gy (i.e. radiation damage limited to gut alone) the mean survival time was only 7.1 days. [125] Thus, because the tumors used in this study were placed on the lower flank above the lower abdomen, it was our goal to understand the extent of non-tumor tissues which could have been affected by the irradiation. We designed an experiment to estimate which non-tumor tissues had interacted with the radiation beam in which a synthetic beam was created and overlaid on a 3D micro CT image of a rodent (data acquired from an open access institute). The open source image visualization and analysis platform 3D Slicer ([www.slicer.org](http://www.slicer.org)) was used to manipulate the location of the beam, and visualize the two datasets (beam and animal) concurrently. The dataset was not for a rat, as was used in our studies, but because mice and rats have

---

“Digimouse Download” at <http://neuroimage.usc.edu/neuro/>

proportionally similar anatomical structures it was assumed to be sufficiently accurate for our purposes. The beam was a logical mask (assumed to be a step function in radiation intensity), square in cross section, and extended through the entire height of the image. To account for the slight variation in tumor locations within the lower flank, the beam was made 50% larger than was experimentally applied (1.8 x 1.8 cm in cross section) to account for inter-animal variability in dose.

### Imaging studies

Each imaging study consisted of the acquisition of two types of images: b-mode for the localization of tumor tissue relative to surrounding tissue types, and acoustic angiography for the assessment of vascularization within the tumors. Animals were imaged immediately prior to irradiation (Day 0) and then at Days 3, 6, 9, 12, and 18. A pictorial representation of this timeline is provided (Figure 5.7). Tumors were imaged until they grew larger than 1.5 cm in the largest axis, or if they were predicted to surpass this size by the following imaging study.

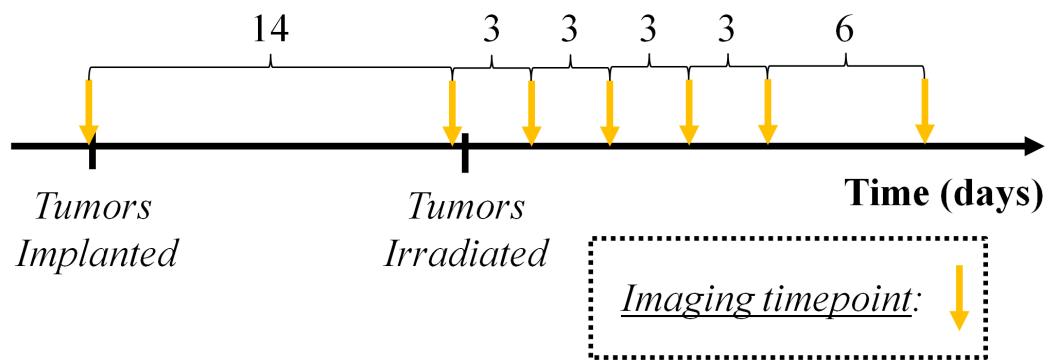


Figure 5.7: A timeline illustrating the tumor implantation, imaging, treatment schedule. Relative distances between events are to scale.

Microbubble contrast dose and infusion, and ultrasound imaging parameters were the same as previously described [101]. Animals were weighed after each imaging study to monitor their health after radiation treatment. If any animals lost more than

5% of their weight (relative to Day 0) flavored high protein dietary supplements were provided to all animals in that treatment group, and daily subcutaneous injections of sterile saline administered in 3 mL boluses to all animals in the treatment group. These infusions and dietary supplements were provided to counteract the weight loss due to treatment-induced nausea.

### **Image analysis**

Three metrics were examined at each imaging timepoint for this study: animal weight, tumor volume, and tumor perfusion ratio. The latter two were computed by first defining a 3D region of interest (ROI) to the location of the tumor. This is normally accomplished with frame-by-frame manually defined ROIs which then assemble into a 3D binary logical mask (1's inside the tumor boundaries, 0's outside) of the same size as the original 3D image data. This can be a time consuming process, however, as a 1 cm tumor imaged with an inter-frame spacing of 150  $\mu\text{m}$  has over 60 images which require ROIs. With 15 animals and many timepoints per animal, it was estimated that ROI definition alone would have necessitated over 13 hours (assuming 10 seconds per ROI, and a range of tumor sizes between 0.5 and 2 cm in diameter). Instead, a more efficient method was explored in this study, which exploited the elliptical shape of the FSA tumor being imaged and would not tax the limits of human patience to the same degree. A custom Matlab function was written which required the user to manually define ROIs in 3 orthogonal planes through the center of the tumor (Figure 5.8). These user-defined ROI perimeters represented a 3D cloud of points surrounding the tumor, to which a volumetric ellipsoid could be fit. Preliminary studies revealed that the accuracy of these semi-automated elliptical ROIs was comparable to the aforementioned frame-by-frame ROIs (data not shown), and could be fully defined for each tumor in, at most, 40 seconds.

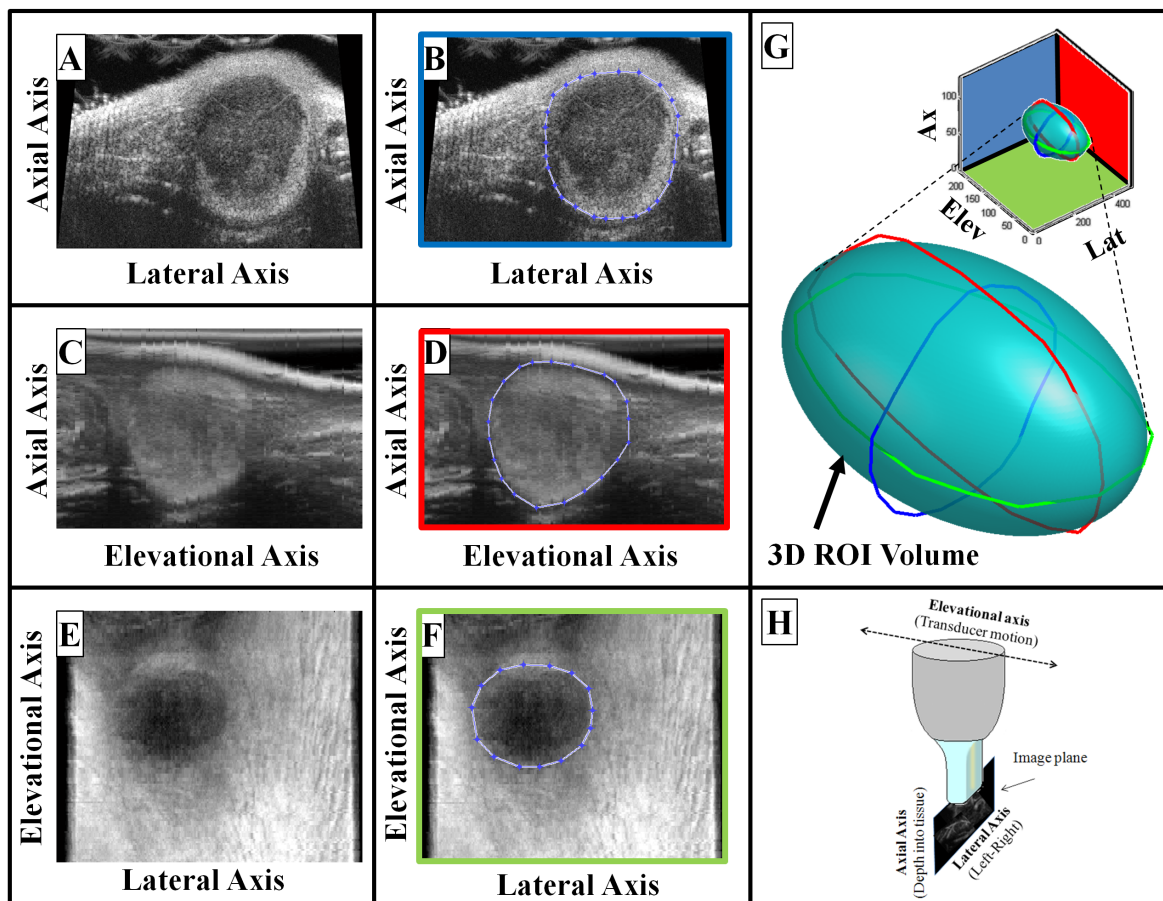


Figure 5.8: An illustration of how the regions of interest were defined in this study. The left column (A,C,E) is identical to the middle column (B,D,F) notwithstanding the overlaid user-defined boundaries of the tumor. G shows a rendering of the 3D ellipsoid fit to the data defined by the curves shown in (B,D,F). The color of the frame boundaries corresponds to the three orthogonal curves in (G). H: a cartoon schematic illustrating the orientation of the 3 planes relative to physical space.



Using these 3D ROIs, both tumor volume and perfusion ratio metrics could be computed. The tumor volume was computed as the sum of all voxels in the ROI multiplied by the voxel size (0.05 x 0.05 x 0.15 mm). This yielded a measure for volume in units of mm<sup>3</sup>, or equivalently:  $\mu\text{L}$ . The second metric, the volumetric perfusion ratio, was a unitless estimate between 0 and 1 of the proportion of the tumor’s volume which was occupied by perfusing vessels. This was computed by determining the volume of voxels within the 3D ROI which were above the noise floor, and dividing by the total volume of the ROI. The noise floor was estimated by randomly sampling several images, and determining the value of intensity of the image within non-perfused tissues. This is a similar metric as the “power Doppler index,” as was used by many of the studies listed in Table 5.3.

### 5.2.3 Results and discussion

After randomization prior to treatment (Day 0), the tumor size distribution for the three treatment groups was as follows:  $196.3 \pm 69.2 \text{ mm}^3$  (0 Gy),  $261.3 \pm 281.7 \text{ mm}^3$  (5 Gy), and  $175.4 \pm 87.4 \text{ mm}^3$  (20 Gy) (Figure 5.9) These volumetric estimations of volume correspond to average tumor diameters of  $(7.18 \pm 0.86 \text{ mm})$ ,  $(7.28 \pm 2.54 \text{ mm})$ , and  $(6.77 \pm 1.34 \text{ mm})$  for the same groups respectively.

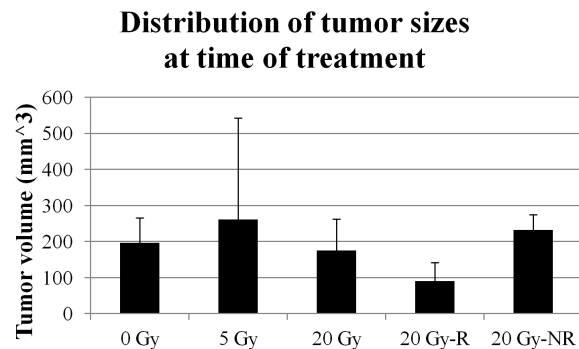


Figure 5.9: The means and standard deviations of the tumor volumes in each of the treatment groups prior to therapy. The 20 Gy treatment group is split into two subsets (R: ‘responder’, NR: ‘non-responder’).

The untreated tumors all surpassed the maximum allowable size by Day 6, and all but 1 animal in the 5 Gy group was culled by day 9. (Figure 5.10) None of these animals were significantly affected by the irradiation at 5 Gy. The animals irradiated by 20 Gy were all below the critical size threshold until Day 18. It should be noted that although three of the 20 Gy animals were sacrificed at the Day 18 timepoint, it was not because the tumors had necessarily grown to a large size at this time. Rather, these 3 animals (hereafter referred to as the “20 Gy non-responders”) experienced an inflection point in their growth curves at this timepoint. As a result of scheduling logistics, it was not possible to image any animals between the Day 18 and Day 28 timepoints, and thus it was prudent to sacrifice them, thereby not allowing their then-growing tumors to exceed the allowed size during that 10 day period. At Day 28, the two animals remaining in the study (hereafter referred to as the “20 Gy responders”) did not have tumors detectable by high frequency b-mode or manual palpation.

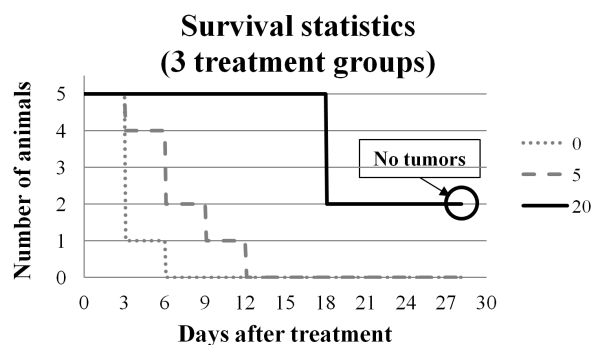


Figure 5.10: A survival curve illustrating the number of animals remaining at each timepoint within the three different treatment groups. The two animals remaining at Day 28 were the responders.

### Radiation induced weight loss

By Day 5 it was evident that animals in the 20 Gy group were losing more weight than their counterparts in the 0 and 5 Gy groups. The average percent change in weight on Day 5 was  $-5.89 \pm 3.75\%$  in the 20 Gy group compared to  $-1.22 \pm 1.30\%$  and  $-1.39 \pm 1.49\%$

in the 0 and 5 Gy groups, respectively ( $p = 0.06$  and  $p = 0.05$  respectively). Thus, because they had dropped below 95% of their original body weight, the animals in this group were given daily saline injections and protein rich food supplements for two weeks. Interestingly, there was a correlation between therapeutic outcome of irradiation and degree of weight loss. The two animals whose tumors were effectively treated by the 20 Gy had lost less weight by Day 5 (mean normalized body weights were 0.93 compared to 0.95 for the 5 vs. 20 Gy groups, respectively) and stopped losing weight three days sooner (Day 6 vs. Day 9 for the responders vs. non-responders, respectively). (Figure 5.11). The non-responder subset eventually started regaining their body weights on Day 9, and by Day 18, their mean weight was less than 1% different from their Day 0 body weight.

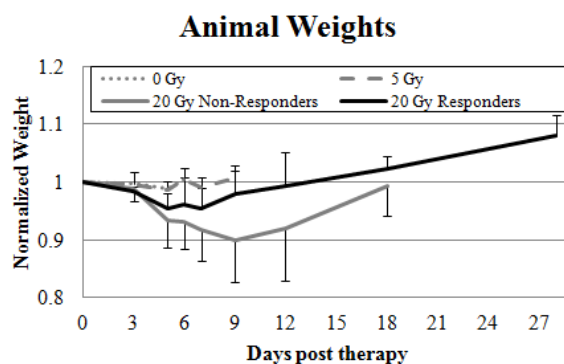


Figure 5.11: The animals weights for the different groups, normalized to each animal’s Day 0 weight.

The irradiation simulation experiment in Slicer revealed a potential mechanism for the weight loss observed in the 20 Gy group. Because the irradiations took place without image guidance, it is impossible to know the true location of the beam for all animals in the study, but based on the simulation data (Figure 5.12) it is likely that the beam irradiated the bladder, small bowel, and lower bowel in all animals, though it is unlikely that the kidneys were affected. Depending on the location of the tumors in the anatomical axial axis (“A-Ax” in Figure 5.12A) the proportions of both small and

lower bowel which were irradiated could have been modulated. This can be visualized in (Figure 5.12C). Based on the doses used in this study and the the delivery location, it is likely that the 20 Gy group's post-treatment weight loss was due to radiation-induced intestinal dysfunction (radiation enteritis). [126] This could be avoided in the future by positioning the tumor above the quadriceps muscle on the thigh at the time of implantation, as opposed to the flank area, as this would move the beam distally along the anatomical axial axis, and nearly eliminate the its overlap with both large and small bowels.

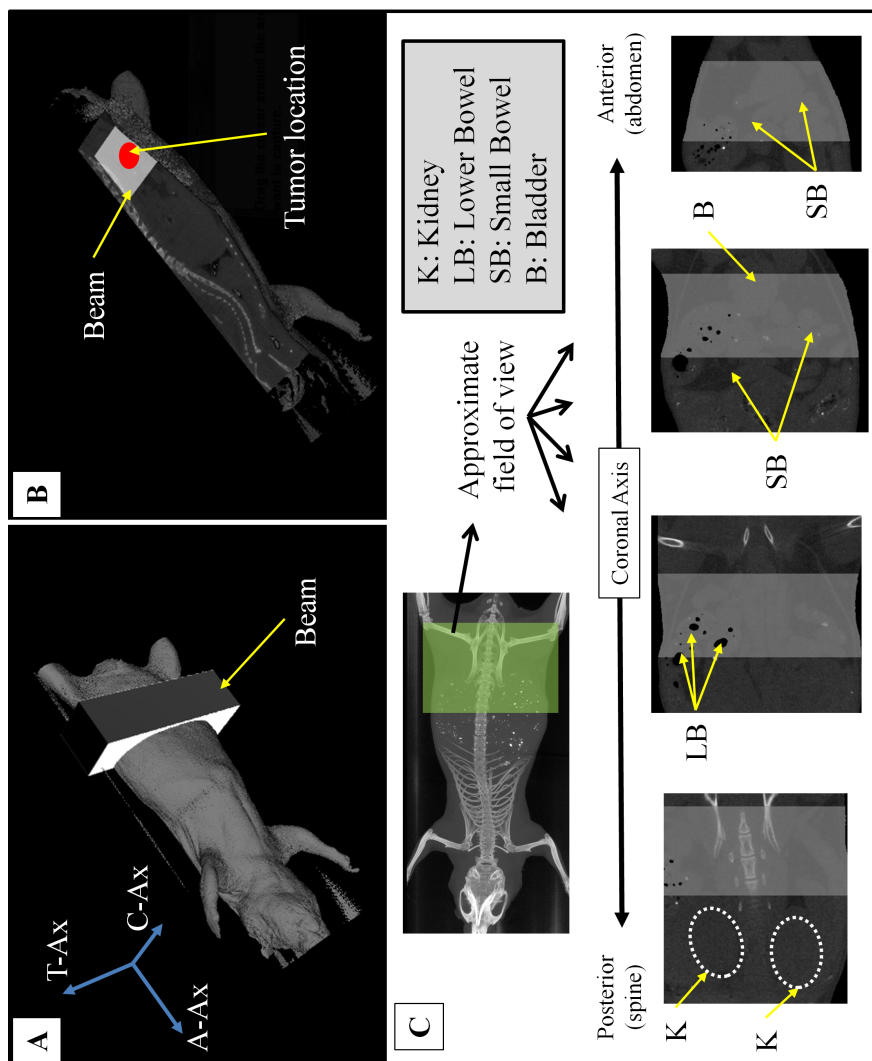


Figure 5.12: Results from the simulation study to predict which tissues would interact with the beam. A: a 3D rendered model and beam to illustrate spatial orientation. B: a clipped model fused to the 3D CT data to illustrate approximate tumor implant location and size at Day 0. C: Multiple coronal cuts through the data to sample different tissues as a function of depth into tissue.

## Assessing response to therapy (tumor volumes)

Irrespective of the treatment group, all tumors in the study continued to grow after treatment day, though there was a correlation between the irradiation dose and the degree to which tumors continued to grow after treatment. Tumors grew 2.63, 1.60, and 0.63 fold during the 3 days following irradiation for the 0 Gy, 5 Gy, and 20 Gy groups, respectively. There was not a significant difference between any of the 3 groups on Day 3 when comparing the distribution of tumor volumes, but when examining the distribution of tumor growth normalized to their Day 0 volumes, the 20 Gy group was significantly different than both the 0 Gy group ( $p = 0.004$ ) and the 5 Gy group ( $p = 0.002$ ). This difference in significance between the normalized and non-normalized data can be attributed to the heterogeneous size distributions of tumors at the Day 0 timepoint (Figure 5.9). The tumor volumes of the 20 Gy group remained well below those of the 5 Gy group for all subsequent timepoints. (Figure 5.13)

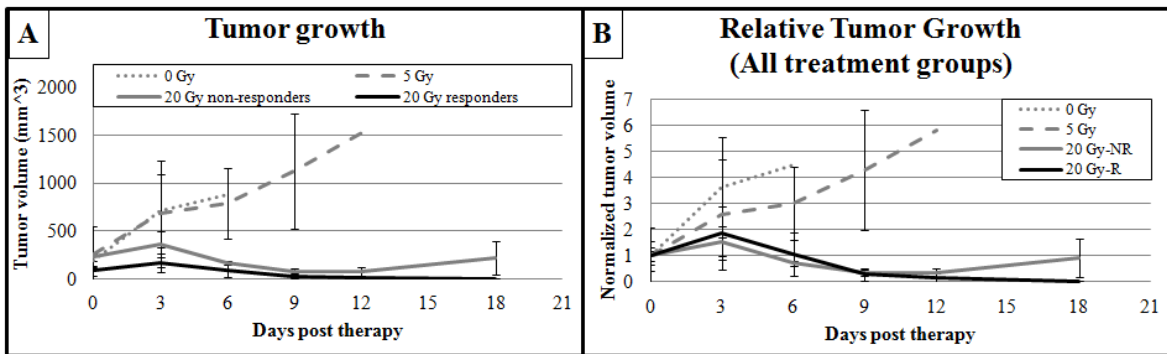


Figure 5.13: Plots showing the raw and normalized volumes of the tumor tissue vs. time (mean  $\pm$  standard deviation). Data are averaged over the group at each timepoint.

The tumor growth curve data for the 20 Gy group is difficult to visualize when plotted on the same scale as the rapidly growing 0 and 5 Gy treatment groups, thus they are plotted separately in (Figure 5.14).

On Day 18, the average responder subset normalized tumor volume was  $0.032 \pm 0.006$  (black) compared to tumor volumes of  $0.885 \pm 0.559$  in the non-responder subset (gray)

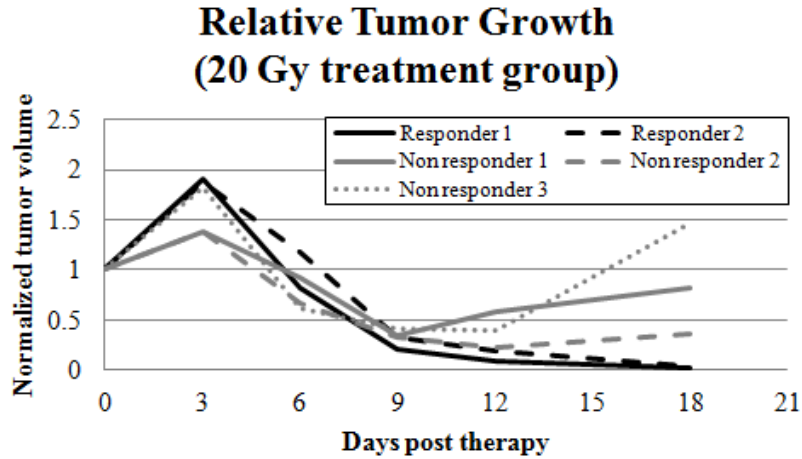


Figure 5.14: Plots showing the normalized volumes of tumor tissue vs. time for individual animals within the 20 Gy treatment group. The non-responders and responders are colored differently.

(Figure 5.14). After Day 18 there were no measurable tumors in the responder subset of the 20 Gy treatment group.

### Assessing response to therapy (tumor perfusion)

Immediately following radiation therapy, there did not appear to be any dramatic differences between the treatment groups when examining the interior perfusion of the tumors. This can be evaluated qualitatively (Figure 5.15) or via the quantitative analysis presented in (Figure 5.16). All groups experienced between a 1.20 and 3.02 fold increase in the volumetric perfusion ratio between days 0 and 3. While the responder subset had a 47.6% smaller perfusion ratio at the Day 3 timepoint than the non-responder subset ( $0.24 \pm 0.11$  vs.  $0.46 \pm 0.14$ ), this is unlikely evidence of this metric providing an early indication of eventual therapeutic response; on Day 6 and Day 9 that the two subsets of the 20 Gy group essentially have identical perfusion ratios (percent difference between them: 8.06%, and 8.75%; average percent standard deviation at these timepoints >15%), and thus the difference between them on Day 3 is likely just a coincidence.

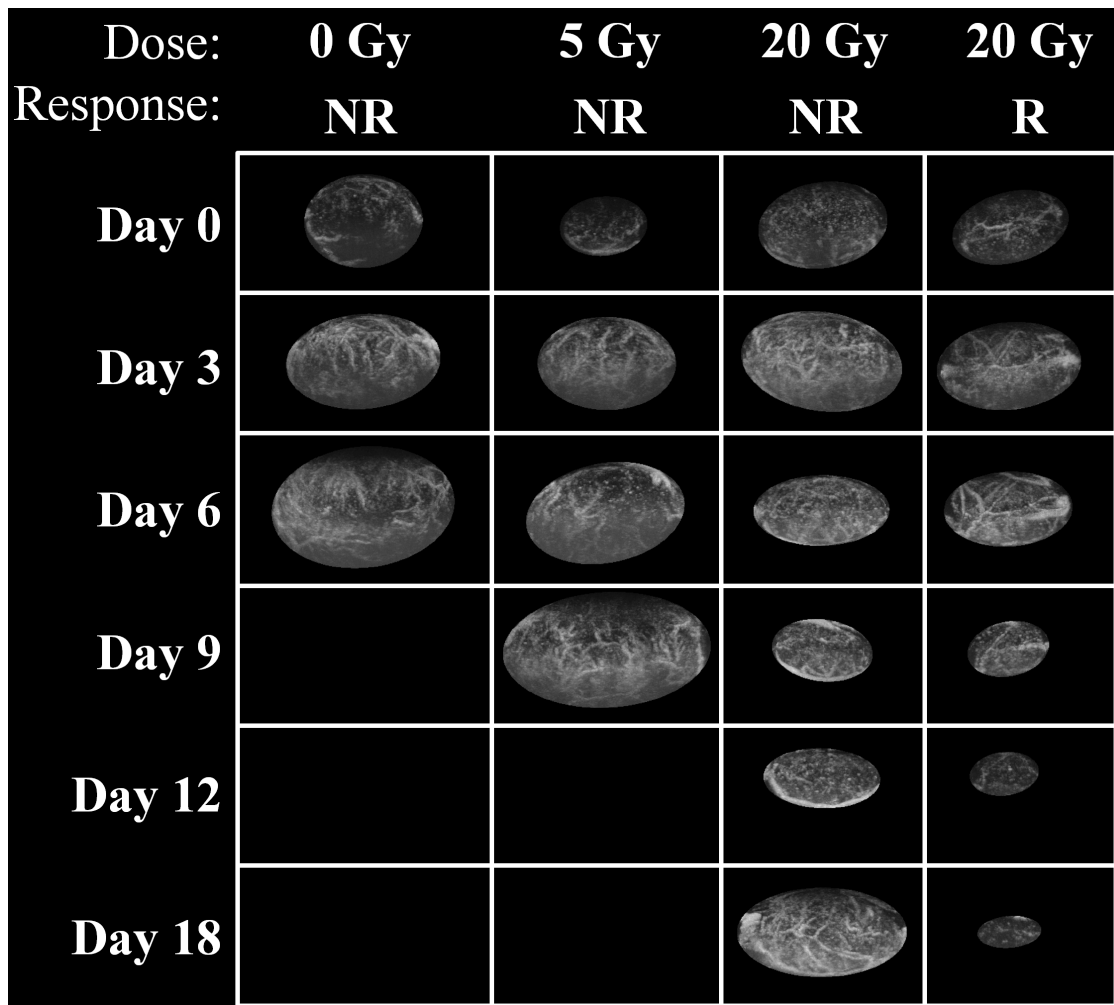


Figure 5.15: Representative samples of the image data analyzed in this study. These are maximum intensity projections through the elevational imaging axis (out of plane step direction of the transducer). Prior to the projections, the 3D image volume was first masked by the animal's 3D binary ROI at that timepoint. Thus, any vessel visualized in this image is contained within the boundaries of the tumor margins.



On Day 9, however, there is an inflection point in the perfusion ratio between the responder and non-responder subsets of the 20 Gy treatment group. After this timepoint, the responder subset's perfusion ratio falls linearly to zero, while the non-responder subset steadily increases back to over 50%. This is an interesting result, since there was a 0.7 fold difference between the volumes of these two subsets while the magnitude of the difference between the perfusion ratios was 1.1 fold. The total number of animals within the responder and non-responder subsets was small ( $N = 2$  and  $N = 3$ , respectively) so statistical comparisons between them do not carry much weight, but a trend is clearly evident in this metric, providing motivation for additional studies in the future to investigate the reliability of this quantity at predicting tumor response.

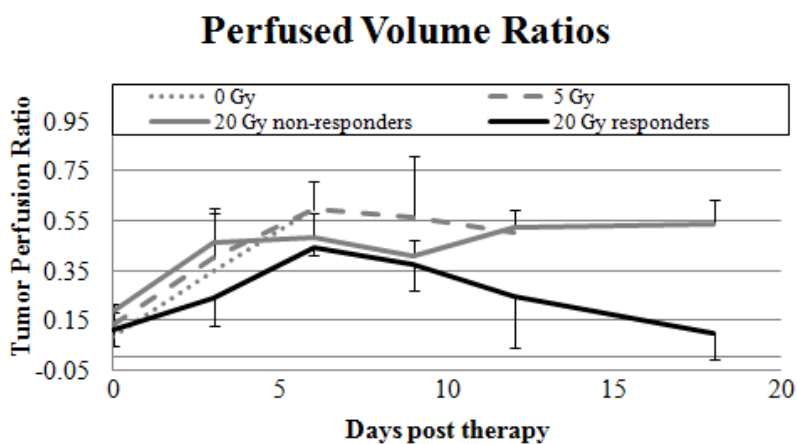


Figure 5.16: Plots showing the perfused volume ratio vs. time for the different groups (mean  $\pm$  standard deviation).

These results are remarkably similar to a previous study [119] most similar to our own, in which, following radiotherapy, power Doppler is implemented to estimate the ratio of perfusion within a single 2D slice through the treated tumors. As in this study, their tumor models were also located in the abdomen area, though were NMU induced breast tumors and thus were not the same model implemented in our study. This difference notwithstanding, they observed the same diverging treatment response

curves for animals treated by a high dose of radiation (18 Gy) after an initial decrease in tumor size. They also observed this difference in treatment response correlated with their index for blood perfusion. Their metric for blood perfusion could predict eventual tumor response at day 12 predicted eventual response. This is the same timepoint at which the perfused volume ratio also demonstrated a marked difference between the populations. Because we did not acquire power Doppler measurements in our own study, and because the sample sizes in the responder and non-responder subsets were so small, it is impossible to know which imaging method and corresponding metric for perfusion is more sensitive. This result does, however, provide motivation for additional studies to investigate the relationship and relative sensitivities between these modalities, especially since the VisualSonics system used for acoustic angiography has the capability to acquire power Doppler measurements.

#### **A note for future studies**

After the two subsets in the 20 Gy group diverged in their treatment responses on Day 9, it became difficult to estimate the statistical significance of the trend. Because repeating the study with additional animals was beyond the scope of this initial pilot study, additional studies will likely be performed in order to evaluate the diagnostic utility of acoustic angiography when used in this post-treatment tumor evaluation context. A standard power analysis using a 2-sided  $z$ -test with 0.05 significance level was performed and should be referenced in this case (Figure 5.17). It was based on the the means and standard deviations for the perfused volume ratio metric at the Day 12 timepoint (the first timepoint when the groups were qualitatively, if not measureably, distinct. The results of the power analysis indicate that at least 8 animals will be required in each group (non-responders and responders) to achieve 95% confidence at the  $\alpha = 0.05$  level.

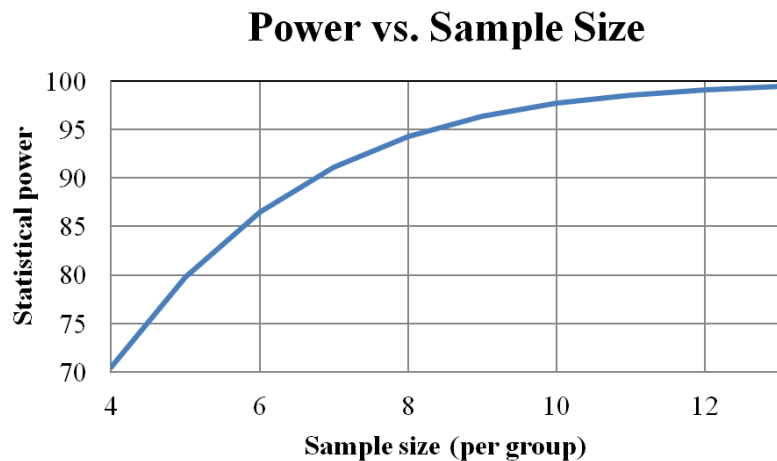


Figure 5.17: An analysis to estimate the number of animals required in each group to achieve the desired statistical power for delimiting responders from non-responders at the Day 12 timepoint.

### Limitations of the perfused volume ratio metric

There was a counterintuitive inflection point in perfusion volume ratio for the 5 Gy group after the Day 6 timepoint (Figure 5.16). As evidenced by their growth curves in Figure 5.13, these tumors are not undergoing any decrease or loss of malignancy. Rather, this is an unfortunate and unavoidable effect inherent to the computation of the perfused volume ratio metric when using our imaging equipment to image large tumors. The perfusion ratio relies on summing the number of pixels above the noise floor within the tumor boundary to quantify blood flow. This metric thus relies on signal intensities being stable throughout the imaging field in order to consistently and reliably account for the presence of blood vessels. Because the only transducer capable of imaging in acoustic angiography mode is a fixed-focus piston transducer, the sensitivity to vessels is non-uniform throughout the depth of field (Figure 4.5). This is not problematic for imaging vessels close to the acoustic focus in the axial dimension, but can result in underestimating perfusion in large tumors whose margins extend beyond the axial depth of field. In other words, our imaging approach will make a large tumor appear

as though it is not perfused with contrast in both the proximal and distal axial faces, whether or not there are blood vessels present at these locations. The reader is referred to the MIP of the Day 9 timepoint for the 5 Gy tumor in Figure 5.15 to illustrate this effect.

This is an inherent drawback for imaging large tumors with fixed focus piston transducers - a limitation which extends to power Doppler imaging on these preclinical systems as well - though a dynamically focused array transducer would be able to compensate for this effect by creating a more uniform sensitivity profile in the axial dimension. This notwithstanding, however, future users of the perfused volume metric extracted from any ultrasound image, 3D or otherwise, must take care to ensure consistent time-gain-compensation curves; users need to ensure consistent amplification of noise and signal levels originating from different regions in tissue, or across multiple timepoints, for this type of metric to have diagnostic meaning and value.

#### **5.2.4 Concluding remarks**

This study represents the first use of acoustic angiography to assess the inter-tumoral blood perfusion of post-irradiated tumors. The results demonstrated that the ratio of perfused volume to total tumor volume was correlated with tumor growth, and in fact was sooner to change within a subset of animals who were treated effectively by a 20 Gy radiation dose and those who were not treated effectively by this dose (i.e. their tumors reimmersed after shrinking). While it was beyond the scope of this study to elucidate the underlying biological mechanisms for why a subset treated at 20 Gy did not respond to the dose, it was likely a result of either their larger tumor sizes at the time of irradiation (statistically speaking, a greater number of radio-insensitive cells are present in a larger tumor), or the amount of healthy intestinal tissue which was irradiated (evidenced by subsequent weight loss in the non-responsive tumor bearing

animals) causing a heightened immune response within the gut.

Currently, the effects of radiation on tumor microvasculature is of interest to many. This imaging approach could provide a method to assess longitudinal perfusion in a high resolution way, though provided tumors fall within the size regime amenable to the current imaging probe's axial depth of field (tumor sizes from 1 mm to 1 cm), or until array technology is developed. The imaging studies performed herein were limited to structural information - tissue morphology from b-mode, vessel network architecture from acoustic angiography - though it is possible that additional functional information gleaned from other ultrasound imaging modes would improve diagnostic assessments of tumors responding to therapy; blood flow rates can be parametrically mapped via flash replenishment, and molecular signatures for disease can be detected via targeted contrast agents. While flow is likely related to vessel architecture, in the past it has been demonstrated that they provide independently useful information.

Previous acoustic angiography studies have used vessel morphological metrics to detect the presence of cancer. These differences between tissue types (healthy vs. malignant-tumor bearing) were immediately clear when looking at projections of the acoustic angiography data. While in this study, tumor vessel density was markedly different between the responder subset and the other groups, from a qualitative perspective, there did not appear to be the same morphological differences in vessel structure between any of the groups (0, 5, or 20 Gy). There have been several human magnetic resonance angiography tumor imaging studies published using the same vessel extraction and morphological analysis, which showed quantitative differences in vessel network architecture after successful tumor therapy, so it is possible that acoustic angiography could be used to extract diagnostic information (other than tumor size and perfusion ratio) from tumor-bearing tissue volumes in the future, though the current study parameters did not yield a promising model for testing this.

Finally, in this study all quantitative values extracted from the image data was limited to the boundaries of the tumor. The surrounding tissue was not assessed due to the limited field of view offered by the imaging technology currently available. As tumors get above 1 cm in diameter, they begin to dominate the field of view, occupying well over half the available imaging voxels, thus the ratio of tumor tissue to non-tumor tissue gets skewed as the lesions grow in size. This problem could be circumvented by a widefield imaging approach. Currently, our group is collaborating with an industry partner (Kitware, Carrboro NC) to enable the expansion of preclinical imaging into a wider field of view, and software is already available in their open source Slicer platform to enable to registration of multiple sub-volumes.

## CHAPTER 6

### RADIATION FORCE ENHANCED MOLECULAR IMAGING

Both of the studies presented in this chapter implemented acoustic radiation force as a method to increase the number of contrast agents retained by diseased tissues in molecular imaging studies. For the first study, radiation force was implemented on the dual-frequency transducer (Chapter 6.1) Despite some initially promising results from this study, there were some unfortunate tradeoffs to using the dual-frequency probe in this type of molecular imaging study (discussed in Chapter 6.1.4), so our group pivoted to a widely available clinical ultrasound system as a method to both administer radiation force and image targeted contrast agents (Chapter 6.2).

Since early observations of acoustic radiation force (ARF) on microbubble contrast agents, researchers have speculated about the utility of this force to push populations of microbubbles in a direction normal to their flow in a patient's vasculature, thereby guiding them out of circulation and against the wall of a vessel [61]. It has been hypothesized that increasing ligand-receptor proximity and reducing the velocity of

---

*Note:* This chapter has two sections, both of which draw from previous published material. Previously published material was reprinted with permission from the publishers.

**Chapter 6.1:** Ryan Gessner, Marc Lukacs, Mike Lee, James Tsuruta, F.Stuart Foster, Paul A. Dayton. *Radiation force-enhanced targeted imaging and near real-time molecular imaging using a dual-frequency high-resolution transducer: in vitro and in-vivo results.* IEEE International Ultrasonics Symposium Proceedings. 2009

**Chapter 6.2:** Ryan C. Gessner, Jason Streeter, Roshni Kothadia, Steven Feingold, Paul A. Dayton. *An In Vivo Validation of the Application of Acoustic Radiation Force to Enhance the Diagnostic Utility of Molecular Imaging Using 3D Ultrasound,* Ultrasound Med Biol, 2012 Apr;38(4):651-60.

flowing microbubbles would greatly increase the amount of targeted microbubble adhesion in molecular imaging studies [62; 127; 70; 69; 128]. *In vitro* studies of ARF on microbubbles have demonstrated the ability to increase the quantity of microbubble adhesion more than 100-fold compared with molecular targeting without ARF [127]. *In vivo* observations performed by intravital microscopy have also demonstrated between four and 20-fold increases (depending on the vascular environment) in the amount of targeted microbubbles retained in microvasculature after ARF pulses [70]. Similarly, with the development of acoustically active drug delivery vehicles, it has been hypothesized that ARF could be a mechanism to increase vehicle and drug concentration at the desired target site via ultrasound. Researchers have shown the utility of ARF to mediate the concentration of several types of potential therapeutic delivery vehicles [67; 68; 129].

It has also been proposed that ARF might play a role in pulse sequences designed to enhance the detection of targeted contrast agents in molecular imaging. Many current molecular imaging studies involve the use of a waiting period, typically 5-20 minutes, for free (unbound) microbubbles to clear the circulation before imaging of adherent targeted agents can be performed [59]. This limitation makes molecular imaging with ultrasound a slow process and likely results in loss of detected signal, because bound microbubbles can detach or degrade over the waiting period. It has been shown that rapid increase in adhesion of targeted microbubbles using ARF can be used to help delineate signal from free and bound contrast agents [130; 131].

However, to date, literature demonstrating the application of ARF *in vivo* to improve microbubble targeting has been scarce. This is likely caused by a disparity between the types of acoustic pulses used for imaging by clinical and preclinical imaging systems, and the acoustic regime over which ARF-induced microbubble displacement



is most efficient. Microbubble translation is maximized near the bubble’s resonant frequency. For most efficient translation, a large duty cycle is required, and the mechanical index must be low enough to avoid microbubble destruction [62]. A long duty cycle and low mechanical index are typically not parameters beneficial for ultrasound imaging, and thus it is likely that the paucity of *in vivo* ARF-enhanced molecular imaging data is a result of these pulse sequences not being intuitively available on commercial ultrasound equipment.

## 6.1 Molecular imaging with the dual-frequency prototype

### 6.1.1 Methods

#### *In vitro* experiments

To test the dual-frequency probe’s proficiency at facilitating microbubble targeting via radiation force, two *in vitro* setups were implemented. Microbubble-target binding was achieved *in vitro* via the avidin-biotin binding complex, using the *in vitro* targeted agent formulation (Appendix A). Two flow phantoms were used: an optical phantom and an acoustic phantom. The optical phantom was a 200  $\mu\text{m}$  cellulose tube used to optically verify the production of radiation force and radiation force enhanced targeting. The acoustic phantom was a wall-less agarose gel phantom in which radiation force enhanced targeting was verified acoustically. A syringe pump was used at several different constant volumetric flow rates to pump microbubbles (diluted to  $\sim 5 \times 10^6$  bubbles/mL) through the phantoms. The waveforms used for administering radiation force were 200-cycle 4 MHz sinusoids with a PRF of 15 kHz and peak negative pressures of approximately 100 kPa. Even though this frequency was outside of the optimal bandwidth of the low frequency element, it was chosen to reduce bubble destruction.

#### 1) Optical phantom setup

The cellulose tube filled with avidin for 1 hour and then flushed with deionized

water after this time had passed. The tube was oriented horizontally at the focus of both the dual-frequency probe and a Photron high-speed camera (Model APX-RS - San Diego, CA) equipped with a 60x water immersion lens (Olympus LUMPlanFI/w - Melville, NY). The axes of the transducer and the camera were aligned perpendicularly with the tube at the same location. A needle hydrophone was positioned in the optical focus and the pulsing transducer was aligned to maximize the measured signal from the hydrophone. Radiation force pulses were applied to the microbubble solution as it was pumped through the tube at different flow rates. The efficacy of the radiation force pulses to divert the flow of contrast agents and enhance targeting was observed in real time as well as recorded for offline confirmation.

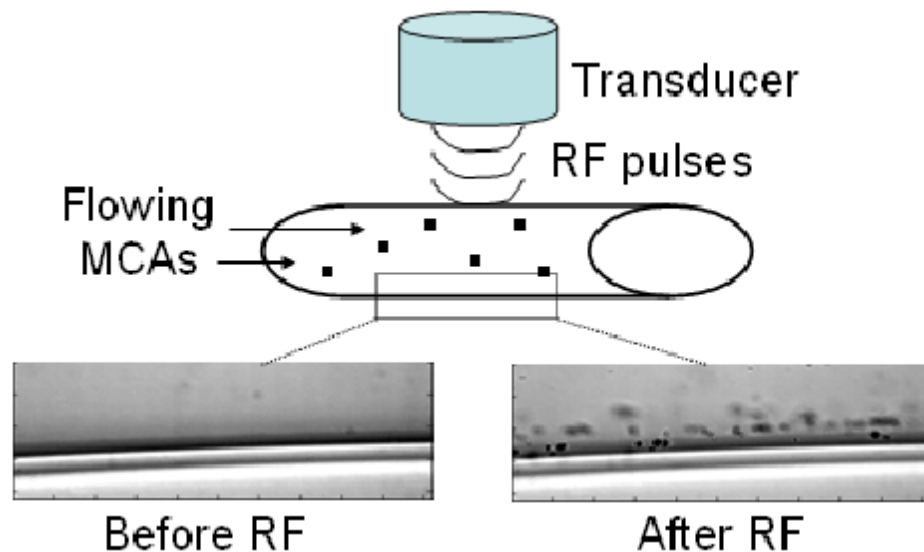


Figure 6.1: An image displaying adherent bubbles successfully targeted to the wall of the 200  $\mu\text{m}$  cellulose tube by a single sweep of the dual-frequency transducer despite the constant shear stress induced by the volumetric injection rate of 5 mL/h.

## 2) Acoustic phantom setup

The biotinylated wall-less flow phantom was prepared as described by Needles et al. using agarose at a concentration of 10 mg/mL [132]. The bore was created by suspending a polyethylene tube (outside diameter: 1.09 mm) between the inlet and

outlet needles and then removed after the gel had cooled. The bore was avidinated the same way as the cellulose tube. The syringe pump was used to flow microbubbles through the bore at a constant volumetric flow rate of 1 mL/h at a horizontal orientation. The dual-frequency transducer was vertically aligned with the tube and coupled with the phantom surface using ultrasound gel. Radiation force pulses were applied and then bound and free bubbles were imaged. Bound bubbles were delineated from freely circulating bubbles in the video data using interframe averaging filtering [131; 132].

### ***In vivo* experiments**

A fibrosarcoma tumor model was imaged to examine the effects of radiation force on targeted bubbles circulating *in vivo*. The tumor was implanted on the right hind leg as previously described [133] and allowed to grow to a diameter of  $\sim 1$  cm. Targeted microbubbles were administered in 200  $\mu\text{L}$  bolus injections via a 24 gauge tail vein catheter. During the radiation force-enhanced studies, the transducer would sweep at 1 Hz over the center of the tumor as the microbubbles were administered both during the injection and for 30 s following the injection. During passive targeting studies, radiation force pulses were not administered. After waiting 25 min to allow for freely circulating bubbles to clear from the animal, a 3D scan was acquired across the volume of the tumor at step sizes of 200  $\mu\text{m}$ .

## **6.1.2 Results**

### ***In vitro* experiments**

Biotinylated microbubbles were successfully targeted to avidinated phantom walls and verified both optically and acoustically in the two different setups. In the optical phantom, radiation force pulses were administered to microbubbles flowing at linear flow velocities between 0.3 and 200 mm/s. The pulses were able to push bubbles to the bottom wall of the tube, against buoyancy, at all linear flow velocities less than

50 mm/s. At flow rates faster than this the direction of the microbubble stream was perturbed, though did not significantly divert within the viewing window of 500  $\mu\text{m}$ . At flow rates faster than 25 mm/s, bubbles could successfully be pushed to the wall, though the shear stress tended to dislodge targeted bubbles in the phantom tube model rapidly. In the gel phantom, microbubbles were successfully targeted to the wall of the phantom. Because the tissue signal in dualfrequency imaging was suppressed, it was possible to delineate bound bubbles from freely flowing bubbles using interframe filtering. Movie files were exported to Matlab and a 10 frame moving average filter was applied prior to a thresholding operation. The resulting signal was overlaid on top of dual-frequency b-mode data and color coded in green. An example of this can be seen in Figure 6.2C.

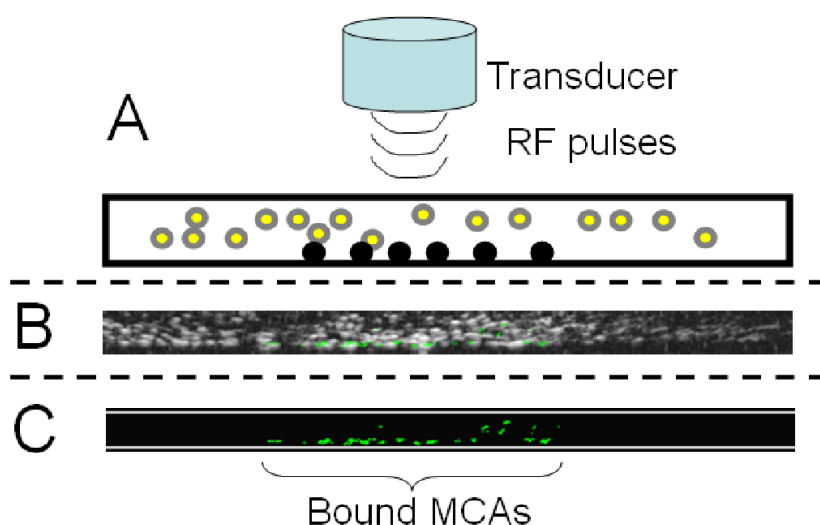


Figure 6.2: A: A schematic cartoon showing the position of the transducer in relation to the wall-less flow phantom. Incident RF pulses forced freely flowing bubbles (two colors) against their buoyancy to become bound (black colored). B: A dual-frequency b-mode image free and bound contrast agents within the phantom. Overlaid on top of this image in green is the signal of adherent microbubbles delineated from moving bubbles using interframe filtering. C: Only the signal returned by the filtering process showing bound microbubbles delineated from freely flowing ones.

### *In vivo* experiments

Microbubbles targeted to angiogenic vasculature were used to compare radiation force enhanced targeting with conventional passive targeting. Four injections of targeted contrast agents were administered to an animal with the same 2D planes within the 3D datasets examined between the different data collections throughout the study. Radiation force targeted and control studies were alternated. The two studies implementing radiation force pulses during the administration of the microbubbles showed improved microbubble retention in every 2D image slice of data collected when compared to the passive targeting studies, as evidenced by Figure 6.3.

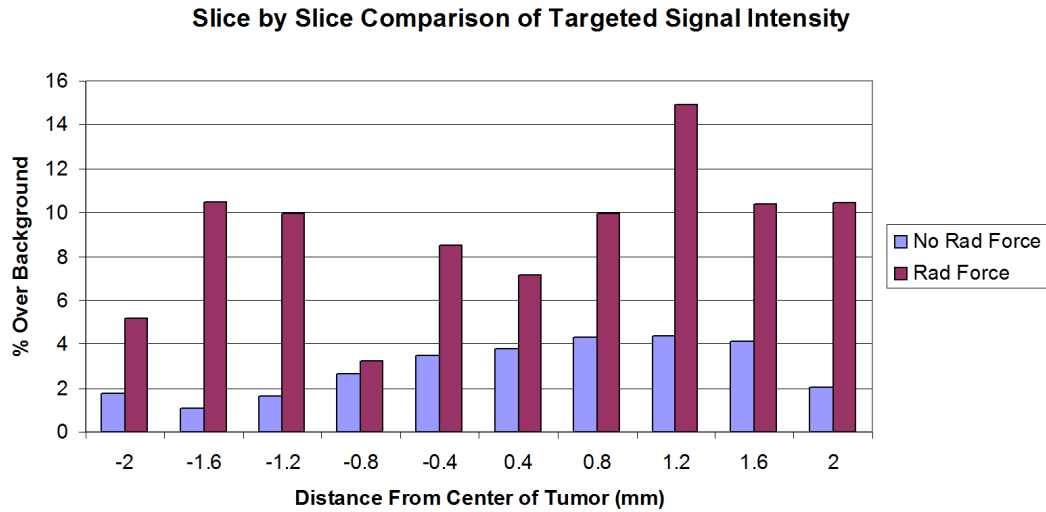


Figure 6.3: Comparison of molecular targeted bubble signal as a function of distance through the tumor.

The average improvement in mean pixel intensity within the same image slices of the tumor between passive and radiation force-enhanced datasets was 13.3 dB ( $N = 12$ ). The maximum improvement in targeting intensity as a result of using radiation force was 35.1 dB, while the minimum was 2.1 dB. The average mean pixel intensity increase over baseline was  $2.5 \pm 2.4\%$  and  $8.4 \pm 4.4\%$  for passive and radiation-force enhanced studies respectively (error is standard deviation). There was no significant decrease in

targeting performance between the first and second trials of either the passive or radiation force-enhanced studies, indicating that there was very little reduction in available targeting sites due to previous studies' adherent bubbles.

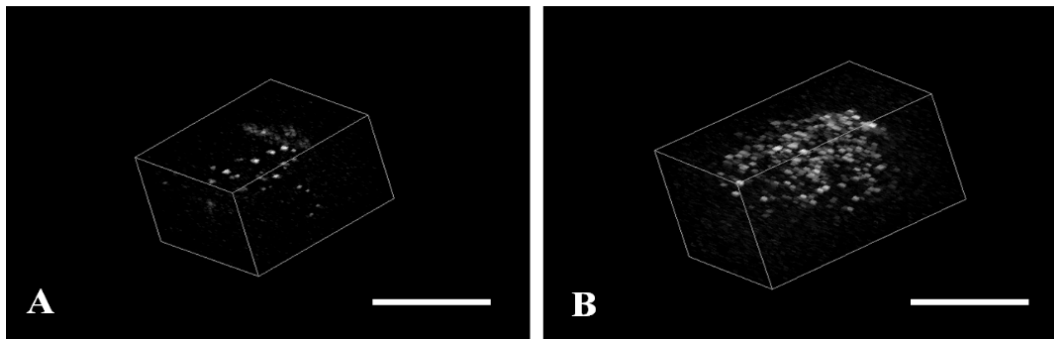


Figure 6.4: Two images comparing the targeted contrast agent intensity in multiple 2D slices between passive targeting (A) and radiation force-enhanced targeting (B) studies. Scale bars = 1 cm.

### 6.1.3 Discussion

#### *In vitro* experiments

*In vitro* experiments demonstrated the effectiveness of a dual-frequency probe in the ability to enhance adhesion of targeted microbubbles using the low-frequency element. Application of 4 MHz ultrasound at  $\sim 100$  kPa and a 75% duty cycle, swept at 1 Hz across the sample volume, significantly increased the retention of targeted microbubbles along the distal wall of a tube phantom. Contrast-specific imaging, achieved by exciting microbubbles at 2.5 MHz and receiving broadband harmonic energy above 10 MHz, was shown to suppress tissue signal and allow imaging of only bound and free contrast agents. Successive slow-time filtering, performed by averaging video frames, enabled filtering of free-floating microbubble signal and detection of bound targeted agents. Signal from bound agents was color-coded in green and could be overlaid on either tissue or contrast data in order to perform near real-time targeted imaging without the requirement of a waiting period for signal from unbound contrast to clear.

## ***In vivo* experiments**

*In vivo* application of radiation force during targeted imaging studies was demonstrated to significantly increase the amount of targeted contrast agent retained in the vasculature. An average of 13 dB in signal enhancement was achieved compared to non-radiation force enhanced targeting. This demonstrates the utility of radiation force to enhance targeted microbubble retention *in vivo*, as is desired in molecular imaging or microbubble-based therapeutic strategies.

### **6.1.4 Concluding remarks**

In this preliminary study, the effects of acoustic radiation force produced by the generation 1 dual-frequency probe's low frequency element were observed in two *in vitro* phantom models and an *in vivo* tumor model. As was determined in a different study, acoustic angiography cannot be performed without clearing microbubbles from the imaging plane (Chapter 3.1). This represents a critical barrier for acoustic angiography's implementation in molecular imaging studies. Non-destructive contrast imaging is important, as the amount of time required for freely flowing non-targeted contrast agents to clear from the blood stream can vary, and being able to assess the degree to which bubbles have cleared the system is an important first step prior to acquiring image data; if freely flowing bubbles are present, then the user can wait long for them to clear prior to acquiring data, but if a microbubble-clearing imaging approach is used then this preliminary step is impossible.

While the dual-frequency probe's design made it very flexible with respect to the pulsing schemes used to administer radiation force, the fact that it could not non-destructively image contrast agents forced us to implement a different imaging system to test the hypothesis that radiation force was a method to enhance molecular imaging studies. This followup study is presented in the following section.

## 6.2 Volumetric molecular imaging with a clinical system

In this chapter, we describe the implementation of a widely used clinical ultrasound system, the imaging parameters of which we have adjusted to produce ARF of a magnitude substantial enough to cause nondestructive bubble translation. After the ARF pulses used to enhance contrast targeting, we use contrast-specific imaging pulse sequences for molecular imaging. This study uses a fibrosarcoma tumor model to illustrate the effect of ARF-enhanced molecular imaging compared with conventional passive molecular imaging. In addition, we investigate the effect on nonspecific adhesion caused by the intentional push of microbubbles away from the center of the lumen toward the distal walls within tumor vasculature. Results from preliminary *in vitro* studies are also presented that suggest that the pressure of the ARF pulse sequence is a significant factor in promoting lasting bond kinetics between molecularly targeted microbubbles and their target integrins, and that one must balance detrimental over-pushing with ineffective under-pushing to achieve the optimal ARF-enhanced molecular imaging protocol.

### 6.2.1 Materials and methods

#### Imaging

All microbubbles imaged in our studies were formulated in-house as previously described [54]. The two lipid formulations used were the *in vivo* targeted formulation and the perfusion agent formulation (Appendix A). Both targeted and nontargeted bubbles were of a diameter size distribution centered at 1.6  $\mu\text{m}$ . This was achieved through a differential centrifugation technique [134]. Imaging was performed on a Siemens clinical ultrasound system (Acuson Sequoia 512; Siemens Medical Solutions, Mountain View, CA, USA) using a linear array transducer (model 15L8). The transducer was precisely positioned using a three-axis translational motion stage setup, as previously described [135], and the same probe was used for both imaging and the application



of ARF. For volumetric radiation force administration and imaging, the transducer was swept in the elevational direction by a computer-controlled motion stage (Model UTS150PP; Newport, Irvine, CA, USA) interfaced through LabView (National Instruments, Austin, TX, USA) to a desktop computer. This motion stage allowed 3D images to be captured and ARF pulses to be delivered uniformly across the volume. ARF pulses were optimized in the pulsed wave (PW) Doppler mode at a frequency of 7 MHz. Adjusting the gate size (18 mm), location of the gate within the field (65 mm), and blood velocity scale (1 m/sec) enabled us to achieve a 25% duty cycle pulse with a PRF of 25 kHz (70 cycles). The amplitude of the ARF pulses was modulated by using the power output dial of the ultrasound system (range -7 dB to 0 dB).

### **Calibration**

Acoustic pressure measurements were determined by a calibrated needle hydrophone (model HNA-0400; Onda, Sunnyvale, CA, USA) in a water tank. The acoustic pressures produced by the linear array transducer in PW Doppler mode at the previously mentioned parameters were measured at 100  $\mu\text{m}$  increments in a 2.2x0.4-cm area in front of, and parallel to, the aperture using the needle hydrophone. This region of the acoustic pressure field was mapped at 0.5-, 1-, 1.5-, and 2-cm distances from the aperture, for seven different power output settings. The peak negative pressure was measured at each spatial location and power output setting. These pressures were between 8 and 28 kPa for the system output setting studied, and the pressure field deviated by <10% at the locations between 0.5 and 2 cm from the aperture face (in the water tank).

### ***In vitro* studies: effect of ARF pressure**

To assess the relationship between output pressure and microbubble translation efficiency, an optical-acoustical system was constructed to enable visualization of microbubble translation during pulsing. A Photron high-speed camera (Model APX-RS; San Diego, CA, USA) was fitted with a 60x water immersion objective lens (LUM-PlanFI/w; Olympus, Melville, NY, USA) through a single-tube microscope (Edmund Optics, Barrington, NJ, USA). The objective was inserted through a latex seal into the water tank and aligned confocally with and at 90 degrees to the linear array transducer (Figure 6.5A). A 200  $\mu\text{m}$  acoustically and optically transparent cellulose tube (Spectrum Labs, Rancho Dominguez, CA, USA) was placed at the mutual focus, and a fiber optic illuminator was used as a light source for the camera. A dilute concentration of contrast agents ( $2 \times 10^7$  bubbles/mL; approximately 1:1000 from the initial concentration) was pumped through the tube and ARF pulses were applied perpendicularly to both the flow direction and microbubble buoyancy. Videos were acquired of the contrast agents as they were pushed by the ARF pulses across the diameter of the tube. Data were analyzed offline and the spatial locations of the contrast agents were mapped throughout their translation using a custom-designed program in Matlab (The MathWorks, Natick, MA, USA). Bubble motion was tracked at each of the pressure outputs, yielding a relationship between ARF-induced translational bubble velocity and acoustic pressure amplitude.

A second study was performed in which the axial dimension of the transducer was aligned with the optical axis, and ARF pulses were used to push contrast agents toward the wall of the tube closest to the lens (Figure 6.5B). The purpose of this study was to visualize the behavior of microbubbles at the tube wall after initial ARF pulses had successfully pushed them to the boundary and thereby quantify conditions in which

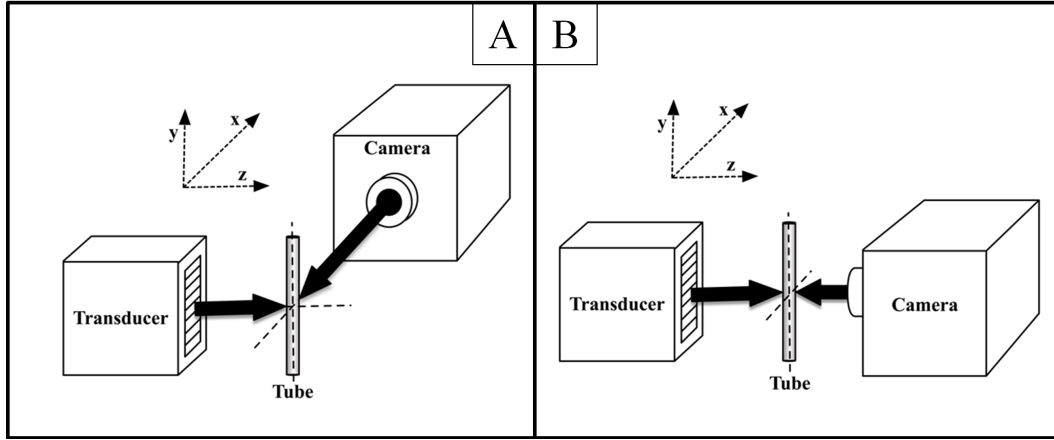


Figure 6.5: Experimental diagrams for the *in vitro* characterization of the effects of radiation force on microbubbles. (A) System used to determine the relationship between microbubble translational velocity and output pressure from the transducer. (B) System used to examine the effects of secondary radiation force on contrast agents after making contact with the tube wall. In (A) the optical axis is along the x direction, the acoustic axis is along the z direction and the microbubble flow axis is along the y direction. Similarly, in (B), the optical axis and the acoustic axis are along the z direction and the microbubble flow axis is along the y direction.

“over-pushing” occurred. We define over-pushing as any ARF setting that caused microbubble destruction, or lateral microbubble translation along the tube wall. At higher acoustic pressures, lateral motion caused by both secondary radiation forces and force vectors along the curved tube surface in response to primary radiation force would likely cause adherent microbubbles *in vivo* to be knocked free. Thus, too much radiation force could be detrimental to molecular imaging studies. Videos of the bubbles were acquired for several seconds as they were pushed into the wall by ARF pulses, and analyzed later offline. Data were processed with a pixelwise standard deviation projection through the time axis, thereby enabling the visualization of any lateral movement of bubbles after they initially reached the tube wall.

### ***In vitro* studies: Estimating optimal *in vivo* study parameters**

It is known that the amount of ARF experienced by a defined population of microbubbles is a function of the acoustic pressure and the exposure time in the acoustic field.

Before *in vivo* studies, we estimated optimal experimental parameters for administering ARF to a volume of tissue in which targeted contrast agents were circulating. We chose to use a fixed translational speed of  $1 \text{ mm s}^{-1}$  for the mechanically scanned transducer, as well as a fixed duty cycle for all ARF administration. The optimal pressure,  $P_o$ , was necessarily a balance between efficient bubble translation and bubble-wall interactions. Our goal was to design an experimental protocol in which ARF was applied uniformly across a volume of tissue. Because of the effects of tissue attenuation,  $P_o$  was not constant through the entire depth of tissue. This necessitated a compromise between over-pushing in shallower regions of tissue and under-pushing at deeper regions of tissue. The optimal initial ARF pressure to maximize targeting efficiency through a specific tumor size was estimated by taking the minimum value of a cumulative error-function (CEF) defined as

$$CEF = \int_0^D | P_o - P(z) | dz \quad (6.1)$$

where  $P(z)$  was the pressure of the radiation force beam derated for attenuation at depth  $z$  into the tumor with an axial diameter  $D$ . Compensation for tissue attenuation is achieved via the formula

$$P(z) = P_i e^{-\alpha z} \quad (6.2)$$

where  $\alpha$  is the attenuation coefficient for the tissue [136]. A constant tissue attenuation of  $0.6 \frac{Np}{cm}$  was assumed for the tumors used in the *in vivo* portion of the study, because this falls within the range of attenuation values previously measured [137; 138]. The units of this CEF are measured in kPa, although the true values returned by the equation are less important than the relative values between different power output settings. We computed the CEF for each of the output settings on the

ultrasound system as a method for estimating the optimal ARF pressure amplitude for a given tumor diameter. Similarly, we could estimate the axial distance travelled by microbubbles,  $D_a$ , within a volume of tissue as a result of the ARF pulses by computing

$$D_a(z) = (\text{velocity}) \cdot (\text{time}) = (m \cdot P(z)) \cdot \left(\frac{w_b}{v_T}\right) \quad (6.3)$$

where  $m$  is the slope of the curve for velocity of microbubbles as a function of pressure (determined by the *in vitro* experiments with the schematic seen in Figure 6.5A, with units  $\text{m}(\text{s kPa})^{-1}$ ),  $P(z)$  is the pressure of the ARF beam at depth  $z$ ,  $w_b$  is the elevational width of the ARF beam (3 mm) and  $v_T$  is the elevational sweep velocity of the transducer during the application of ARF. Thus, the first term in parentheses will yield the average velocity of the microbubbles exposed to ARF, and the second term will yield the amount of time they are travelling. This calculation assumed an infinite potential path length (i.e., no tube wall to prevent the bubble from being steadily translated).

### ***In vivo* experiments**

Fischer 344 rats (Charles River Laboratories, Durham, NC, USA) were used for studies of ARF-enhanced and conventional molecular imaging (hereafter called passive targeting studies, i.e., those not using ARF). All animal studies were conducted in accordance with protocols approved by the University of North Carolina School of Medicine's Institutional Animal Care and Use Committee.

Fibrosarcoma tumor models ( $N = 8$ ) were established from propagated tumor tissue courtesy of the Dewhirst Lab at Duke University. Before implantation, rats were anesthetized using isoflurane and their left flank was shaved and disinfected. A 2-mm incision was made above the quadriceps muscle and a  $\sim 1 \text{ mm}^3$  piece of tumor tissue was placed subcutaneously. Imaging was performed on tumors after their longest axis

had grown to approximately 1 cm.

During the molecular imaging studies, animals were anesthetized with 2.5% inhaled isoflurane anesthesia mixed with oxygen, and their body temperature was maintained at 37C through the use of a temperature-controlled heating pad. The area to be imaged was shaved, further depilated using a chemical hair remover, and then coupled to the ultrasound transducer using gel as previously described [135].

Microbubbles were administered in bolus injections via a 24-gauge tail-vein catheter. The concentrations of stock solutions for both the targeted and control bubbles were measured before each imaging study using a particle sizer as previously described [54]. The appropriate volume of stock solution was added to the catheter via a micropipette tip and flushed with 100  $\mu$ L of sterile saline such that a contrast dose of  $2 \times 10^8$  bubbles was administered consistently. Because of the dose limitations with the injected volume of saline and contrast into the animals, two different types of studies were performed over several days to examine (a) the effect of ARF pulse amplitude on microbubble targeting efficiency relative to passive targeting, and (b) the effect of ARF at promoting nonspecific adhesion in control bubbles relative to targeted bubbles also exposed to ARF.

For study type (a), each animal underwent four distinct injection and ARF protocols in the following order: (i) Passive targeting (no application of ARF) using targeted microbubbles; (ii) application of ARF with a pressure of 4 kPa using targeted microbubbles; (iii) application of ARF using a pressure of 13 kPa with targeted microbubbles; and (iv) application of ARF with a pressure of 21 kPa using targeted microbubbles. After each of these four imaging protocols, there was a minimum wait time of 10 min to ensure that there were no circulating microbubbles remaining. Similarly for study type (b), each animal underwent distinct injection and ARF protocols in the following order: (i) Passive targeting with control microbubbles, (ii) application of ARF with

a pressure of 13 kPa with control microbubbles, (iii) passive targeting with targeted microbubbles and (iv) application of ARF with a pressure of 13 kPa with targeted microbubbles. Between each type (b) experiment, there was a minimum wait time of 10 min to ensure that there were no circulating microbubbles remaining in the tumor vasculature. Because of injection volume limitations, study types (a) and (b) were not performed in the same animal on the same day. To compare type (a) and type (b) experiments, data were normalized to the mean image intensity within the volumetric passive targeting image data (using targeted microbubbles without application of ARF) in each animal because this imaging protocol occurred in both type (a) and type (b) studies.

During all ARF-enhanced targeting studies, radiation force pulses were applied over the entire volume of the tumor using the mechanically scanned transducer at pressures of 4, 13 or 21 kPa (number of animals imaged at each setting: 4 kPa,  $N = 5$ ; 13 kPa,  $N = 7$ ; 21 kPa,  $N = 5$ ). The transducer was swept at a constant speed of 1 mm/s across the tumor volume after contrast agents were administered to the animal, for a total of 10 passes after the injection. During passive targeting studies, ARF pulses were not administered ( $N = 4$ ). After waiting approximately 10 min for freely-circulating bubbles to clear from the animal's system, a 3D imaging scan was acquired across the tumor with interplane step sizes of 400  $\mu\text{m}$  in the ultrasound system's Cadence contrast imaging mode (CPS). The bound microbubbles were then destroyed using a high mechanical index b-mode 3D scan, and then the tumor reimaged in CPS mode at the same slice locations for a baseline measurement of no targeted agents.

Our interimage step-size was below the -6 dB elevational beam width determined in a previous study [31] to be  $\sim 800 \mu\text{m}$ . Thus the volumetric data were down-sampled offline at 800  $\mu\text{m}$  intervals to yield independent imaging frames for analysis as previously described [54]. The mean pixel intensities within the background-subtracted

images were computed, producing a mean targeted bubble intensity for every 2D image plane within the 3D image acquisition. As previously mentioned, the mean targeted microbubble intensity values were normalized to the mean of the passive targeting microbubble injection. This allowed us to reduce the impact of interanimal tumor heterogeneity when making comparisons between animals. The brightness of adherent microbubble contrast agents was assumed to be correlated with the degree of biomarker expression. Thus, throughout the remainder of this manuscript, mean pixel intensity will refer to the quantity defined by the difference between the average image's intensity before the destruction pulse and the average intensity of the image for the same region of interest after the destruction pulse. This mean pixel intensity metric is a way to approximate the quantity of adherent microbubbles at a single 2D image slice's location. The statistical significance of our comparisons between the mean microbubble targeting measured by the different imaging study settings was assessed using Matlab to implement a two-sided Student's t-test assuming equal variances. Significance between two different distributions was considered at a value of  $p < 0.05$ .

## 6.2.2 Results

### *In vitro* studies: effect of ARF pressure

The positions of multiple bubbles ( $4 < N < 10$ ) were tracked through space and time and a linear relationship ( $R^2 = 0.953$ ) between velocity and radiation force amplitude was observed, with a slope of  $5.018 \text{ m} \cdot [\text{s kPa}]^{-1}$  (Figure 6.6A). For this linear curve fit, the y-intercept was set to 0 (corresponding with a velocity of zero for microbubbles not exposed to ARF).

At each acoustic pressure setting tested between 8 and 28 kPa, the ARF pulses were able to force the microbubbles out of the center of the cellulose tube and against the wall. As the pressure was increased, the aggressiveness of the lateral bubble movement



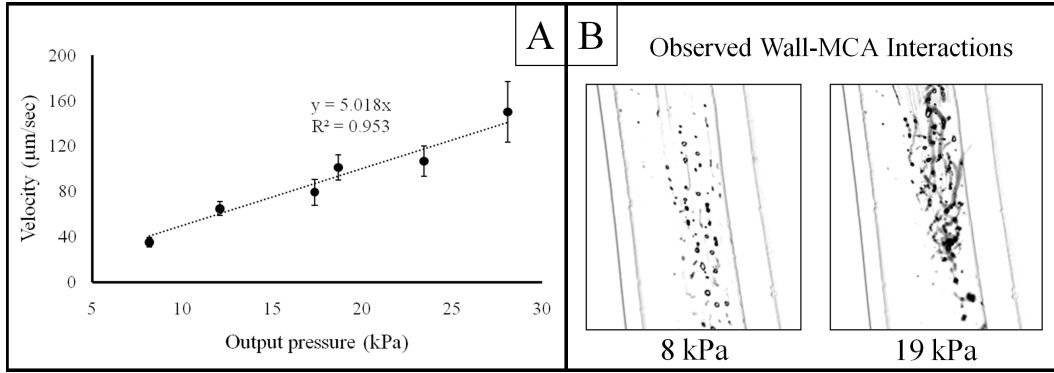


Figure 6.6: Results from optical observations of *in vitro* radiation force on microbubbles. (A) The translational velocity of contrast agents as a function of radiation force pressure amplitude. (B) Images of standard deviation projections of microbubble lateral translation along the tube wall during radiation force pulsing at high (19 kPa) and low (8 kPa) pressures. As the pressure is increased, lateral motion along the wall caused by secondary radiation force can be clearly visualized as nonspherical trails. Note the displayed images are negatives of the actual projections; large values appear dark in these images.

and aggregation caused by secondary radiation force increased (Figure 6.6B). On the basis of qualitative observations from pixel-wise time-axis standard deviation projections (Figure 6.6B), it was hypothesized that the secondary radiation force at pressures  $>10$  kPa would not facilitate lasting ligand-integrin bond kinetics, because ARF pressures above this threshold caused bubbles to laterally translate along the cellulose tube wall. Thus,  $P_0$  was estimated to be 10 kPa because this setting would provide the best compromise between efficient bubble translation ( $50 \mu\text{m/s}$ ) and minimization of lateral movement after contact with the vessel wall.

### ***In vitro* studies: estimating optimal *in vivo* study parameters**

The CEF computations demonstrated that there was no single pressure appropriate for all tumor sizes. A 2D surface plot of the CEF values illustrates that for varying tumor sizes, there exist different acoustic pressures that will optimize radiation-force-enhanced targeting over the entire tumor depth (Figure 6.7A). The CEF predicted that the 13-kPa pressure setting would be the most effective *in vivo* protocol for a 1 cm tumor. A

4-kPa and a 21-kPa setting were also tested *in vivo* to compare the relative targeting efficiencies with the 13-kPa setting predicted by the CEF model.

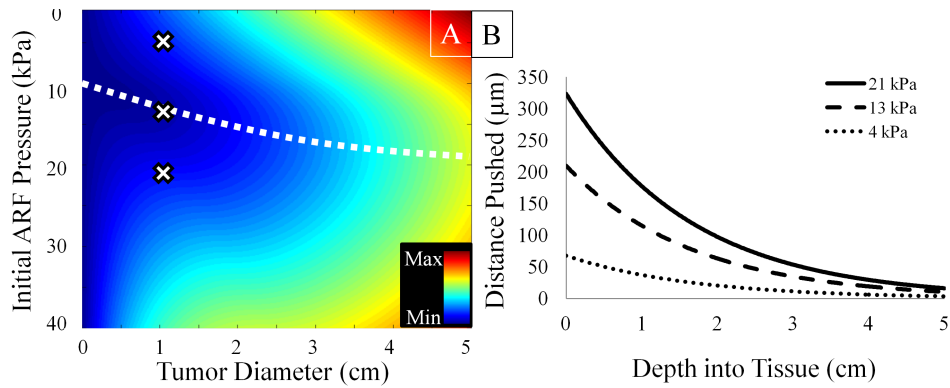


Figure 6.7: (A) The CEF plotted as a function of initial ARF push pressure and tumor diameter. Minimizing the CEF at a given tumor diameter provides the basis for estimating the optimal push protocol for an *in vivo* study (white dashed line). The Xs illustrate the three output settings that were tested and compared in the *in vivo* validation studies. (B) Simulations predicting the distance a microbubble would be pushed by ARF pulses for the three different initial pressure amplitudes as a function of depth into tissue.

The calculations of  $D_a$ , the expected distance microbubbles would translate *in vivo* along the ARF beam's propagation axis, revealed that both the initial push pressure and the depth into tissue determined whether a contrast agent would be sufficiently pushed out of circulation to the luminal wall (Figure 6.7B). In a previous histological analysis of vessels within xenografted tumors, 100  $\mu\text{m}$  was the upper bound on the range of vessel diameters [22]. It was predicted that the three pressure settings tested *in vivo* would provide sufficient microbubble translation ( $D_a \geq 50 \mu\text{m}$ ) at tissue depths <3.1 cm, 2.4 cm and 0.5 cm for the 21-kPa, 13-kPa and 4-kPa ARF amplitudes, respectively.

### ***In vivo* results**

Microbubbles targeted to angiogenic vasculature were used to compare ARF-enhanced targeting with conventional passive targeting (Figure 6.8). Of the tested ARF pulsing schemes, the maximum increase in microbubble targeting, as measured by mean

pixel intensities, was achieved using ARF pulses with a 13-kPa amplitude and a cRGD targeted bubble (nomenclature “RF-13/cRGD+”). In all of the animals tested, the volumetric targeted intensity was greater using RF-13/cRGD+ than with passive targeting (nomenclature “RF-0/cRGD+”). Notably, there was improved microbubble retention in 91% of all 2D image slices of RF-13/cRGD+ data collected when compared with the RF-0/cRGD+ studies (Table 6.1). In the remaining 9% of 2D image slices (in which the passive targeting images were brighter than the RF-13/cRGD+ images), there was a <1 dB difference between the mean pixel intensity of RF-13/cRGD+ data compared with the RF-0/cRGD+ case. Also of note, of the 9% of 2D image slices in which RF-13/cRGD+ was not as bright as the passive targeting run, 80% of these were within the same animal. This was likely an indication of a less angiogenic and more necrotic tumor in this one animal, and thus there was very little adhesion of targeted agents, either with or without ARF.

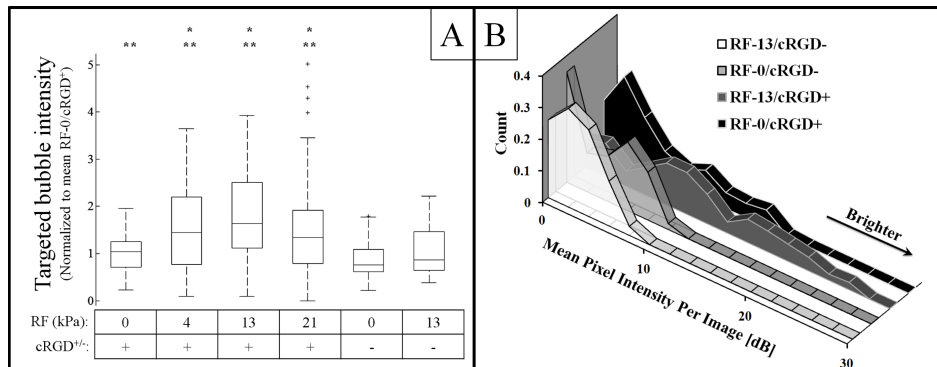


Figure 6.8: (A) A box-and-whiskers plot displaying the distribution of intensities within targeted bubble images. Data are normalized to 0 kPa/cRGD+ dataset. Asterisks indicate ( $p < 0.05$ ) over \* the RF-0/cRGD+ data, \*\* the RF-0/cRGD- data. (B) A comparison of the histograms of pixel intensities for cases listed. These histograms show a larger proportion of bright pixel values when targeted bubbles are used, and even more when radiation force is used with targeted bubbles.

The increase in mean pixel intensity across all animals was 77.8% higher with the RF-13/cRGD+ over the RF-0/cRGD+ case:  $11.4 \pm 7.0$  compared with  $6.4 \pm 4.8$ , respectively. The values represent baseline-subtracted pixel intensities, and thus the

	RF-4/cRGD <sup>+</sup>	RF-13/cRGD <sup>+</sup>	RF-21/cRGD <sup>+</sup>
% of Animals Exposed to ARF with Volumetric Targeting > Volumetric Passive Targeting	80%	100%	60%
% of Slices Exposed to ARF with Mean Targeting > Passive Targeting	65%	91%	51%

Table 6.1: A summary of the percentage of animals (top) and percentage of 2D image slices (bottom) that exhibited a greater degree of microbubble targeting in the ARF-enhanced targeting studies relative to the passive targeting studies.

units are measured in dB. The error in these values is the standard deviation of the baseline-subtracted pixel intensities. Similarly, both the RF-4 ( $8.8 \pm 7.9$ ) and RF-21 ( $8.8 \pm 7.0$ ) settings produced a statistically significant increase in targeting of cRGD+ bubbles relative to the RF-0/cRGD+ case. Of note, the RF-13/cRGD- case suggested a slight increase in mean pixel intensity for nonspecific microbubble adhesion relative to the RF-0/cRGD+ case; however, differences were not significant ( $p = 0.15$ ). The histograms created from the amalgamation of all un-normalized data show that, in general, the mean pixel intensity was higher for both ARF-enhanced and passive targeting studies (Figure 6.8B) compared with nontargeted controls. Furthermore, these histograms show that the RF-13/cRGD+ studies produced the greatest number of enhanced pixels. Figure 6.9 illustrates an example of ARF-enhanced targeted imaging and conventional passive targeting. In this image, the tumor volume is presented with a conically-stratified hinged cutaway, wherein elliptical regions of interest were drawn such that they did not follow the tumor border but instead cut into the interior of the tumor. This allows for microbubble targeting from within the tumor margins to be visualized on the rendered 3D surface, which we found to be useful in visualizing 3D molecular imaging data.

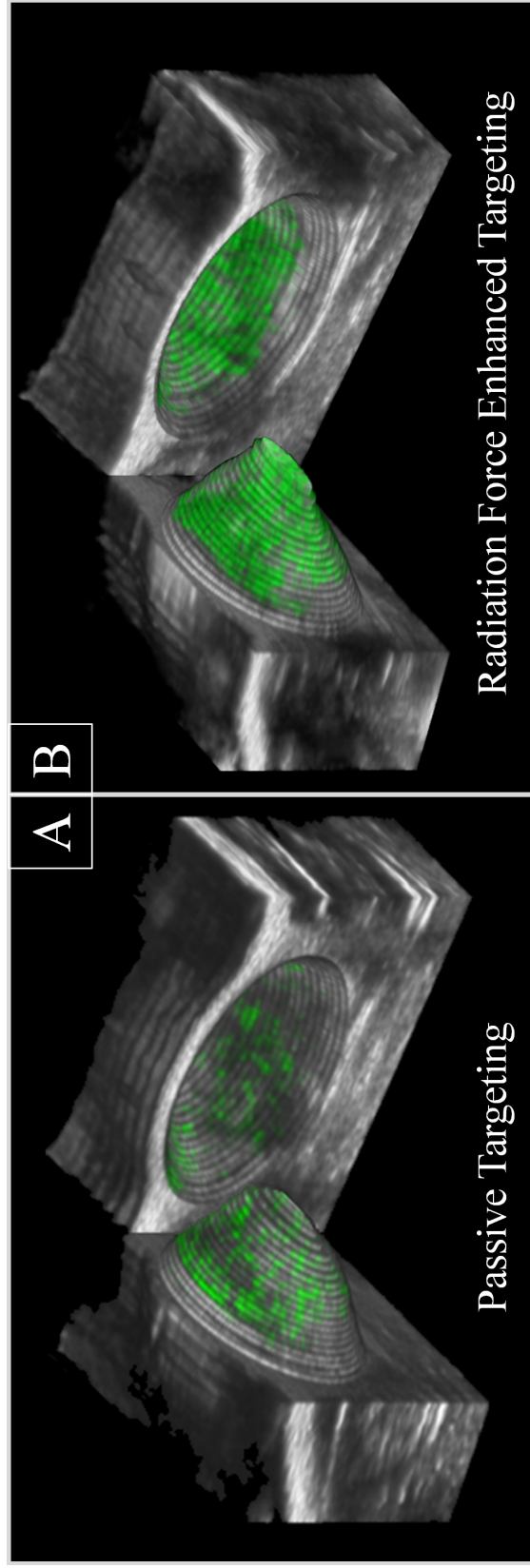


Figure 6.9: A side-by-side comparison of two 3D conically-stratified hinged cutaway images. B-mode images (grayscale) are registered to the corresponding CPS images acquired 10 min after contrast injection (green). In both of these images, the same dose of targeted microbubbles was administered to the same animal. Radiation force was not applied in (A) and was applied at 13 kPa in (B). The imaging field-of-view was 1.2x1.1x1.2 cm.

### 6.2.3 Discussion

#### Optimizing radiation force: *in vitro* predictions and *in vivo* results

Using ARF to facilitate molecular targeting of microbubbles to integrins expressed on diseased endothelium is an intuitive approach to improving the sensitivity of this diagnostic imaging methodology, but its application is nontrivial. Our *in vitro* studies allowed us to observe the behavior of microbubbles exposed to ARF pulses both during their translation and after making contact with the wall of a vessel-mimicking phantom. These analyses allowed us to tune parameters to predict the optimal settings for *in vivo* studies.

The calculation of the CEF demonstrated that because of the effects of tissue attenuation, there is no single setting for ARF amplitude that is universally appropriate to increase molecular imaging sensitivity at all tissue depths. Our CEF model predicted that ARF pulses with 13-kPa pressure amplitude to be the most effective of the three amplitudes studied. The model suggestions were supported by the *in vivo* study, because the 13-kPa pulses had the highest microbubble targeting efficiency. The CEF predictions for the two other pressure amplitudes tested (4 and 21 kPa) were very similar (Figure 6.7), which was also reflected in the *in vivo* data, because these pressures resulted in similar increases in microbubble targeting and were both less effective than the 13-kPa ARF pulses. This CEF model assumed a constant attenuation of  $0.6 \text{ Np cm}^{-1}$  throughout the depth of the tumor, which did not take into account the attenuation provided by the scatter of microbubbles in the tissue. Moreover, our method of tuning ARF pressure via the CEF assumes that a uniform density of integrin (or other biomarker) expression exists throughout the entire tumor volume. Although this is likely not true in the highly heterogeneous microenvironment of tumors, unless the heterogeneity is known a priori, the best strategy for improving molecular targeting is one that maximizes the probability of microbubble bond formation at all locations

within the tumor.

Our *in vivo* studies demonstrated an average increase in microbubble targeting of nearly 80% relative to traditional passive targeting studies, as measured by average pixel intensities within the baseline-subtracted images. It is important to emphasize that 91% of all the 2D image slices within the ARF-enhanced datasets exhibited greater microbubble targeting than the corresponding image frames taken from the passive targeting data. Of the remaining slices that exhibited greater microbubble adhesion in the passive targeting case, most were outliers found in a single animal that showed poor microbubble targeting in all experiments. This, along with the rest of the data summarized in Table 6.1, makes a compelling argument that ARF can improve the diagnostic use of ultrasonic molecular imaging studies.

When comparing the control microbubbles (nontargeted) with the cyclic RGD microbubbles (targeted) in the absence of ARF, it was apparent that nonspecific targeting was observed for the microbubble concentrations and tumor models used in this study. However, the application of ARF significantly increased the mean pixel intensity from the targeted agents, without significantly increasing the mean pixel intensity from the control agents - thereby providing a means to increase signal to noise in situations where there is a high nonspecific targeting background.

A persistent question surrounding the usefulness and applicability of ARF to *in vivo* molecular imaging studies is whether pushing populations of bubbles away from the proximal walls of vessels could actually be detrimental to maximizing the number of microbubble-integrin bonds. Although microbubble targeting on proximal vessel walls is likely negligible during the application of ARF pulses, after the pulses stop, these binding sites are free to be populated by the passive targeting of bubbles circulating through the vasculature. Regardless, based on our *in vitro* observations, the amount of increased bubble adhesion caused by ARF substantially outweighs any loss of targeting

on the proximal vessel walls. Another concern is whether acoustically forcing bubbles into vessel walls will cause an increase in nonspecific adhesion and thereby increase the rate of false-positive diagnoses. In this study, there was no significant difference in targeting efficiency between the control bubble with ARF application compared with the control bubble with no ARF (Figure 6.8). However, we suggest that this would need to be re-evaluated for different adhesion ligands and tumor types.

### **Comparison with previous work**

Previous *in vitro* work studying the increase in targeting efficiency of ARF-enhanced studies relative to passive targeted bubbles adhesion has demonstrated a large dependence on microbubble concentration. There was approximately 3 times more adhesion in passive targeting experiments without an appreciable difference in ARF efficiency when the bubble concentration was increased from  $2.5 \times 10^6$  to  $25 \times 10^6$  bubbles/mL [127]. This suggests that a larger difference in microbubble targeting effectiveness will be apparent if a lower concentration of microbubbles is used, though these studies have yet to be performed *in vivo*. In addition, because the magnitude of radiation force is highest at the resonant frequency of a microbubble [62], the frequency of our radiation force pulses could have been a source of reduction in expected targeting effectiveness. We were pulsing at 7 MHz, which was slightly higher than the resonance frequency of our bubbles ( $\sim 6$  MHz, as calculated using the method described in [139]). Finally, secondary radiation force is known to create aggregates of multiple microbubbles after contacting vessel walls [61; 127; 140] (Figure 6.6B). If these aggregates form lasting bonds with integrin targets, they will contribute to the image signal intensity differently than would a single bubble. This could have contributed to the variability observed in our *in vivo* studies.

In prior *in vivo* molecular imaging studies implementing ARF, Rychak et al. [70]



optically observed a >20-fold increase in microbubble adhesion *in vivo* using intravital microscopy in both the femoral artery and vein of a mouse model for inflammation, although this study relied on optically counting microbubbles through invasive intravital microscopy to quantify retention rather than using ultrasound imaging. Thus, a direct correlation between Rychak's data and the data presented herein is not possible. In Chapter 6.1 of this dissertation, we demonstrated the administration of ARF and acoustic detection of the targeted bubbles using a prototype high-resolution probe and custom pulse sequences, with an average microbubble targeting improvement of 13 dB across all image slices when ARF was used compared with passive targeting. There were many differences between that study and this one, including the ARF parameters and the imaging techniques' contrast sensitivities, which could account for the differences between the reported increase in sensitivity facilitated by radiation force in that paper (13 dB, or  $\sim 4.5$ -fold increase in detected contrast signal) relative to data presented here.

### **Limitations and future directions**

It was beyond the scope of the *in vitro* study of observations of contrast agents interacting with the tube wall to quantify the motion and trajectories of the bubbles after contacting the tube wall. This was because the aggregates of multiple contrast agents continually formed clusters of bubbles in an erratic fashion because of secondary radiation forces and thus made tracking individual contrast agents very difficult. The lack of this analysis notwithstanding, the standard deviation projections seen in Figure 6.6b demonstrate this effect and suggested that higher pressures would reduce the likelihood of lasting ligand-integrin bond formations. A more thorough analysis of this lateral motion would help define  $P_0$  more accurately than our coarse ability to adjust the amplitude of the ARF pulses permitted.

As mentioned previously, the best strategy for improving targeting is one that maximizes the probability of microbubble adhesion throughout the tumor. Because of attenuation effects, it was not possible in our *in vivo* studies to apply ARF uniformly at all axial depths. One potential strategy to apply a more homogeneous ARF profile to multiple depths within tissue (not examined in these studies) would be to sweep through multiple pressures at each spatial location. If at first a high pressure is used, it facilitates microbubble targeting deeper into tissue (as a result of attenuation) while simultaneously over-pushing at shallow depths. If the pressure is reduced steadily, microbubbles at shallower depths will be pushed at a more appropriate pressure without negatively affecting the targeted bubbles deeper in the tissue, because the pressure at these depths will have been reduced and thus the secondary radiation force effects minimized. Of note, over-pushing targeted contrast agents would likely be detrimental only to molecular imaging studies in which the lasting integrity of the microbubble's bond is critical. This limitation would probably not be a concern in ARF-mediated drug delivery, in which the ultimate goal is rapid and efficient localization and release of a microbubble's payload. In many ultrasound-mediated therapies, the microbubbles are disrupted immediately after pushing toward the endothelium, and long-term adhesion is not required [67; 68; 129]. Another method to provide a more uniform pushing region within the tissue could be to increase the F-number ( $z/D$ ) of the transducer, which would increase the depth of field of the transducer and thus offer a more uniform beam profile in depth. Normally this would carry with it a detrimental trade-off in spatial resolution, but would not negatively affect a radiation force enhanced molecular imaging study since no images are acquired during the push phase.

The time window over which radiation force is applied may also affect the increase in microbubble adhesion; if radiation force is administered continuously over several minutes as microbubbles circulate through the animal, more bubbles will be pushed

against the endothelium, although this increased microbubble traffic at the vessel wall could be counterproductive if it causes previously adherent agents to become dislodged.

The experiments performed in this chapter were done on a widely used clinical scanner without any additional customization of the software or pulse sequences, although we suggest that improved results would be obtained if dedicated optimized pulse sequencing and beam focusing/defocusing were available. Our approach did rely on mechanical scanning of the transducer to uniformly apply ARF pulses from the 1D linear array across the volume of tumor tissue, although this would be unnecessary if a 2D matrix array probe were available for high-resolution contrast imaging.

#### **6.2.4 Conclusion**

The studies presented herein provide validation of ARF applied with a clinical ultrasound system as a mechanism to enhance molecular imaging. In all *in vivo* studies, the average targeted microbubble signal throughout the 3D tumor volume was greater when using ARF (at 13 kPa) when compared with passive targeting studies. Our 3D imaging results demonstrate an improvement in signal intensity of 77.8% to our molecular target over conventional passive molecular imaging without an increase in nonspecific targeting. Furthermore, experiments suggest that for volumetric administration of radiation force, there exists an optimal pressure for ARF-enhanced targeting, which is a compromise between efficient bubble translation and adhesion-disruptive secondary radiation force and lateral translation effects.

## CHAPTER 7

### CLOSING REMARKS

Within this dissertation are the first studies implementing a transmit-low receive-high contrast ultrasound imaging approach enabled by a prototype dual-frequency transducer form factor. Our acoustic angiography imaging method produces high contrast and high resolution depictions of microvasculature. We have tested this transducer in an *in vitro* context by first examining resolution and contrast to tissue ratios (Chapter 3.1), and then using a novel microvessel phantom generation technique to generate ground-truth coordinates for vascular networks to be defined and imaged (Chapter 4). We then then extended our studies to both *in vivo* and *ex vivo* imaging applications. The *in vivo* studies were designed first to detect the presence of a tumor within a tissue volume (Chapter 5.1), and then later to assess the same tumor model's response to radiation therapy (Chapter 5.2). The acoustic angiography imaging approach was used in an *ex vivo* imaging context to assess the vasculature within a liver biomatrix scaffold model, a platform for creating of artificial organs (Chapter 3.2). A vessel mapping algorithm, originally developed for human magnetic resonance angiography images, was implemented in both of these *in vivo* and *ex vivo* contexts. Finally, the ultrasound pulsing technique, radiation force, was used as a method to improve the diagnostic sensitivity of ultrasound to malignant tumors (Chapter 6). Together, the results of these studies suggest that the acoustic angiography imaging approach, enabled by our new dual-frequency ultrasound transducer, could eventually be used to detect and monitor

tumors in a clinical imaging context.

## **7.1 The future acoustic angiography**

The scope of the acoustic angiography work to date is limited to the work presented in this dissertation. As such, the technology is in its infancy, but has shown initially promising results as a clinically translatable acquisition strategy for contrast imaging. Unfortunately, there are only two transducers in the world capable of acquiring acoustic angiography images, both of which are at UNC. Additionally, even if these probes were mass produced, there are several drawbacks which hinder their utility and thus will limit their widespread implementation as currently designed. First, their mechanically-scanned piston form factor is obsolete; manufacturers have stopped creating these designs and have instead switched to linear and matrix array transducers. Thus, the number of ultrasound systems capable of operating our transducers will steadily decline over the coming years. Second, implementing a transmit-low receive-high acoustic angiography approach on an array transducer is very important as a means to improve image quality. The axial beamfield maps of the transducers (Chapter 3.1) revealed a very shallow depth of field for these transducers ( $< 1$  cm). This problem manifested itself in a underestimation of the perfusion of larger tumors which were unresponsive to radiation therapy (Chapter 5.2). From a diagnostic standpoint, this systematic bias is unacceptable, though unavoidable in focused piston transducers. Though not yet available, an array transducers specifically designed to operate in acoustic angiography mode, would be capable of dynamic focusing, which would circumvent this issue. With collaborators, the Dayton lab at UNC is currently building two different form factors for transducers capable of operating in acoustic angiography mode (a catheter design for intravascular ultrasound, and a transrectal design for prostate assessment), so these avenues are being explored. Finally, image segmentation and classification techniques

to characterize vessel morphologies will require further development and training to achieve the level of automation, sensitivity and specificity required for a clinical tool.

Assuming the depth of field issues are resolved through better transducer designs, the future of acoustic angiography based vascular assessments appear bright. In the clinic, it could enable a bedside tool for rapid image acquisition, resulting in useful quantitative metrics to assist clinicians in fine-tuning patient-specific treatment plans. Owing to the high frequencies used to create high-resolution images with the acoustic angiography approach, only superficial cancers could be imaged, such as thyroid, melanoma, breast, and prostate lesions. Neovascularization within atherosclerotic plaques might also be an imaging application. Preclinical researchers are not faced with the same depth restrictions, as their mouse and rat models are comparatively small, and thus acoustic angiography-based microvascular mapping would enable candidate cancer therapeutics to be efficiently and noninvasively assessed in a wider array of tumor types.

Given the success of previous work related to quantifying vascular morphology for cancer assessment, the promising imaging quality achieved and the quantitative results demonstrated to date, we believe that acoustic angiography and microvascular mapping could have a large impact in preclinical and clinical cancer diagnostics.

## **7.2 The future molecular imaging with ultrasound**

Molecular imaging with ultrasound is an exciting field because it adds a new dimension of diagnostic capability to this already ubiquitous modality. It is certain that the future role of ultrasound in medicine will continue to increase due to its safety and convenience. Already some manufacturers are producing diagnostic systems no larger than a cellular phone that are intended to be as widely available as stethoscopes. With advancing understanding in molecular changes involved in disease progression, it is likely that

molecular imaging will enable detection of pathology and observation of response to treatment before phenotypic changes occur. Technology already exists to significantly increase the sensitivity of ultrasound to targeted contrast agents, such as presented in this dissertation with the addition of radiation force as the bolus of contrast agents circulates through volume of tissue suspected of containing a tumor. The addition of radiation force is not without limitations, however. While it has demonstrated the ability to increase the signal intensity from within tumors during molecular imaging studies, there is an additional variable in longitudinal studies of the consistency with which the radiation force is applied from timepoint to timepoint. In other words, to maximize the utility of this technique, it is paramount that identical pulsing sequences be applied in the same manner.

There are several other limitations of molecular imaging beyond simply field of view and contrast retention issues (addressed in Chapter 6). One active area of research is the effort to improve the monodispersity of the contrast agent populations injected. Resolving this issue will remove a substantial variable limiting the ability of ultrasound to perform quantifiable contrast measurements (i.e. to correlate image intensity to number of targeted contrast agents). Until that time, measurements can only be relative. Additionally, contrast agents have been engineered with modified lipid shell structures and ligand architectures to provide targeted contrast agents with better retention characteristics, and reduced immunogenicity. Transducers and signal processing are being developed to detect targeted contrast agents non-destructively, with high contrast-to-tissue ratios, and in real-time despite background signal from freely circulating contrast. Finally, the development of phase change and sub-micron contrast agents will enable ultrasound contrast to reach beyond the limits of the endothelium, especially important when trying to leverage the leakiness of tumor vessels for diagnostic purposes.

## APPENDIX A

### MICROBUBBLE CONTRAST AGENT FORMULATION

Three different microbubble formulations were used for these studies. Perfusion agents (used to depict blood flow), *in vitro* targeted agents (biotinylated microbubbles used to simulate a molecular imaging study via the biotin-avidin binding complex), and finally *in vivo* targeting agents (used to image regions of upregulated  $\alpha_v\beta_3$  expression). The details of their formulations are as follows.

#### A.1 Perfusion agents

These were created using a 9:1 molar ratio of DSPC and DSPE-PEG2000 (Avanti Polar Lipids, Alabaster, AL).

#### A.2 *In vitro* targeted agents

These were created using 9:0.5:0.5 molar ratio of DSPC, DSPE-PEG2000 and DSPE-PEG2000-Biotin (Avanti Polar Lipids, Alabaster, AL).

#### A.3 *In vivo* targeted agents

These were created with a 9:0.5:0.5 molar ratio of DSPC, DSPE-PEG2000 (Avanti Polar Lipids), and DSPE-PEG2000 cross-linked to a cyclic RGD peptide (Cyclo-Arg-Ala-Asp-D-Tyr-Cys) (Peptides International, Louisville, KY).



These lipid solutions were mixed into 1 mg/mL buffer solutions made of a 0.8:0.15:0.05 ratio of phosphate buffered saline, propylene glycol, and glycerol, respectively. Aliquots of 1.5 mL of were transferred to 3 mL vials, capped, and decafluorobutane was exchanged with the air in the vial headspace using a custom vacuum apparatus. The vials were then stored at 5°C until immediately prior to injection. Prior to injection, the vial was shaken vigorously for 45 seconds using a mixer (Vialmix, Bristol-Myers Squibb Medical Imaging, North Billerica, MA) to produce the microbubble contrast agents.

## APPENDIX B

### IEEE DECEMBER 2010 COVER IMAGE

#### **High-Resolution, High-Contrast Ultrasound Imaging Using a Prototype Dual-Frequency Transducer**

Caption: These images illustrate high-resolution contrast-enhanced imaging of the microvasculature, made possible with a prototype dual-frequency transducer designed to excite microbubbles near resonance and detect scattered echo content at frequencies greater than 15 MHz. On the left are 3-D images of a rat kidney, where the top is a maximum-intensity projection, and the bottom illustrates planar slices through the data. On the right are maximum intensity projections and planar slices from a subcutaneous fibrosarcoma tumor in a rat model. For further reading, see the accompanying article: R. Gessner, M. Lukacs, M. Lee, E. Cherin, F. S. Foster, and P. A. Dayton, "High-resolution, high-contrast ultrasound imaging using a prototype dual-frequency transducer: *In vitro* and *in vivo* studies," IEEE Trans. Ultrason. Ferroelectr. Freq. Control, vol. 57, no. 8, pp. 1772-1781, Aug. 2010. Images courtesy of Ryan Gessner, Marc Lukacs, Mike Lee, Emmanuel Cherin, F. Stuart Foster, and Paul A. Dayton. R. Gessner and P. A. Dayton are with the University of North Carolina and North Carolina State University Joint Department of Biomedical Engineering, Chapel Hill, NC. M. Lukacs, M. Lee, E. Cherin, and F. S. Foster are associated with the University of Toronto and the Sunnybrook Health Science Centre, Sunnybrook Imaging Research, Toronto, ON, Canada.

# IEEE TRANSACTIONS ON ULTRASONICS, FERROELECTRICS, AND FREQUENCY CONTROL

A PUBLICATION OF THE IEEE ULTRASONICS, FERROELECTRICS, AND FREQUENCY CONTROL SOCIETY



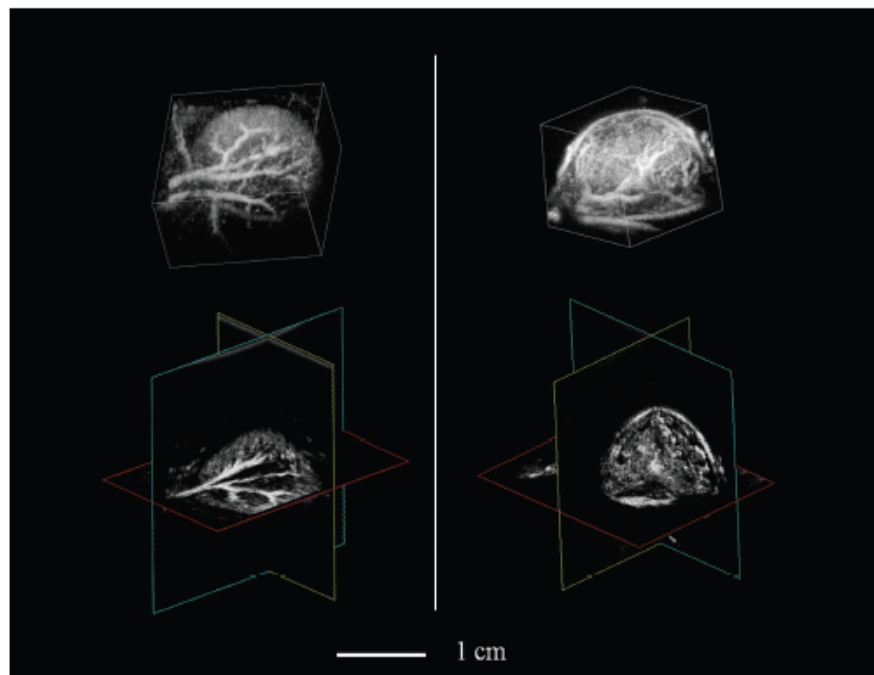
DECEMBER 2010


VOLUME 57

NUMBER 12

ITUCER

(ISSN 0885-3010)



Access the journal with its multimedia contents online  
at: <http://www.ieee-uffc.org/tr/> 

Digital Object Identifier 10.1109/TUFFC.2010.1729



## APPENDIX C

### ***EX VIVO* LIVER SCAFFOLD PREPARATION**

*Note: This appendix describes the experimental preparation required for the imaging studies performed in Section 3.2. This work was performed in collaboration with the Reid Lab. The graduate students who performed the decellularizations were Ariel Hanson and Brient Wu.*

#### **Decellularization of liver tissue**

Wistar rats (weights 250-300 g) were obtained from Charles River Laboratories, Wilmington, MA. They were housed in the animal facilities handled by the UNC Division of Laboratory Animal Management and were fed ad libitum until used for experiments. All experimental work for this study was approved by and performed in accordance with the UNC Institutional Animal Use and Care Committee guidelines.

All media were sterile-filtered (0.22- $\mu$ m filter) and kept in the dark at 4°C before use. To keep collagens stable in the biomatrix scaffolds, the pH of the perfusion media for biomatrix scaffold preparation was kept at 7.5-8.0. DME/F12 (Gibco/Invitrogen, Carlsbad, CA) and was used as the basal medium for preparation of biomatrix scaffolds. All reagents except those noted were obtained from Sigma (St. Louis, MO).

The protocol for decellularizing rat livers to produce biomatrix scaffolds has been

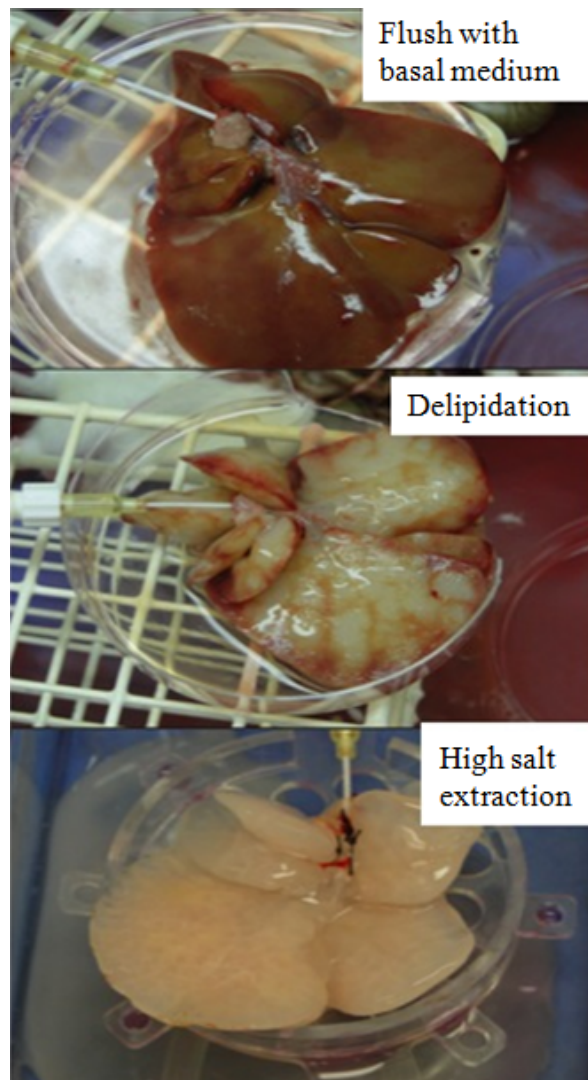


Figure C.1: Decellularization process: (Top) Flushing liver with a serum-free basal medium (e.g. DME/F12) to remove blood; (Middle) Delipidating with phospholipase A2 (PLA2) and then with PLA2 combined with deoxycholate; rinsing with serum-free DME/F12; Perfusing with 3.4 M high salt buffer (salt concentration dictated by collagen types in the tissue), with soybean trypsin inhibitor, and all kept at a pH of 7.5-8.0; rinsing to remove salt; (Bottom) Treating with nucleases to remove residual nucleic acids and then rinsing with serum-free basal medium and stored at 4 C.

described in prior publications 3. Briefly, male rats were anesthetized with Ketamine-Xylazine, and their abdominal cavity opened. The portal vein was cannulated with a 20-gauge catheter to provide a perfusion inlet to the vasculature of the liver, and the vena cava transected to provide an outlet for perfusion. The liver was then removed from the abdominal cavity and placed in a perfusion bioreactor. The blood was removed by flushing the liver with 300 mLs of DMEM/F12 (Gibco, Grand Island, NY). Delipidation (36 U/L of phospholipase A2 in 1% sodium deoxycholate; Fisher, Pittsburgh, PA) was used to remove plasma and nuclear membranes; this delipidation buffer was perfused through the liver for 1 hour or until the tissue became transparent. This was followed by perfusion for 90 minutes with a high salt buffer. Solubility constants for the known collagens in the liver are such that 3.4 M NaCl is adequate to keep all of the liver's collagens in an insoluble state. The liver was rinsed for 15 minutes with serum-free DMEM/F12 to eliminate the delipidation buffer and then followed by perfusion with 100 mLs of DNase (1 mg per 100 mL; Fisher, Pittsburgh, PA) and RNase (5 mg per 100 mL; Sigma Aldrich, St. Louis, MO) to remove any residual contaminants of nucleic acids from the scaffold. The final step was to rinse the scaffolds with DMEM/F12 for 1 hour to eliminate any residual salt.

The decellularized liver was stored overnight at 4 C (FigureC.2) and perfused with media at 3 mL min<sup>-1</sup> via a peristaltic pump (Masterflex, Cole-Parmer - Vernon Hills, IL) before the imaging study was performed. Prior to an imaging study, the biomatrix scaffold was transferred from the perfusion bioreactor into the sample imaging chamber. When in the sample imaging chamber, perfusion was maintained at 4 mL min<sup>-1</sup> through the portal vein via the same peristaltic pump.

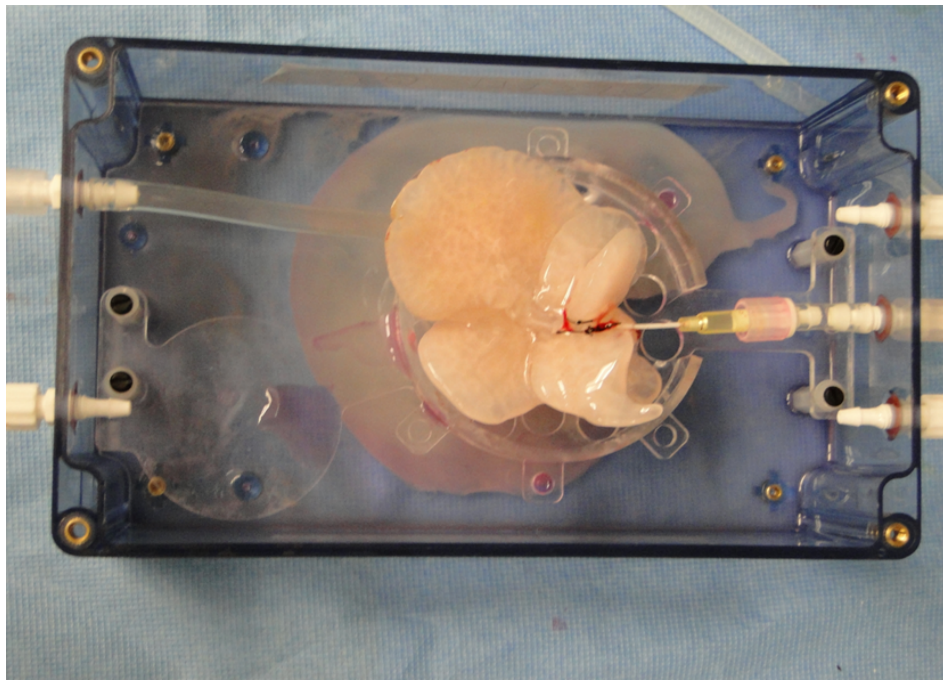


Figure C.2: Photograph of the decellularization bioreactor. The reagents flow through the inlet tubing (via a mechanical pump) and into the liver through the portal vein (right side). The liver is placed on a porous platform allowing waste to be collected in the bottom of the container and actively pumped out through an outlet on the left.

## BIBLIOGRAPHY

- [1] J. Folkman, "Role of angiogenesis in tumor growth and metastasis.," *Semin Oncol*, vol. 29, pp. 15–18, Dec 2002.
- [2] Frost and Sullivan, "U.s. preclinical animal imaging systems market - industry report," tech. rep., Frost & Sullivan Research Service, 2010.
- [3] D. H. Turnbull, J. A. Ramsay, G. S. Shivji, T. S. Bloomfield, L. From, D. N. Sauder, and F. S. Foster, "Ultrasound backscatter microscope analysis of mouse melanoma progression.," *Ultrasound Med Biol*, vol. 22, no. 7, pp. 845–853, 1996.
- [4] J. E. Chomas, R. E. Pollard, A. R. Sadlowski, S. M. Griffey, E. R. Wisner, and K. W. Ferrara, "Contrast-enhanced us of microcirculation of superficially implanted tumors in rats.," *Radiology*, vol. 229, pp. 439–446, Nov 2003.
- [5] N. Elie, A. Kaliski, P. Pronneau, P. Opolon, A. Roche, and N. Lassau, "Methodology for quantifying interactions between perfusion evaluated by dce-us and hypoxia throughout tumor growth.," *Ultrasound Med Biol*, vol. 33, pp. 549–560, Apr 2007.
- [6] F. S. Foster, P. N. Burns, D. H. Simpson, S. R. Wilson, D. A. Christopher, and D. E. Goertz, "Ultrasound for the visualization and quantification of tumor microcirculation.," *Cancer Metastasis Rev*, vol. 19, no. 1-2, pp. 131–138, 2000.
- [7] J. C. Sullivan, B. Wang, E. I. Boesen, G. D'Angelo, J. S. Pollock, and D. M. Pollock, "Novel use of ultrasound to examine regional blood flow in the mouse kidney.," *Am J Physiol Renal Physiol*, vol. 297, pp. F228–F235, Jul 2009.
- [8] P. Dayton and M. Borden, *Molecular Imaging in Oncology: Ultrasound Instrumentation and Techniques*. New York, NY: Informa, 2008.
- [9] J. R. Lindner, J. Song, A. R. Jayaweera, J. Sklenar, and S. Kaul, "Microvascular rheology of definity microbubbles after intra-arterial and intravenous administration.," *J Am Soc Echocardiogr*, vol. 15, pp. 396–403, May 2002.
- [10] F. S. Villanueva and S. Kaul, "Assessment of myocardial perfusion in coronary artery disease using myocardial contrast echocardiography.," *Coron Artery Dis*, vol. 6, pp. 18–28, Jan 1995.



- [11] K. Cheung, O. Couture, P. D. Bevan, E. Cherin, R. Williams, P. N. Burns, and F. S. Foster, "In vitro characterization of the subharmonic ultrasound signal from definity microbubbles at high frequencies.," *Phys Med Biol*, vol. 53, pp. 1209–1223, Mar 2008.
- [12] F. Forsberg, W. T. Shi, and B. B. Goldberg, "Subharmonic imaging of contrast agents," *Ultrasonics*, vol. 38, pp. 93–8, Mar 2000.
- [13] P. N. Burns, S. R. Wilson, and D. H. Simpson, "Pulse inversion imaging of liver blood flow: improved method for characterizing focal masses with microbubble contrast.," *Invest Radiol*, vol. 35, pp. 58–71, Jan 2000.
- [14] D. H. Simpson, C. T. Chin, and P. N. Burns, "Pulse inversion doppler: a new method for detecting nonlinear echoes from microbubble contrast agents.," *IEEE Trans Ultrason Ferroelectr Freq Control*, vol. 46, no. 2, pp. 372–382, 1999.
- [15] P. Phillips and E. Gardner, "Contrast-agent detection and quantification.," *Eur Radiol*, vol. 14 Suppl 8, pp. P4–10, Oct 2004.
- [16] S. M. Stieger, P. A. Dayton, M. A. Borden, C. F. Caskey, S. M. Griffey, E. R. Wisner, and K. W. Ferrara, "Imaging of angiogenesis using cadence contrast pulse sequencing and targeted contrast agents," *Contrast media & molecular imaging*, vol. 3, pp. 9–18, Jan 2008.
- [17] A. Saracco, P. Aspelin, K. Leifland, R. Themudo, B. Wilczek, and R. Axelsson, "Bolus compared with continuous infusion of microbubble contrast agent using real-time contrast harmonic imaging ultrasound in breast tumors.," *Acta Radiol*, vol. 50, pp. 854–859, Oct 2009.
- [18] J. Sijl, E. Gaud, P. J. A. Frinking, M. Arditì, N. de Jong, D. Lohse, and M. Versluis, "Acoustic characterization of single ultrasound contrast agent microbubbles.," *J Acoust Soc Am*, vol. 124, pp. 4091–4097, Dec 2008.
- [19] S. Z. Pinter and J. C. Lacefield, "Objective selection of high-frequency power doppler wall filter cutoff velocity for regions of interest containing multiple small vessels.," *IEEE Trans Med Imaging*, vol. 29, pp. 1124–1139, May 2010.
- [20] Y. Wang, H.-J. Dan, J.-H. Fan, and S.-B. Wen, "Evaluation of the correlation between colour power doppler flow imaging and vascular endothelial growth factor in breast cancer.," *J Int Med Res*, vol. 38, no. 3, pp. 1077–1083, 2010.
- [21] J. L. Alczar, M. Jurado, and G. Lpez-Garca, "Tumor vascularization in cervical cancer by 3-dimensional power doppler angiography: correlation with tumor characteristics.," *Int J Gynecol Cancer*, vol. 20, pp. 393–397, Apr 2010.

- [22] M. Palmowski, J. Huppert, P. Hauff, M. Reinhardt, K. Schreiner, M. A. Socher, P. Hallscheidt, G. W. Kauffmann, W. Semmler, and F. Kiessling, "Vessel fractions in tumor xenografts depicted by flow- or contrast-sensitive three-dimensional high-frequency doppler ultrasound respond differently to antiangiogenic treatment.," *Cancer Res*, vol. 68, pp. 7042–7049, Sep 2008.
- [23] M. E. Loveless, X. Li, J. Huamani, A. Lyshchik, B. Dawant, D. Hallahan, J. C. Gore, and T. E. Yankeelov, "A method for assessing the microvasculature in a murine tumor model using contrast-enhanced ultrasonography.," *J Ultrasound Med*, vol. 27, pp. 1699–1709, Dec 2008.
- [24] Y. Ding, E. A. Boguslawski, B. D. Berghuis, J. J. Young, Z. Zhang, K. Hardy, K. Furge, E. Kort, A. E. Frankel, R. V. Hay, J. H. Resau, and N. S. Duesbery, "Mitogen-activated protein kinase signaling promotes growth and vascularization of fibrosarcoma.," *Mol Cancer Ther*, vol. 7, pp. 648–658, Mar 2008.
- [25] K. Wei, A. R. Jayaweera, S. Firoozan, A. Linka, D. M. Skyba, and S. Kaul, "Quantification of myocardial blood flow with ultrasound-induced destruction of microbubbles administered as a constant venous infusion.," *Circulation*, vol. 97, pp. 473–483, Feb 1998.
- [26] R. E. Pollard, A. R. Sadlowski, S. H. Bloch, L. Murray, E. R. Wisner, S. Griffey, and K. W. Ferrara, "Contrast-assisted destruction-replenishment ultrasound for the assessment of tumor microvasculature in a rat model.," *Technol Cancer Res Treat*, vol. 1, pp. 459–470, Dec 2002.
- [27] R. Metoki, F. Moriyasu, N. Kamiyama, K. Sugimoto, H. Iijima, H.-X. Xu, T. Aoki, Y. Miyata, K. Yamamoto, K. Kudo, M. Shimizu, and M. Yamada, "Quantification of hepatic parenchymal blood flow by contrast ultrasonography with flash-replenishment imaging.," *Ultrasound Med Biol*, vol. 32, pp. 1459–1466, Oct 2006.
- [28] N. G. Chen, J. B. Fowlkes, P. L. Carson, and G. L. LeCarpentier, "Rapid 3d imaging of contrast flow: demonstration of a dual beam technique.," *Ultrasound Med Biol*, vol. 33, pp. 915–923, Jun 2007.
- [29] J. Shiraishi, K. Sugimoto, F. Moriyasu, N. Kamiyama, and K. Doi, "Computer-aided diagnosis for the classification of focal liver lesions by use of contrast-enhanced ultrasonography.," *Med Phys*, vol. 35, pp. 1734–1746, May 2008.
- [30] R. E. Pollard, P. A. Dayton, K. D. Watson, X. Hu, I. M. Guracar, and K. W. Ferrara, "Motion corrected cadence cps ultrasound for quantifying response to vasoactive drugs in a rat kidney model," *Urology*, vol. 74, pp. 675–81, Sep 2009.

- [31] S. Feingold, R. Gessner, I. M. Guracar, and P. A. Dayton, “Quantitative volumetric perfusion mapping of the microvasculature using contrast ultrasound,” *Invest Radiol*, vol. 45, pp. 669–74, Oct 2010.
- [32] K. Sugimoto, J. Shiraishi, F. Moriyasu, S. Ichimura, R. Metoki, and K. Doi, “Analysis of intrahepatic vascular morphological changes of chronic liver disease for assessment of liver fibrosis stages by micro-flow imaging with contrast-enhanced ultrasound: preliminary experience,” *Eur Radiol*, vol. 20, pp. 2749–2757, Nov 2010.
- [33] F. Molinari, A. Mantovani, M. Deandrea, P. Limone, R. Garberoglio, and J. S. Suri, “Characterization of single thyroid nodules by contrast-enhanced 3-d ultrasound,” *Ultrasound Med Biol*, vol. 36, pp. 1616–1625, Oct 2010.
- [34] S.-F. Huang, R.-F. Chang, W. K. Moon, Y.-H. Lee, D.-R. Chen, and J. S. Suri, “Analysis of tumor vascularity using three-dimensional power doppler ultrasound images,” *IEEE Trans Med Imaging*, vol. 27, pp. 320–330, Mar 2008.
- [35] C. Y. Li, S. Shan, Q. Huang, R. D. Braun, J. Lanzen, K. Hu, P. Lin, and M. W. Dewhirst, “Initial stages of tumor cell-induced angiogenesis: evaluation via skin window chambers in rodent models,” *J Natl Cancer Inst*, vol. 92, pp. 143–147, Jan 2000.
- [36] R. K. Jain, “Normalization of tumor vasculature: an emerging concept in antiangiogenic therapy,” *Science*, vol. 307, pp. 58–62, Jan 2005.
- [37] E. Bullitt, M. G. Ewend, S. Aylward, W. Lin, G. Gerig, S. Joshi, I. Jung, K. Muller, and J. K. Smith, “Abnormal vessel tortuosity as a marker of treatment response of malignant gliomas: preliminary report,” *Technol Cancer Res Treat*, vol. 3, pp. 577–584, Dec 2004.
- [38] E. Bullitt, N. U. Lin, J. K. Smith, D. Zeng, E. P. Winer, L. A. Carey, W. Lin, and M. G. Ewend, “Blood vessel morphologic changes depicted with mr angiography during treatment of brain metastases: a feasibility study,” *Radiology*, vol. 245, pp. 824–830, Dec 2007.
- [39] J. Folkman, “The role of angiogenesis in tumor growth,” *Semin Cancer Biol*, vol. 3, pp. 65–71, Apr 1992.
- [40] J. Folkman, “What is the evidence that tumors are angiogenesis dependent?,” *J Natl Cancer Inst*, vol. 82, pp. 4–6, Jan 1990.
- [41] J. Folkman, “Tumor angiogenesis,” *Adv Cancer Res*, vol. 43, pp. 175–203, 1985.
- [42] D. Fukumura, D. G. Duda, L. L. Munn, and R. K. Jain, “Tumor microvasculature and microenvironment: novel insights through intravital imaging in pre-clinical models,” *Microcirculation*, vol. 17, pp. 206–225, Apr 2010.

- [43] P. Carmeliet and R. K. Jain, "Principles and mechanisms of vessel normalization for cancer and other angiogenic diseases.," *Nat Rev Drug Discov*, vol. 10, pp. 417–427, Jun 2011.
- [44] A. H. Parikh, J. K. Smith, M. G. Ewend, and E. Bullitt, "Correlation of mr perfusion imaging and vessel tortuosity parameters in assessment of intracranial neoplasms.," *Technol Cancer Res Treat*, vol. 3, pp. 585–590, Dec 2004.
- [45] J. W. Baish and R. K. Jain, "Fractals and cancer.," *Cancer Res*, vol. 60, pp. 3683–3688, Jul 2000.
- [46] F. Yuan, Y. Chen, M. Dellian, N. Safabakhsh, N. Ferrara, and R. K. Jain, "Time-dependent vascular regression and permeability changes in established human tumor xenografts induced by an anti-vascular endothelial growth factor/vascular permeability factor antibody.," *Proc Natl Acad Sci U S A*, vol. 93, pp. 14765–14770, Dec 1996.
- [47] C. G. Willett, Y. Boucher, E. di Tomaso, D. G. Duda, L. L. Munn, R. T. Tong, D. C. Chung, D. V. Sahani, S. P. Kalva, S. V. Kozin, M. Mino, K. S. Cohen, D. T. Scadden, A. C. Hartford, A. J. Fischman, J. W. Clark, D. P. Ryan, A. X. Zhu, L. S. Blaszkowsky, H. X. Chen, P. C. Shellito, G. Y. Lauwers, and R. K. Jain, "Direct evidence that the vegf-specific antibody bevacizumab has antivascular effects in human rectal cancer.," *Nat Med*, vol. 10, pp. 145–147, Feb 2004.
- [48] E. Bullitt, M. Ewend, J. Vredenburg, A. Friedman, W. Lin, K. Wilber, D. Zeng, S. R. Aylward, and D. Reardon, "Computerized assessment of vessel morphological changes during treatment of glioblastoma multiforme: report of a case imaged serially by mra over four years.," *Neuroimage*, vol. 47 Suppl 2, pp. T143–T151, Aug 2009.
- [49] J. R. Eisenbrey, N. Joshi, J. K. Dave, and F. Forsberg, "Assessing algorithms for defining vascular architecture in subharmonic images of breast lesions.," *Phys Med Biol*, vol. 56, pp. 919–930, Feb 2011.
- [50] B. A. Kamen, J. Glod, and P. D. Cole, "Metronomic therapy from a pharmacologist's view.," *J Pediatr Hematol Oncol*, vol. 28, pp. 325–327, Jun 2006.
- [51] S. R. Aylward and E. Bullitt, "Initialization, noise, singularities, and scale in height ridge traversal for tubular object centerline extraction.," *IEEE Trans Med Imaging*, vol. 21, pp. 61–75, Feb 2002.
- [52] E. Bullitt, G. Gerig, S. M. Pizer, W. Lin, and S. R. Aylward, "Measuring tortuosity of the intracerebral vasculature from mra images.," *IEEE Trans Med Imaging*, vol. 22, pp. 1163–1171, Sep 2003.

- [53] D. Hanahan and R. A. Weinberg, “The hallmarks of cancer.,” *Cell*, vol. 100, pp. 57–70, Jan 2000.
- [54] J. E. Streeter, R. Gessner, I. Miles, and P. A. Dayton, “Improving sensitivity in ultrasound molecular imaging by tailoring contrast agent size distribution: in vivo studies,” *Mol Imaging*, vol. 9, pp. 87–95, Apr 2010.
- [55] R. Gessner and P. A. Dayton, “Advances in molecular imaging with ultrasound,” *Mol Imaging*, vol. 9, pp. 117–27, Jun 2010.
- [56] H. Leong-Poi, J. P. Christiansen, A. L. Klibanov, S. Kaul, and J. R. Lindner, “Noninvasive assessment of angiogenesis by ultrasound and microbubbles targeted to  $\alpha(v)$ -integrins,” *Circulation*, vol. 107, pp. 455–60, Jan 2003.
- [57] P. A. Schumann, J. P. Christiansen, R. M. Quigley, T. P. McCreery, R. H. Sweitzer, E. C. Unger, J. R. Lindner, and T. O. Matsunaga, “Targeted-microbubble binding selectively to  $\alpha_{IIb}\beta_3$  receptors of platelet thrombi,” *Invest Radiol*, vol. 37, pp. 587–93, Nov 2002.
- [58] B. A. Kaufmann, “Ultrasound molecular imaging of atherosclerosis,” *Cardiovascular Research*, vol. 83, pp. 617–25, Sep 2009.
- [59] J. R. Lindner, J. Song, J. Christiansen, A. L. Klibanov, F. Xu, and K. Ley, “Ultrasound assessment of inflammation and renal tissue injury with microbubbles targeted to p-selectin.,” *Circulation*, vol. 104, pp. 2107–2112, Oct 2001.
- [60] G. E. R. Weller, M. K. K. Wong, R. A. Modzelewski, E. Lu, A. L. Klibanov, W. R. Wagner, and F. S. Villanueva, “Ultrasonic imaging of tumor angiogenesis using contrast microbubbles targeted via the tumor-binding peptide arginine-arginine-leucine,” *Cancer Res*, vol. 65, pp. 533–9, Jan 2005.
- [61] P. Dayton, A. Klibanov, G. Brandenburger, and K. Ferrara, “Acoustic radiation force in vivo: a mechanism to assist targeting of microbubbles.,” *Ultrasound Med Biol*, vol. 25, pp. 1195–1201, Oct 1999.
- [62] P. A. Dayton, J. S. Allen, and K. W. Ferrara, “The magnitude of radiation force on ultrasound contrast agents.,” *J Acoust Soc Am*, vol. 112, pp. 2183–2192, Nov 2002.
- [63] H.-X. Xu, M.-D. Lu, X.-H. Xie, X.-Y. Xie, M. Kuang, Z.-F. Xu, G.-J. Liu, Z. Wang, L.-D. Chen, and M.-X. Lin, “Treatment response evaluation with three-dimensional contrast-enhanced ultrasound for liver cancer after local therapies.,” *Eur J Radiol*, vol. 76, pp. 81–88, Oct 2010.
- [64] F. Forsberg, N. M. Rawool, D. A. Merton, J. B. Liu, and B. B. Goldberg, “Contrast enhanced vascular three-dimensional ultrasound imaging.,” *Ultrasonics*, vol. 40, pp. 117–122, May 2002.

- [65] A. Bouakaz, S. Frigstad, F. J. T. Cate, and N. de Jong, "Improved contrast to tissue ratio at higher harmonics.," *Ultrasonics*, vol. 40, pp. 575–578, May 2002.
- [66] D. E. Kruse and K. W. Ferrara, "A new imaging strategy using wideband transient response of ultrasound contrast agents.," *IEEE Trans Ultrason Ferroelectr Freq Control*, vol. 52, pp. 1320–1329, Aug 2005.
- [67] M. J. Shortencarier, P. A. Dayton, S. H. Bloch, P. A. Schumann, T. O. Matsunaga, and K. W. Ferrara, "A method for radiation-force localized drug delivery using gas-filled lipospheres.," *IEEE Trans Ultrason Ferroelectr Freq Control*, vol. 51, pp. 822–831, Jul 2004.
- [68] A. F. H. Lum, M. A. Borden, P. A. Dayton, D. E. Kruse, S. I. Simon, and K. W. Ferrara, "Ultrasound radiation force enables targeted deposition of model drug carriers loaded on microbubbles," *Journal of Controlled Release*, vol. 111, pp. 128–34, Mar 2006.
- [69] S. Zhao, M. Borden, S. H. Bloch, D. Kruse, K. W. Ferrara, and P. A. Dayton, "Radiation-force assisted targeting facilitates ultrasonic molecular imaging.," *Mol Imaging*, vol. 3, pp. 135–148, Jul 2004.
- [70] J. J. Rychak, A. L. Klibanov, K. F. Ley, and J. A. Hossack, "Enhanced targeting of ultrasound contrast agents using acoustic radiation force," *Ultrasound in Medicine & Biology*, vol. 33, pp. 1132–9, Jul 2007.
- [71] T. C. Potdevin, J. B. Fowlkes, A. P. Moskalik, and P. L. Carson, "Analysis of refill curve shape in ultrasound contrast agent studies.," *Med Phys*, vol. 31, pp. 623–632, Mar 2004.
- [72] D. L. Miller and R. A. Gies, "Gas-body-based contrast agent enhances vascular bioeffects of 1.09 mhz ultrasound on mouse intestine.," *Ultrasound Med Biol*, vol. 24, pp. 1201–1208, Oct 1998.
- [73] S. Chen, M. H. Kroll, R. V. Shohet, P. Frenkel, S. A. Mayer, and P. A. Grayburn, "Bioeffects of myocardial contrast microbubble destruction by echocardiography.," *Echocardiography*, vol. 19, pp. 495–500, Aug 2002.
- [74] D. L. Miller, P. Li, D. Gordon, and W. F. Armstrong, "Histological characterization of microlesions induced by myocardial contrast echocardiography.," *Echocardiography*, vol. 22, pp. 25–34, Jan 2005.
- [75] D. L. Miller and C. Dou, "Contrast-aided diagnostic ultrasound does not enhance lung metastasis in a mouse melanoma tumor model.," *J Ultrasound Med*, vol. 24, pp. 349–354, Mar 2005.
- [76] P. A. van Der Wouw, A. C. Brauns, S. E. Bailey, J. E. Powers, and A. A. Wilde, "Premature ventricular contractions during triggered imaging with ultrasound contrast.," *J Am Soc Echocardiogr*, vol. 13, pp. 288–294, Apr 2000.

- [77] A. C. Borges, T. Walde, R. K. Reibis, A. Grohmann, R. Ziebig, W. Rutsch, I. Schimke, and G. Baumann, “Does contrast echocardiography with optison induce myocardial necrosis in humans?,” *J Am Soc Echocardiogr*, vol. 15, pp. 1080–1086, Oct 2002.
- [78] P. Li, L. qin Cao, C.-Y. Dou, W. F. Armstrong, and D. Miller, “Impact of myocardial contrast echocardiography on vascular permeability: an in vivo dose response study of delivery mode, pressure amplitude and contrast dose.,” *Ultrasound Med Biol*, vol. 29, pp. 1341–1349, Sep 2003.
- [79] D. Miller, P. Li, and W. F. Armstrong, “The effect of time and of vasoactive drugs on capillary leakage induced during myocardial contrast echocardiography.,” *Echocardiography*, vol. 21, pp. 125–132, Feb 2004.
- [80] P. Li, W. F. Armstrong, and D. L. Miller, “Impact of myocardial contrast echocardiography on vascular permeability: comparison of three different contrast agents.,” *Ultrasound Med Biol*, vol. 30, pp. 83–91, Jan 2004.
- [81] S. Chapman, J. Windle, F. Xie, A. McGrain, and T. R. Porter, “Incidence of cardiac arrhythmias with therapeutic versus diagnostic ultrasound and intravenous microbubbles.,” *J Ultrasound Med*, vol. 24, pp. 1099–1107, Aug 2005.
- [82] T. Ay, X. Havaux, G. V. Camp, B. Campanelli, G. Gisellu, A. Pasquet, J. F. Deneff, J. A. Melin, and J. L. Vanoverschelde, “Destruction of contrast microbubbles by ultrasound: effects on myocardial function, coronary perfusion pressure, and microvascular integrity.,” *Circulation*, vol. 104, pp. 461–466, Jul 2001.
- [83] N. Kobayashi, T. Yasu, S. Yamada, N. Kudo, M. Kuroki, K. Miyatake, M. Kawakami, and M. Saito, “Influence of contrast ultrasonography with perflutren lipid microspheres on microvessel injury.,” *Circ J*, vol. 67, pp. 630–636, Jul 2003.
- [84] N. Kobayashi, T. Yasu, S. Yamada, N. Kudo, M. Kuroki, M. Kawakami, K. Miyatake, and M. Saito, “Endothelial cell injury in venule and capillary induced by contrast ultrasonography.,” *Ultrasound Med Biol*, vol. 28, pp. 949–956, Jul 2002.
- [85] J. H. Wible, K. P. Galen, J. K. Wojdyla, M. S. Hughes, A. L. Klivanov, and G. H. Brandenburger, “Microbubbles induce renal hemorrhage when exposed to diagnostic ultrasound in anesthetized rats.,” *Ultrasound Med Biol*, vol. 28, no. 11-12, pp. 1535–1546, 2002.
- [86] F. Schlachetzki, T. Hlscher, H. J. Koch, B. Draganski, A. May, G. Schuierer, and U. Bogdahn, “Observation on the integrity of the blood-brain barrier after microbubble destruction by diagnostic transcranial color-coded sonography.,” *J Ultrasound Med*, vol. 21, pp. 419–429, Apr 2002.

- [87] D. L. Miller and R. A. Gies, "The influence of ultrasound frequency and gas-body composition on the contrast agent-mediated enhancement of vascular bioeffects in mouse intestine.," *Ultrasound Med Biol*, vol. 26, pp. 307–313, Feb 2000.
- [88] J. E. Chomas, P. Dayton, D. May, and K. Ferrara, "Threshold of fragmentation for ultrasonic contrast agents.," *J Biomed Opt*, vol. 6, pp. 141–150, Apr 2001.
- [89] J. M. Smith, S. W. Biggins, D. G. Haselby, W. R. Kim, J. Wedd, K. Lamb, B. Thompson, D. L. Segev, S. Gustafson, R. Kandaswamy, P. G. Stock, A. J. Matas, C. J. Samana, E. F. Sleeman, D. Stewart, A. Harper, E. Edwards, J. J. Snyder, B. L. Kasiske, and A. K. Israni, "Kidney, pancreas and liver allocation and distribution in the united states.," *Am J Transplant*, vol. 12, pp. 3191–3212, Dec 2012.
- [90] M. P. van de Kerkhove, R. Hoekstra, R. A. F. M. Chamuleau, and T. M. van Gulik, "Clinical application of bioartificial liver support systems.," *Ann Surg*, vol. 240, pp. 216–230, Aug 2004.
- [91] Y. Wang, H.-L. Yao, C.-B. Cui, E. Wauthier, C. Barbier, M. J. Costello, N. Moss, M. Yamauchi, M. Sricholpech, D. Gerber, E. G. Lobo, and L. M. Reid, "Paracrine signals from mesenchymal cell populations govern the expansion and differentiation of human hepatic stem cells to adult liver fates.," *Hepatology*, vol. 52, pp. 1443–1454, Oct 2010.
- [92] A. Berzat and A. Hall, "Cellular responses to extracellular guidance cues.," *EMBO J*, vol. 29, pp. 2734–2745, Aug 2010.
- [93] L. E. Smith, R. Smallwood, and S. Macneil, "A comparison of imaging methodologies for 3d tissue engineering.," *Microsc Res Tech*, vol. 73, pp. 1123–1133, Dec 2010.
- [94] H. Xu, S. F. Othman, and R. L. Magin, "Monitoring tissue engineering using magnetic resonance imaging.," *J Biosci Bioeng*, vol. 106, pp. 515–527, Dec 2008.
- [95] S. Young, J. D. Kretlow, C. Nguyen, A. G. Bashoura, L. S. Baggett, J. A. Jansen, M. Wong, and A. G. Mikos, "Microcomputed tomography characterization of neovascularization in bone tissue engineering applications.," *Tissue Eng Part B Rev*, vol. 14, pp. 295–306, Sep 2008.
- [96] X. Liang, B. W. Graf, and S. A. Boppart, "Imaging engineered tissues using structural and functional optical coherence tomography.," *J Biophotonics*, vol. 2, pp. 643–655, Nov 2009.
- [97] A. P. McGuigan and M. V. Sefton, "Vascularized organoid engineered by modular assembly enables blood perfusion.," *Proc Natl Acad Sci U S A*, vol. 103, pp. 11461–11466, Aug 2006.



- [98] M. L. Mather, S. P. Morgan, and J. A. Crowe, “Meeting the needs of monitoring in tissue engineering.,” *Regen Med*, vol. 2, pp. 145–160, Mar 2007.
- [99] F. S. Foster, M. Y. Zhang, Y. Q. Zhou, G. Liu, J. Mehi, E. Cherin, K. A. Harasiewicz, B. G. Starkoski, L. Zan, D. A. Knapik, and S. L. Adamson, “A new ultrasound instrument for in vivo microimaging of mice.,” *Ultrasound Med Biol*, vol. 28, pp. 1165–1172, Sep 2002.
- [100] R. H. Behler, T. C. Nichols, H. Zhu, E. P. Merricks, and C. M. Gallippi, “Arfi imaging for noninvasive material characterization of atherosclerosis. part ii: toward in vivo characterization.,” *Ultrasound Med Biol*, vol. 35, pp. 278–295, Feb 2009.
- [101] R. C. Gessner, S. R. Aylward, and P. A. Dayton, “Mapping microvasculature with acoustic angiography yields quantifiable differences between healthy and tumor-bearing tissue volumes in a rodent model.,” *Radiology*, vol. 264, pp. 733–740, Sep 2012.
- [102] R. Gessner, M. Lukacs, M. Lee, E. Cherin, F. S. Foster, and P. A. Dayton, “High-resolution, high-contrast ultrasound imaging using a prototype dual-frequency transducer: in vitro and in vivo studies.,” *IEEE Trans Ultrason Ferroelectr Freq Control*, vol. 57, pp. 1772–1781, Aug 2010.
- [103] M. Kaya, T. S. Gregory, and P. A. Dayton, “Changes in lipid-encapsulated microbubble population during continuous infusion and methods to maintain consistency,” *Ultrasound in Medicine & Biology*, vol. 35, pp. 1748–1755, Sep 2009.
- [104] P. N. Martins and P. Neuhaus, “Surgical anatomy of the liver, hepatic vasculature and bile ducts in the rat.,” *Liver Int*, vol. 27, pp. 384–392, Apr 2007.
- [105] Y. Wang, C.-B. Cui, M. Yamauchi, P. Miguez, M. Roach, R. Malavarca, M. J. Costello, V. Cardinale, E. Wauthier, C. Barbier, D. A. Gerber, D. Alvaro, and L. M. Reid, “Lineage restriction of human hepatic stem cells to mature fates is made efficient by tissue-specific biomatrix scaffolds.,” *Hepatology*, vol. 53, pp. 293–305, Jan 2011.
- [106] P. Kogan, K. A. Johnson, S. Feingold, N. Garrett, I. Guracar, W. J. Arendshorst, and P. A. Dayton, “Validation of dynamic contrast-enhanced ultrasound in rodent kidneys as an absolute quantitative method for measuring blood perfusion.,” *Ultrasound Med Biol*, vol. 37, pp. 900–908, Jun 2011.
- [107] E. Z. Zhang, J. G. Laufer, R. B. Pedley, and P. C. Beard, “In vivo high-resolution 3d photoacoustic imaging of superficial vascular anatomy.,” *Phys Med Biol*, vol. 54, pp. 1035–1046, Feb 2009.

- [108] J. Laufer, P. Johnson, E. Zhang, B. Treeby, B. Cox, B. Pedley, and P. Beard, “In vivo preclinical photoacoustic imaging of tumor vasculature development and therapy.,” *J Biomed Opt*, vol. 17, p. 056016, May 2012.
- [109] S. Aylward, E. Bullitt, S. Pizer, and D. Eberly, “Intensity ridge and widths for tubular object segmentation and description,” in *Proceedings of the Workshop on Mathematical Methods in Biomedical Image Analysis*, pp. 131–138, 1996.
- [110] E. Bullitt, D. Zeng, G. Gerig, S. Aylward, S. Joshi, J. K. Smith, W. Lin, and M. G. Ewend, “Vessel tortuosity and brain tumor malignancy: a blinded study.,” *Acad Radiol*, vol. 12, pp. 1232–1240, Oct 2005.
- [111] E. Bullitt, N. U. Lin, M. G. Ewend, D. Zeng, E. P. Winer, L. A. Carey, and J. K. Smith, “Tumor therapeutic response and vessel tortuosity: preliminary report in metastatic breast cancer.,” *Med Image Comput Comput Assist Interv*, vol. 9, no. Pt 2, pp. 561–568, 2006.
- [112] E. Bullitt, K. E. Muller, I. Jung, W. Lin, and S. Aylward, “Analyzing attributes of vessel populations.,” *Med Image Anal*, vol. 9, pp. 39–49, Feb 2005.
- [113] S. Hu and L. V. Wang, “Photoacoustic imaging and characterization of the microvasculature.,” *J Biomed Opt*, vol. 15, no. 1, p. 011101, 2010.
- [114] K. H. Song and L. V. Wang, “Deep reflection-mode photoacoustic imaging of biological tissue.,” *J Biomed Opt*, vol. 12, no. 6, p. 060503, 2007.
- [115] O. V. Solesvik, E. K. Rofstad, and T. Brustad, “Vascular structure of five human malignant melanomas grown in athymic nude mice.,” *Br J Cancer*, vol. 46, pp. 557–567, Oct 1982.
- [116] F. Denis, P. Bougnoux, L. de Poncheville, M. Prat, R. Catroux, and F. Tranquart, “In vivo quantitation of tumour vascularisation assessed by doppler sonography in rat mammary tumours.,” *Ultrasound Med Biol*, vol. 28, pp. 431–437, Apr 2002.
- [117] A. J. Schueneman, E. Himmelfarb, L. Geng, J. Tan, E. Donnelly, D. Mendel, G. McMahon, and D. E. Hallahan, “Su11248 maintenance therapy prevents tumor regrowth after fractionated irradiation of murine tumor models.,” *Cancer Res*, vol. 63, pp. 4009–4016, Jul 2003.
- [118] F. Denis, P. Bougnoux, L. Paon, O. le Floch, and F. Tranquart, “Radiosensitivity of rat mammary tumors correlates with early vessel changes assessed by power doppler sonography.,” *J Ultrasound Med*, vol. 22, pp. 921–929, Sep 2003.
- [119] F. Denis, S. Colas, L. Chami, P. Louisot, O. L. Floch, F. Tranquart, and P. Bougnoux, “Changes in tumor vascularization after irradiation, anthracyclin, or antiangiogenic treatment in nitrosomethyl ureas-induced rat mammary tumors.,” *Clin Cancer Res*, vol. 9, pp. 4546–4552, Oct 2003.

- [120] K. J. Niermann, A. C. Fleischer, E. F. Donnelly, A. J. Schueneman, L. Geng, and D. E. Hallahan, "Sonographic depiction of changes of tumor vascularity in response to various therapies.," *Ultrasound Q*, vol. 21, pp. 61–7; quiz 149, 153–4, Jun 2005.
- [121] D. W. N. Kim, J. Huamani, K. J. Niermann, H. Lee, L. Geng, L. L. Leavitt, R. A. Baheza, C. C. Jones, S. Tumkur, T. E. Yankeelov, A. C. Fleischer, and D. E. Hallahan, "Noninvasive assessment of tumor vasculature response to radiation-mediated, vasculature-targeted therapy using quantified power doppler sonography: implications for improvement of therapy schedules.," *J Ultrasound Med*, vol. 25, pp. 1507–1517, Dec 2006.
- [122] K. J. Niermann, A. C. Fleischer, J. Huamani, T. E. Yankeelov, D. W. Kim, W. D. Wilson, and D. E. Hallahan, "Measuring tumor perfusion in control and treated murine tumors: correlation of microbubble contrast-enhanced sonography to dynamic contrast-enhanced magnetic resonance imaging and fluorodeoxyglucose positron emission tomography," *J Ultrasound Med*, vol. 26, pp. 749–56, Jun 2007.
- [123] J. Huamani, C. Willey, D. Thotala, K. J. Niermann, M. Reyzer, L. Leavitt, C. Jones, A. Fleishcher, R. Caprioli, D. E. Hallahan, and D. W. N. Kim, "Differential efficacy of combined therapy with radiation and aee788 in high and low egfr-expressing androgen-independent prostate tumor models.," *Int J Radiat Oncol Biol Phys*, vol. 71, pp. 237–246, May 2008.
- [124] M. Hwang, G. Hariri, A. Lyshchik, D. E. Hallahan, and A. C. Fleischer, "Correlation of quantified contrast-enhanced sonography with in vivo tumor response.," *J Ultrasound Med*, vol. 29, pp. 597–607, Apr 2010.
- [125] M. F. Sullivan, S. Marks, P. L. Hackett, and R. C. Thompson, "X-irradiation of the exteriorized or in situ intestine of the rat.," *Radiat Res*, vol. 11, pp. 653–656, Nov 1959.
- [126] W. K. MacNaughton, "Review article: new insights into the pathogenesis of radiation-induced intestinal dysfunction.," *Aliment Pharmacol Ther*, vol. 14, pp. 523–528, May 2000.
- [127] J. J. Rychak, A. L. Klibanov, and J. A. Hossack, "Acoustic radiation force enhances targeted delivery of ultrasound contrast microbubbles: in vitro verification.," *IEEE Trans Ultrason Ferroelectr Freq Control*, vol. 52, pp. 421–433, Mar 2005.
- [128] M. A. Borden, M. R. Sarantos, S. M. Stieger, S. I. Simon, K. W. Ferrara, and P. A. Dayton, "Ultrasound radiation force modulates ligand availability on targeted contrast agents," *Mol Imaging*, vol. 5, pp. 139–47, Jul 2006.

- [129] A. Kheirrolomoom, P. A. Dayton, A. F. H. Lum, E. Little, E. E. Paoli, H. Zheng, and K. W. Ferrara, “Acoustically-active microbubbles conjugated to liposomes: characterization of a proposed drug delivery vehicle,” *J Control Release*, vol. 118, pp. 275–284, Apr 2007.
- [130] A. V. Patil, J. J. Rychak, J. S. Allen, A. L. Klibanov, and J. A. Hossack, “Dual frequency method for simultaneous translation and real-time imaging of ultrasound contrast agents within large blood vessels,” *Ultrasound in Medicine & Biology*, vol. 35, pp. 2021–30, Dec 2009.
- [131] S. Zhao, D. E. Kruse, K. W. Ferrara, and P. A. Dayton, “Selective imaging of adherent targeted ultrasound contrast agents,” *Phys Med Biol*, vol. 52, pp. 2055–2072, Apr 2007.
- [132] A. Needles, O. Couture, and F. S. Foster, “A method for differentiating targeted microbubbles in real time using subharmonic micro-ultrasound and interframe filtering,” *Ultrasound Med Biol*, vol. 35, pp. 1564–1573, Sep 2009.
- [133] A. Krol, M. W. Dewhirst, and F. Yuan, “Effects of cell damage and glycosaminoglycan degradation on available extravascular space of different dextrans in a rat fibrosarcoma,” *Int J Hyperthermia*, vol. 19, no. 2, pp. 154–164, 2003.
- [134] J. A. Feshitan, C. C. Chen, J. J. Kwan, and M. A. Borden, “Microbubble size isolation by differential centrifugation,” *Journal of Colloid and Interface Science*, vol. 329, pp. 316–324, Jan 2009.
- [135] J. E. Streeter, R. C. Gessner, J. Tsuruta, S. Feingold, and P. A. Dayton, “Assessment of molecular imaging of angiogenesis with three-dimensional ultrasonography,” *Mol Imaging*, Apr 2011.
- [136] D. A. Christensen, *Ultrasonic Bioinstrumentation*. John Wiley & Sons, 1988.
- [137] F. T. D’Astous and F. S. Foster, “Frequency dependence of ultrasound attenuation and backscatter in breast tissue,” *Ultrasound Med Biol*, vol. 12, pp. 795–808, Oct 1986.
- [138] C. Chang, S. Huang, H. Yang, Y. Chou, and P. Li., “Reconstruction of ultrasonic sound velocity and attenuation coefficient using linear arrays: clinical assessment,” *Ultrasound Med Biol*, vol. 33, no. 11, pp. 1681–7, 2007.
- [139] E. Quaia, *Contrast media in ultrasonography basic principles and clinical applications*. Springer, 2005.
- [140] S. Kotopoulis and M. Postema, “Microfoam formation in a capillary,” *Ultrasonics*, vol. 50, pp. 260–268, Feb 2010.